Delft University of Technology

Master's Thesis Report

Experimental Study on the Effects of Build Angle on Surface Roughness and Fluid Flow Performance in Laser-Powder Bed Fusion manufactured Micro-channels

Author:
Arthur Thiam (4472586)
February 18, 2024

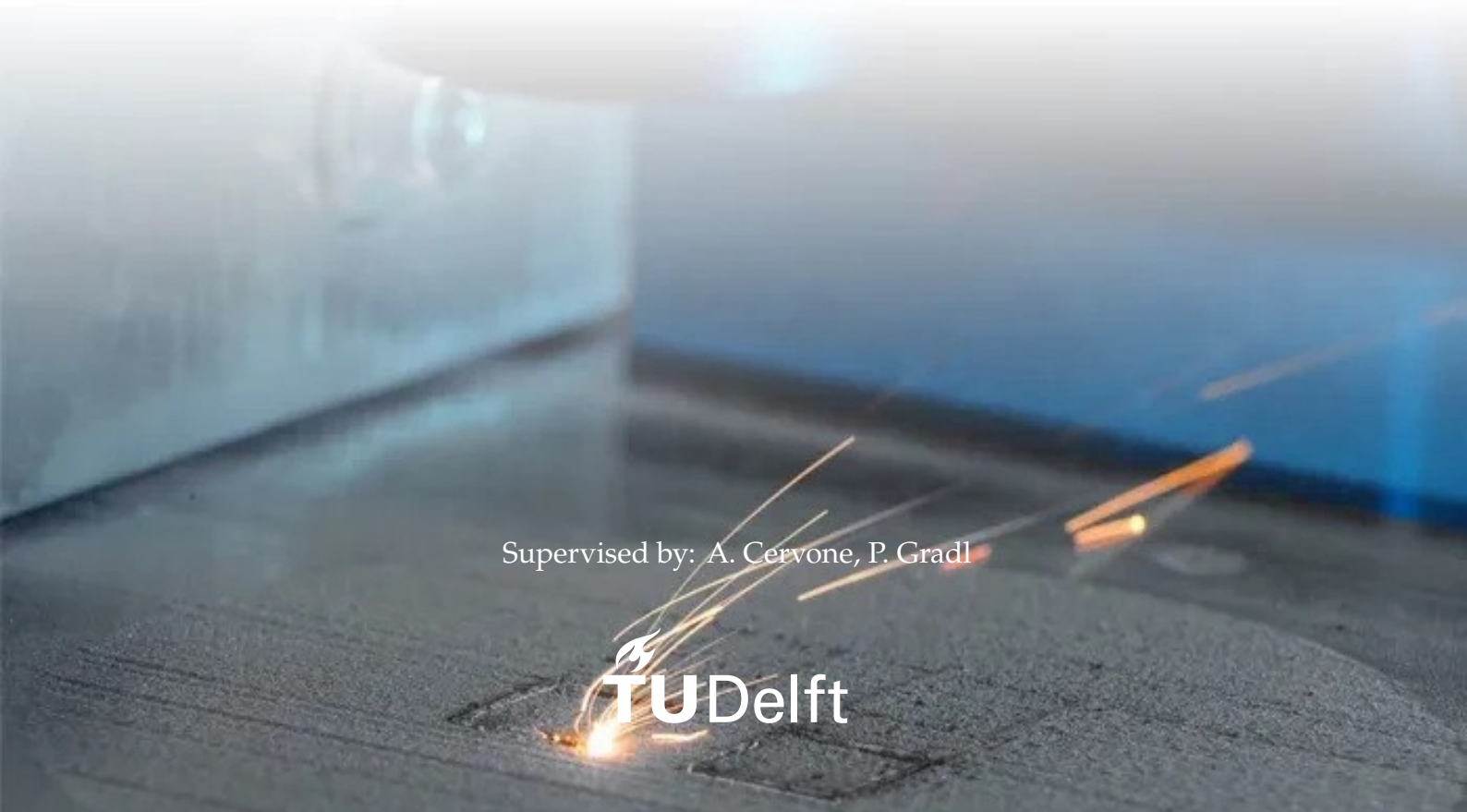

Supervised by: A. Cervone, P. Gradl

TU Delft

Experimental Study of L-PBF Micro-channel Surface Roughness

An Experimental Study on the Effects of Build Angle on Surface Roughness and Fluid Flow Performance in Laser-Powder Bed Fusion Manufactured Micro-channels

by

Arthur Thiam

To obtain the degree of Master of Science at the Delft University of Technology.
To be publicly defended on Wednesday 28^{th} of February 2024, at 15:30.

Publish date: 18^{th} of February, 2024

Student number:	4472586	
Faculty:	Aerospace Engineering, Delft	
Thesis committee:	Ir. B.T.C Zandbergen	Chair, TU Delft
	Dr. A. Cervone	Supervisor, TU Delft
	MSc. P. Gradl	Supervisor, NASA - MSFC
	Dr. Ir. E. Mooij	External reviewer, TU Delft

An electronic version of this thesis is available at `https://repository.tudelft.nl`

TU Delft

Preface

Dear reader,

This thesis report is written in the context of a masters degree in the field of Space Engineering at the Delft University of Technology. The master's thesis was supervised by Dr. Angelo Cervone, professor at the Space Systems Engineering department, and Msc. Paul Gradl, principal engineer at the NASA Marshall Space Flight Center.

I want to extend my warm thanks to Paul and Angelo for their support during this thesis. The experimental nature of this thesis in combination with full time propulsion engineering work was certainly challenging, and you guided me with clarity, understanding and patience throughout the research. I would also like to thank Koen Huybrechts and 3DSystems for kindly sponsoring the manufacturing of all test samples, and all of the staff at DEMO and HSL/LSL for their willingness to answer questions and help with the experimental setup.

My sincere gratitude goes out to Pangea Aerospace for supporting the research both financially and otherwise, and Federico Rossi, head of propulsion at Pangea, for giving me the flexibility I needed to complete this research.

Executive Summary

The work presented in this report was performed in the context of a masters thesis in the field of spaceflight engineering. Significant advances in the accuracy and versatility of manufacturing technologies such as Laser Powder bed Fusion have resulted in the increasing adoption of additive manufacturing [AM] for combustion chamber and nozzle design, enabling them to feature more complex, intricate and ultimately efficient solutions. One application of specific interest to this industry is the integrated manufacturing of cooling channels for combustion chambers of liquid rocket engines.

Despite all the advantages provided by AM, such as increased design freedom with reduced waste material and part count, the technology is characterized by a few key disadvantages. Of particular importance to the performance of rocket engine cooling channels is their surface roughness. Beyond the influence surface quality has on the efficiency of the heat transfer, the pressure drop caused by the channel dimensions and surface roughness has a great influence on the overall system efficiency. Large pressure drops place stringent requirements on upstream subsystems, requiring large output pressures for pumps, higher pressure valving and piping systems, and potentially higher storage pressures.

The consistency and predictability of these surface roughnesses in cooling channels, of which the build angle may vary along their tracks, is of paramount importance if combustion devices are to be manufactured using AM. To address this issue, the research presented in this thesis takes an experimental approach to studying both surface roughness and channel pressure drop for cooling channels representative of chamber/nozzle channels. The primary research question addressed was the following:

"How does the build angle of Laser powder bed fusion manufactured micro-channels relate to their internal surface roughness and fluid flow performance?"

To answer this question, 6 samples containing a total of 18 channels were printed. The printing was performed at 45°, 60° and 90° build angles, with the objective of investigating the relation between build angle, surface roughness, and friction factor. 6 channels were first selected for flow testing, filtering out those containing print defects that could influence test results. Pressure drops were then measured across a range of air flow rates using a differential pressure sensor for increased accuracy. The results were used to calculate friction factors, relative roughness and equivalent sand grain roughnesses for all channels.

Relative roughnesses were found to lie between 10% and 28%, confirming that small channels can fall outside of the applicability range of the Moody charts (originally created using tubing with up to 5% relative roughness). The equivalent sand grain roughness was shown to have a strong dependency on flow conditions. Additionally, trends of equivalent sand grain roughness with respect to Sa were investigated. Results show that while the general tendency indicates higher Sa values map to higher sand grain roughnesses, there is significant overlap in the data and it is difficult to separate the flow conditions from this relation.

After flow testing, upskin and downskin surfaces of all 18 channels were inspected using focus variation microscopy. The build angle was found to be inversely and linearly related with surface roughness, with 45° surfaces exhibiting the highest Sa values. Within individual

channels, downskin surfaces consistently had higher roughness than upskin surfaces. These findings are consistent with trends found in literature.

To deal with the impact of differing surface orientations (with respect to gas flow) and the unplanned use of two recoater blade types (due to batches being printed in different machines), the roughness analysis was extended to assess the influence of each. It was found that where orientation was the only differentiating factor (i.e. 90° surfaces within one batch), downskin oriented channels had a higher average roughness than the upskin orientation. This is likely related to the gas flow, and suggestions are included in recommendations for future work (see chapter 6). Review of the recoater blade influence revealed that the carbon blade recoater resulted in higher average roughness values than the soft blade recoaters, a trend that was found to be consistent with literature. The average deviation was shown to be at most 12%, and was deemed low enough to compare other trends across batches without further distinction.

Finally the samples were printed with two open channels each (up- and downskin). The goal was to investigate if open channels could be printed alongside closed channels to provide an accurate witness specimen for internal geometries. This would allow regenerative cooling channel roughnesses on combustion chambers to be validated without the need for destructive testing. In the case where channels are intended to be operated in as-built conditions, information from witness specimens may be useful in determining the required channel inlet pressures. On the other hand, if any form of surface polishing is planned, the as-built witness channel roughness may provide an indication of required exposure duration or other relevant post-processing parameters.

Sa values for the open channels were found to closely replicate those found on internal surfaces, meaning open channel witness specimens can be used to validate the roughness of internal channels. It should be noted that they were only compared to internal channels with matching orientation (with respect to gas flow), and future work on this is suggested in chapter 6. This may be specifically relevant in the context of complex channel flow paths that may not be easily replicable on witness specimens (e.g. helical/spiralling channel configurations).

Contents

List of Symbols **ix**

1 Introduction **1**

2 Literature Review **3**
2.1 Fundamentals of Additive Manufacturing . . . 3
2.1.1 L-PBF - The Basic Principle . . . 3
2.1.2 Advantages of AM . . . 6
2.1.3 Disadvantages of AM . . . 6
2.1.4 L-PBF for Chamber/Nozzle Micro-channels . . . 7
2.2 Micro-channel Performance . . . 8
2.3 Surface Roughness Metrics . . . 13
2.3.1 Profile Texture Parameters . . . 14
2.3.2 Sand Grain Roughness . . . 18
2.4 Surface Roughness Metrology . . . 19
2.5 Processing Parameters and Print Effects . . . 21
2.5.1 Common Print Defects . . . 21
2.5.2 Gas flow and Denudation . . . 25
2.5.3 Recoater blade . . . 26
2.5.4 Build angle . . . 28

3 Experimental Phase **30**
3.1 Test Objectives . . . 30
3.2 Test Matrix . . . 31
3.3 Test Plan . . . 32
3.3.1 Involved Parties . . . 32
3.4 Sample Design . . . 33
3.4.1 General Design Approach . . . 33
3.4.2 Sample Requirements . . . 34
3.4.3 Structural integrity . . . 35
3.4.4 Internal Roughness Witness Specimen . . . 36
3.4.5 Sample Design Overview . . . 36
3.5 Printing [P] . . . 37
3.5.1 Material Selection . . . 38
3.5.2 Machine Characteristics & Print Settings . . . 38
3.5.3 Print Defects & Sample Selection . . . 40
3.6 Post processing [M] . . . 42
3.6.1 Flow test preparation . . . 42
3.7 Flow Testing [T1] . . . 45
3.7.1 Measurement Strategy . . . 45
3.7.2 Fluidic Setup . . . 46
3.7.3 Leak Testing . . . 47
3.7.4 Data Acquisition . . . 48
3.8 Surface Roughness Measuring . . . 49
3.8.1 Microscope preparation [M4/M5] . . . 49
3.8.2 Microscope Measurements [T2/T3/T4] . . . 50

4 Results and Analysis **52**
4.1 Sample Selection . . . 52
4.2 Internal Surface Analysis . . . 52
4.2.1 Visual Surface Feature Analysis . . . 52
4.2.2 Sampling Area . . . 56
4.2.3 Form Correction and Data Filtering . . . 57
4.2.4 Areal Arithmetic Mean Height [Ra/Sa] . . . 58
4.2.5 Peaks and Valley Heights [Spk/Svk] . . . 62
4.2.6 Skewness [Ssk] . . . 63
4.2.7 Visual Cross Sectional Analysis . . . 64
4.2.8 Cross Sectional Area Measurements . . . 65
4.3 Flow Test Results . . . 68
4.3.1 Geometrical Parameters . . . 68
4.3.2 Flow Properties . . . 68
4.3.3 Pressure Drop and Friction Factor . . . 69
4.3.4 Relative and Sand grain Roughness . . . 71
4.3.5 Experimental Data Comparison . . . 74
4.4 Summary of Results . . . 75
4.4.1 Flow testing . . . 75
4.4.2 Surface Roughness Measurements . . . 75
4.4.3 Relative and Sand Grain Roughness . . . 76

5 Conclusions **77**

6 Recommendations **80**

A Overview of Surface Roughness Metrics **82**

B Sample Design Drawings **85**

C Welding Clamp Design Drawings **86**

D Sample Database **87**
D.1 Print Settings and Post Processing . . . 88
D.2 Defects and Sample Purposing . . . 89

List of Tables

2.1 Trademark L-PBF methods 5
2.2 Overview of common surface roughness measurement technologies 19

3.1 Test Matrix 32
3.2 Test Plan Elements 32
3.3 Sample design & process requirements 35
3.4 LaserForm material properties (for DMP Flex 350) 38
3.5 Print Specifications 39
3.6 Overview of post processing steps 42
3.7 Component control/readout details 48
3.8 Calibration Data 48

4.1 Cross sectional area measurements for flow tested samples 67

D.1 Sample print and process settings 88
D.2 Overview of sample print settings, defects, and testing 89

List of Figures

2.1 Laser Powder Bed Fusion Process [65] . . . 4
2.2 L-PBF Binding Mechanisms [42] . . . 5
2.3 2-piece dual cooled aerospike engine by Pangea Aerospace, L-PBF manufactured [GRCop42] [3] . . . 7
2.4 Moody Diagram [66] . . . 9
2.5 Stimpson et al. [62] experiment results . . . 11
2.6 Darcy friction factor representation based on constricted flow diameter [38] . . . 13
2.7 Overview of profile height parameters [75] . . . 16
2.8 Profile and Areal Surface Analysis [72] . . . 17
2.9 Comparative study of optical measurement techniques[67] . . . 20
2.10 Stairstep effect visualization [80] . . . 21
2.11 (a) Schematic of spatter formation; (b) High speed camera shot of typical spatter behaviour [48] . . . 23
2.12 continuous scan track (left), the shrinkage-induced balling (middle) and the spatter-induced balling (right) [35] . . . 23
2.13 Higher power, lower speed. Left: dross schematic, Right: SEM scan of 45° overhang dross.[70] . . . 24
2.14 Lower power, higher speed. Left: dross schematic, Right: SEM scan of 45° overhang dross.[70] . . . 25
2.15 Denuded zone with as function of gas (Ar) pressure (Torr) [49] . . . 26
2.16 Factor levels used in experimental design [60] . . . 27
2.17 Results of parametric analysis on the effect of recoater arm type, recoating speed and PSD [60] . . . 27
2.18 Surface roughness at varying recoater speeds and materials [44] . . . 28
2.19 Build angle schematic . . . 28

3.1 Layout of open and closed contour surfaces (cross section) . . . 37
3.2 Print Configuration . . . 40
3.3 Batch 1, 60° sample, kinked channels . . . 41
3.4 Batch 2, 45° & 60°, witness lines . . . 41
3.5 sample w/ holes, before welding . . . 43
3.6 Curvature on outer channel samples . . . 43
3.7 Sample interface welding . . . 44
3.8 Samples with compression fittings attached . . . 44
3.9 Sample ready for flow testing . . . 44
3.10 P&ID diagram of setup . . . 46
3.11 Test setup . . . 47
3.12 Sensor calibration curves . . . 49
3.13 Channel B1-45-B, processed for microscope analysis . . . 50
3.14 Example of stitched scan output after microscope inspection . . . 51

4.1 B1-90 downskin surface scans . . . 53
4.2 B1-90 upskin surface scans . . . 53
4.3 Optical scans of 90° closed contour surfaces . . . 54
4.4 B1-60 downskin surface scans . . . 54
4.5 B1-60 upskin surface scans . . . 55

4.6 B1-45 downskin surface scans . . . 55
4.7 B1-45 upskin surface scans . . . 56
4.8 Microscope scan areas for both batches . . . 57
4.9 Sa values for both printed batches . . . 58
4.10 Ra values for both printed batches . . . 59
4.11 Average Sa deviation . . . 60
4.12 Open contour surface roughness . . . 61
4.13 Spk values for both printed batches . . . 62
4.14 Ra values for both printed batches . . . 63
4.15 Skewness - Ssk . . . 64
4.16 Cross sectional scans of samples B1-45-A and B1-90-A . . . 64
4.17 Cross sectional area measurement, processed w/ ImageJ [4] . . . 65
4.18 Correction process for areal measurements, processed w/ ImageJ [4] . . . 66
4.19 Area/perimeter measurements . . . 67
4.20 Pressure drop by Reynolds number . . . 69
4.21 Derived friction factors . . . 70
4.22 Relative and Sand grain roughnesses . . . 71
4.23 Equivalent sand grain roughness ratios . . . 72
4.24 Friction factor by relative roughness . . . 73
4.25 Comparison of experimental results with findings from Stimpson [62] . . . 74

B.1 Sample Technical Drawing . . . 85

C.1 Welding Clamp Technical Drawing . . . 86

List of Symbols

Abbreviations

3ME	Faculty of Maritime, Mechanical and Materials Engineering
ACF	Auto-correlation function
AFM	Atomic force microscopy
AM	Additive Manufacturing
BSP	British Standard Pipe
BSP	British Standard Piping
CAD	Computer Aided Design
CC	Closed contour
CNC	Computer Numerical Control
CONF	Confocal microscopy
CSI	Coherence scanning interferometry
DASML	Delft Aerospace Structures and Materials Lab
DEMO	Dienst Elektro-Mechanische Ontwikkeling
DMLS	Direct Metal Laser Sintering
DMP	Direct Metal Printing
DZ	Denudation Zone
EDM	Electric Discharge Machining
FSLB	First line scan balling
FV	Focus Variation
HSL	High Speed Lab
HTFD	Hypersonic Test Facility Delft
ISO	International Organization for Standardization
L-PBF	Laser Powder Bed Fusion
LSL	Low Speed Lab
MEOP	Maximum Expected Operating Pressure
NI	National Instruments
NLPM	Normal liters per minute
NPT	National Pipe Thread
OC	Open contour
P&ID	Piping and Instrumentation Diagram
PSD	Particle Size Distribution
RMS	Root mean square
ROI	Region of interest
SEM	Scanning electron microscope
SF	Safety factor
SLM	Selective laser melting
SLP	Structured light profilometry
SLS	Selective Laser Sintering
WLI	White light interferometry

Variables

ϵ	Absolute roughness
μ	Viscosity
σ_y	Yield stress
θ	Build angle
A	Area
D_h	Hydraulic diameter
d_{eq}	Equivalent diameter
$D_{h,c}$	Constricted flow hydraulic diameter
$f_{D,cf}$	Constricted flow friction factor
g	Gravitational acceleration
h_f	Frictional head loss
L	Tube length
l_r	Sampling length
L_t	Layer thickness

p	pressure
Ra	Profile arithmetic mean height
Re	Reynolds number
Re_{cf}	Constricted flow Reynolds number
rho	Density
Rku	Profile kurtosis
Rq	Root-mean-square profile height
Rsk	Profile skewness
Rz	Max profile height over assessment length
Sa	Areal arithmetic mean height
Sdc	Arithmetic mean peak curvature
Sku	Areal kurtosis
Smc	Inverse areal material ratio
Smr	Areal material ratio
Sp	Areal max peak height
Spk	Reduced peak height
Sq	Areal root-mean-squares height
Ssk	Areal skewness
Sv	Areal max valley depth
Svk	Reduced valley height
Sz	Areal max surface height
T	Temperature
V	Velocity
Vm	Material volume
Vmc	Core material volume
Vv	Void volume
Vvc	Core void volume
$z(x)$	Height profile
f	Friction factor

Chapter 1

Introduction

In recent decades, the surge in the demand for space access has fueled a need for scalable solutions while concurrently driving down the costs associated with development and operational aspects [8]. Simultaneously, significant advancements have been made in the realm of manufacturing technologies, with metal additive manufacturing (AM) emerging as a potentially transformative innovation [11]. This technology provides design engineers with increased design flexibility, streamlined assembly processes, cost-efficient production, and minimal material wastage [11]. These advantages make AM of particular interest for the space industry, where design solutions are often limited by manufacturing capabilities.

The fabrication of combustion chambers and nozzles with integrated cooling channels using Laser Powder bed Fusion (L-PBF) is one such example [31]. L-PBF is a subset of AM technologies that relies on the layer-wise addition and selective melting of a metal powder, yielding high dimensional accuracies when compared to other metal AM solutions, like Directed Energy Deposition [DED] [39]. Cooling channel geometry and integration to the hot wall has a direct impact on their efficiency, and by extension, the performance of the entire propulsion system. Beyond the increase in efficiency of existing designs, AM has the potential to unlock certain system designs previously considered unfeasible due to limitations in manufacturing techniques.

Despite the numerous advantages, L-PBF manufacturing grapples with a few inherent challenges. Of particular importance to small fluid flow channels are the surface quality and dimensional accuracy, which are both considerably lower than most traditional manufacturing options (such as subtractive machining or molding) [29]. The relation between the processing parameters used to print and the resulting surface quality are complex and not always predictable.

Among the more impactful processing parameters is the build angle. The build angle represents the angle between a printed surface and the horizontal base plate of the printer from which the part is built. A horizontal surface will have a build angle of 0°, while a vertical surface will have a build angle of 90°. In the case of nozzle or combustion chamber printing, this build angle will vary along the length of a singular channel, and can cause it to have a wide range of roughness levels. In addition, channel performance is usually evaluated using empirical relations such as Moody charts, but these are based on parameters that have no applicability to relative roughness levels of small channels [62], and no clear relation to modern day surface texture parameters obtained from optical measurements.

Finally, inspection of surface quality for small closed channels typically involves destructive testing, a process that is not feasible on combustion chambers intended for flight. To tackle these issues, the research presented in this thesis addresses the following research question:

"How does the build angle of Laser powder bed fusion manufactured micro-channels relate to their internal surface roughness and fluid flow performance?"

This research question is further divided into the following four sub-questions:

- **SQ-1:** What is the influence of varied build angle on the surface roughness of L-PBF flow channels?
- **SQ-2:** What is the influence of varied printing build angle on the friction factor of L-PBF flow channels?
- **SQ-3:** How representative are open-contour witness samples of closed-contour prints?
- **SQ-4:** How do the performed measurements and tests relate to the primary research question?

An experimental approach was chosen in order to provide meaningful data and investigate the relations between various parameters and performance effects. To do this, a number of small channels (both open and closed) of square cross section were additively manufactured using Laser powder bed fusion. Closed contour channels were first flow tested, after which they were cut open and inspected along with their open channel counterparts. This report presents the methodology and results of said experiments, provides insight on the relations found, and lays out future recommended work with regards to the remaining uncertainties. Each of the sub-questions listed above is linked to a set of specific objectives that can be found in section 3.1.

First, a review of relevant literature concerning additive manufacturing, surface roughness and channel performance is provided in chapter 2. This chapter elaborates on the general characteristics of L-PBF printing in the context of this research, as well as on the performance assessment and prediction of fluid flow channels using Moody diagrams. Additionally, a discussion on the equipment and metrics used for quantifying surface roughness is included. The experimental phase in chapter 3 then describes the overall approach to the test campaign. The chapter details the approach to sample design and test campaign planning, and provides a detailed overview on the experimental setup, as well as all manufacturing, machining and testing steps. All test results are then reported and discussed in chapter 4. This includes an analysis of surface quality and roughness metrics, an assessment of the cross sectional areas and their impact on test results, and a calculation of friction factors and relative roughness levels based on flow test results. In chapter 5, conclusions on the test results and analysis are provided and related back to all research (sub-)questions. Finally, a number of recommendations for future work are given in chapter 6.

Chapter 2

Literature Review

In this chapter, literature relevant to the topic of surface roughness in microchannels is discussed. While the topic of additive manufacturing of micro-channels can easily extend past the topics discussed here, a selection of topics and concepts primarily relevant to the experiments and results analysis were selected.

2.1 Fundamentals of Additive Manufacturing

The term "Additive manufacturing (AM)" covers the entirety of manufacturing technologies that rely on the layerwise *addition* of material (as opposed to the subtraction thereof). At the core, AM allows models that are generated using Computer Aided Design (CAD) to be manufactured with a significantly reduced process planning [30]. Though there is a large variety of AM processes, each with specific advantages and disadvantages, they all rely on the same process: parts are built by adding varying cross-sections in a layer-by-layer fashion [30].

In its early phases, most applications of AM concerned the use of polymer printing for prototyping purposes. Further advances in AM technology (including the ability to print metal parts) enabled the field to grow and find applications in rapid prototyping, tooling, part production and the repair of parts [15]. Laser Powder Bed Fusion (L-PBF), one of the more widely used AM technologies, is of particular interest for combustion chamber/nozzle channel manufacturing for a variety of reasons. Its main characteristics and how they relate to the application of L-PBF for chamber/nozzle channels are discussed in the following sections.

2.1.1 L-PBF - The Basic Principle

As mentioned in section 2.1, AM is based on the layer-wise addition of a material whereby each layer constitutes a specific cross-section of the to-be-built part. This approach comes with a very specific set of challenges when compared to traditional manufacturing technologies. How and to what extent these challenges are resolved is what typically differentiates one AM technology from another. Generally speaking, an AM technology is characterized by three main components: A thermal source (Used for changing the material state), a mechanism to control material fusion to a predefined region in the layer (i.e. forming of the part cross section), and a mechanism for adding new layers [30]. In the case of metal AM, the thermal source is used to fully or partially melt a metal powder, which is solidified into the part upon cooling. The selective melting of metal powder in a specific region of a powder layer is possible with an electron beam, but is more frequently done with a laser. Lasers are able to achieve higher dimensional accuracies and better surface finishes [15], both of which can have significant impact on the performance of the final part. Alternatively an electron beam can be used as a thermal source (EB-PBF). This requires a vacuum to be created during processing, allowing higher operating temperatures and reduced thermal distortion, but it is incompatible with ferrous metals due to the electron beams [46].

The laser used in metal AM machines is focused on a thin layer of metal powder (typically in the order of 20-100 μm [15]). This causes the powder to either melt (in the case of full powder

melting) or fuse (in the case of sintering applications), thereby creating a solidified cross section of the part. If oxygen is present in the printing chamber and the metal is susceptible to oxidation, an oxide layer may form between powder layers, causing a deterioration in bond strength [59]. To prevent this, the entire process is performed in a controlled environment filled with inert gas [26]. If metals with higher thermal conductivity are being printed, the melting process can be improved by increasing the temperature of the bed (base-plate upon which the layers are stacked) closer to the powder melt point [19][35]. An example of this is the metal printing of copper alloys, where pre-heating of the bed has been shown to improve inter-particle bonding, due to a higher thermal gradient being present across the powder/metal layers [35].

Once a cross section of the part is melted and re-solidified, the bed is moved downwards to allow the placement of a new layer of powder (see Figure 2.1). The process can then be repeated until the entire part has been built, at which point excess powder is removed and the part is detached from the base-plate. Generally speaking, L-PBF is considered to be feasible with any metal that can be welded. Many metal AM alloys are commercially available in powder form, while others are proprietary alloys specifically developed for printing.

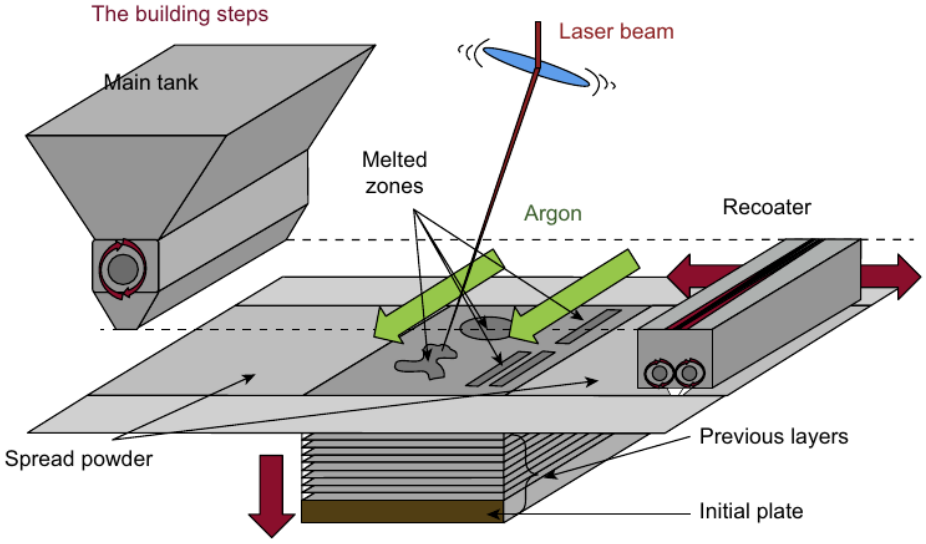

Figure 2.1: Laser Powder Bed Fusion Process [65]

Within the subset of laser-based L-PBF printing, we find a large amount of processes. Each presents a different approach to the implementation of laser-based L-PBF printing, and as a result of intellectual property rights and the competitive nature of the manufacturing market, each approach also has a different name/acronym. This can often lead to confusion, so it is useful to define and distinguish them for further clarity. The range of L-PBF implementations includes SLS, SLM, DMLS, DMP and LaserCusing to name a few of the more common ones. They are essentially various trademarked implementations of L-PBF printing technology, though they are often used to refer to other companies/printers using the same process:

Table 2.1: Trademark L-PBF methods

Acronym	Name	Trademark
SLS	Selective Laser Sintering	3DSystems
SLM	Selective Laser Melting	SLM Solutions
DMLS	Direct Metal Laser Sintering	EOS
DMP	Direct Metal Printing	3DSystems
LaserCusing	Laser Cusing	Concept Laser

While most of the differences between these methods are relatively small, it is worth noting the definitions of sintering and melting. These refer to the binding mechanism used for turning the powder into a solid part. Kruth et al. [42] classifies the various binding mechanisms of L-PBF printing as follows:

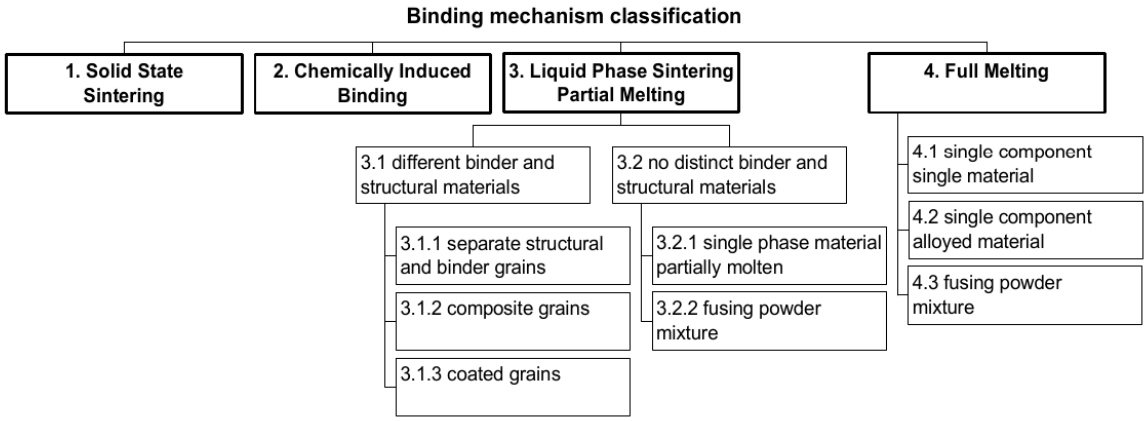

Figure 2.2: L-PBF Binding Mechanisms [42]

Sintering

Sintering refers to the partial melting of the powder layer. Sintering techniques can be combined with feedstock powders that are composed of different materials and/or particle sizes. A distinction may for example be made between the binder and structural material, where the binder is molten and the structural material remains solid throughout the process. It can also utilize bi-modal powders, composed of different particle sizes, or multi-phase powders, composed of multiple materials. However, partial melting can also be achieved in a single-phase material by carefully controlling the degree of powder consolidation through process parameters such as laser power and speed [54].

Full Melting

The full melting process, as the name suggests, melts the full layer in a single step to achieve closer to 100% density [54]. This process can be achieved with both single or alloyed powder materials. While the higher density can provide certain desireable material properties, the higher temperature gradients required to fully melt a powder layer can result in delamination or part distortion [41] [42], as well as the occurence of balling, a common L-PBF surface defect further addressed in section 2.5. The various implementations shown in Table 2.1 are all slightly differently calibrated approaches to these two methods.

2.1.2 Advantages of AM

When comparing to traditional manufacturing techniques (subtractive, cold forming, welding, casting), many of the (dis-)advantages that characterize L-PBF printing are common to all AM technologies. The nuances of the various AM technologies then present a more detailed set of (dis-)advantages that highlight what AM approach is more suitable for certain applications. In this section and subsection 2.1.3, (dis-)advantages are discussed on a more broad level, comparing AM to traditional manufacturing techniques.

At its core, layer-wise addition of material means a high percentage of the processed material is used in the final part. This is also referred to as the build-to-fly ratio, and unless post processing is applied such as polishing/post-machining/chemical milling, it can reduce these ratios from 10:1-20:1 down to 1:1 [15]. In addition to the highly efficient use of processed material, L-PBF printing offers the possibility for recycling the unused powder within the machine up to 12-14 times without significant changes in the material properties [12]. This further results in a lower need for raw material production, as well as less usage of toxic chemicals such as lubricant or coolant [18].

From a design perspective, the additive nature of AM also provides a significant increase in design freedom. Design for subtractive manufacturing is heavily influenced by manufacturability, tool accessibility and assembly process. Assemblies need to be manufactured out of multiple parts, and the entire process requires careful planning and selection of machines and eventual joining processes such as welding/bolting/riveting/etc. Instead, additive manufacturing allows these multi-stage processes to be executed in a single print. In a demonstration of the process feasibility to the application of channel wall nozzles, Gradl and Protz [33] explain that metal AM has the potential to save cost and reduce fabrication time while allowing to more easily scale production.

Beyond the efficiency and ecological footprint, the design freedom provided by AM processes allows for more complex geometries or internal features to be manufactured, essentially increasing the solution spaces designers can work with. The improvements further extend downstream of the manufacturing process too. The mentioned removal of assembly/joining processes removes the need for bolts/joints, leading to overall reductions in mass. This effect can snowball into the overall optimization of the system for which the part is destined. This is of particular interest to areas where weight optimization is of great importance, such as the aeronautical and space industries. Furthermore, generative shape design processes can explore a greater design space, as parts are geometrically constrained essentially by only two things: total available build volume, and accessibility for removal of required support structures and unmelted powder.

2.1.3 Disadvantages of AM

Despite the numerous advantages mentioned above, there are a few characteristics specific to AM that require particular attention.

The manufacturing process can be very slow. AM technology can typically add material at a much slower rate than subtractive method can remove it (L-PBF typically reaches build rates of 35cm3 /hr [36]). This is balanced by the fact that assemblies that would normally require multiple parts, can be built out of single elements using AM. The same applies for cost: AM is typically an expensive manufacturing technique, and its cost efficiency tends to cross over that

of traditional techniques when production is scaled up [69].

Of particular relevance to the manufacturing of small cooling channels, L-PBF printing offers lower dimensional accuracy and higher surface roughness than its subtractive counterparts. This can have a negative effect on fatigue resistance and tolerancing, as well as pressure drop and heat transfer coefficients. The mean surface height deviation (Ra) of L-PBF parts can typically reach down to 4µm - 11µm [74], though this depends on many factors and can be much higher in certain cases. This stands in stark contrast to the sub-µm levels achievable with CNC machining [77].

2.1.4 L-PBF for Chamber/Nozzle Micro-channels

One direct application of additive manufacturing is the printing of combustion chambers, nozzles and injector heads for liquid propulsion. These are typically very complex components with multiple flow paths, that have to operate under extreme pressures and temperature gradients. While these are traditionally manufactured from a number of machined parts, there are already numerous examples of AM being applied in an effort to further simplify and optimize the manufacturing process, while simultaneously enabling design improvements that were impossible or hard to achieve previously. A good example of this is the aerospike engine shown in Figure 2.3, which was fully manufactured from GRCop42, a copper alloy developed specifically for printing by Gradl et al. [32]. AM enabled this engine to be built out of only two pieces, integrating two separate cooling channel circuits for liquid oxygen and liquid methane into the walls of the printed elements.

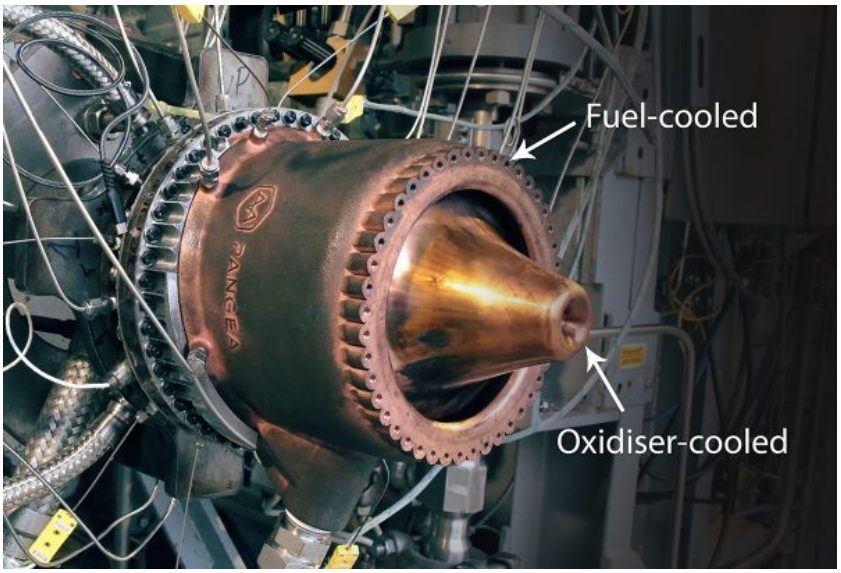

Figure 2.3: 2-piece dual cooled aerospike engine by Pangea Aerospace, L-PBF manufactured [GRCop42] [3]

However, the printing of combustion chambers for regeneratively cooled engine cycles implies that the small cooling channels used for heat exchange are subject to the disadvantages of L-PBF printing mentioned in subsection 2.1.3. While the higher surface roughness of L-PBF compared to for example CNC machining is not necessarily problematic on large fluid flow channels, the problem is accentuated on smaller scales. On mm, or even sub-mm scales, L-PBF surface roughness can become significant in comparison to the hydraulic diameter of a fluid flow channel. This so-called *relative roughness* turns out to be a key performance parameter

when it comes to channel pressure drop, heat exchange efficiency, and thus overall system performance. section 2.2 elaborates on the various aspects of pressure drop through small AM channels.

2.2 Micro-channel Performance

The performance of small fluid flow channels can be assessed in various ways, and generally depends on the topic of research and the application of the channels. Within the space of rocket engine cooling channels, fluid flow channels can serve several purposes. Primarily, the cooling channels use the propellant to cool the walls of the combustion chamber and/or nozzle before their injection into the chamber. The transfer of heat from the walls into the propellant before combustion has the additional benefit of heating the propellant, at times gasifying it, which increases combustion efficiency by reducing the required energy within the chamber to ignite propellant molecules. Finally, in expander cycles, the propellant can purposely be vaporized in the cooling channels in order to drive turbines and forgo the need for gas generators or pre-burners.

The cooling channels have an effect on engine design in two fundamental ways. Firstly, their design affects how the fluid properties evolve throughout the channel, and how much heat can be extracted from the chamber/nozzle wall. Secondly, much as a consequence of the evolution of fluid properties throughout the channel and the chamber inlet requirements, their design places a requirement on the channel inlet conditions of the propellant flow. The contribution of internal surface roughness of a channel to the fluid pressure drop becomes of significant importance when they are additively manufactured (for reasons mentioned in subsection 2.1.3). More concretely, a high surface roughness may lead to more effective heat transfer, but also to a significant increase in pressure drop and therefore required inlet pressure. On high thrust engines, this may place difficult to reach requirements on the head rise provided by the turbomachinery. On smaller pressure-fed/blow-down systems (think of in-space propulsion) it can result in excessive or infeasible tank masses due to high storage pressures.

As can be seen, the properties of engine cooling channels can have far-reaching impact on the design and performance of a propulsion system. The implementation of AM for the design and manufacturing of rocket engines allows for the direct integration of channels into the walls of chambers and nozzles [32]. This avoids the need for intricate manufacturing and assembly processes such as the milling of channels and attachment of a outer close-out liner, or even the brazing of cooling channels onto the outer wall of a nozzle [32]. That being said, the ability to predict channel performance in both pressure drop and heat transfer is paramount to their integration through AM. The scope of the experiments and analysis presented in this thesis is directed at gaining a better understanding of how the pressure drop in small AM channels relates to quantifiable parameters used to characterize surface roughness.

Head loss and Friction factor

The pressure loss through a tube/pipe is usually related to the surface roughness using the head loss and friction factor. The head loss is a measure for the energy loss in a flow trough a tube/pipe, and can be attributed to a set of major and minor losses. Minor losses are caused by irregularities and accessories present in the tube, but can be neglected as the focus of this study is on one of the major losses: the frictional effects stemming from surface roughness [79].

The frictional head loss, denoted by h_f, is used to represent the drop in fluid head due to friction. The Darcy-Weisbach equation (Equation 2.1 as published by Bhave [16]) is able to relate this frictional head loss to the flow properties, pipe/tube dimensions, and the Darcy friction coefficient. The equation can be re-arranged to relate actual pressure drop to fluid properties and a characteristic dimension of the tube (Equation 2.2):

$$h_f = \frac{fL}{D}\frac{V^2}{2g} \tag{2.1}$$

$$\Delta p = \frac{f \cdot L}{D_h} \cdot \frac{1}{2}\rho V^2 \tag{2.2}$$

Here, the hydraulic diameter D_h is a relation between cross sectional area and perimeter. ρ and V are the fluid density and velocity respectively, L the tube length, and f the friction factor. This last parameter is where the effects of surface roughness are accounted for in the Darcy-Weisbach relation. There is no way to directly determine the friction factor of a surface, primarily because it is not purely a surface property. It is also dependent on the properties of the fluid flowing through the channel. Historically, it has been determined based on empirical relations, most commonly those established by Moody in 1944 [47]. The Moody Diagrams show how the friction factor of a channel varies with flow reynolds number for a variety of relative roughnesses (see Figure 2.4)

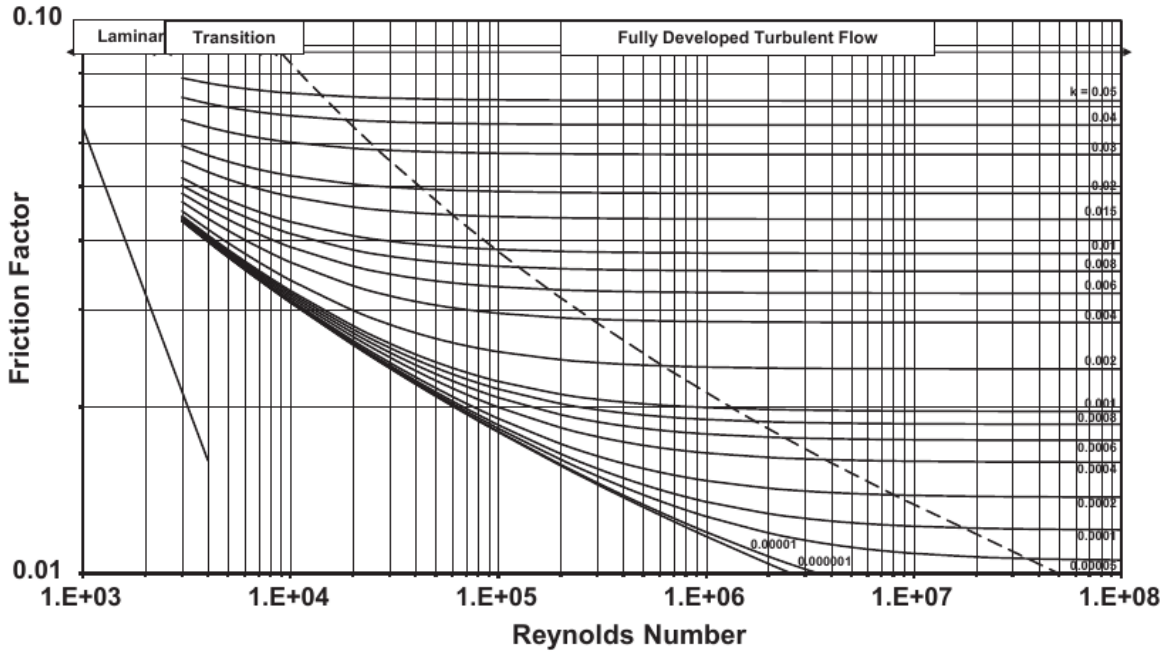

Figure 2.4: Moody Diagram [66]

The relative roughness ϵ/D (denoted k in Figure 2.4) is a measure for the absolute roughness in relation to the diameter of the tube. This absolute roughness is also referred to as the equivalent sand grain roughness [13]. In the case of non-round tubes, the hydraulic diameter can be used. As the diagram shows, the higher the relative roughness is, the higher a tube friction factor will be for any given Reynolds number. This then translates to a head loss in the flow through the channel. In a given tube, the flow friction factor varies with Reynolds number according to three different relations depending on the flow state. For example for fully laminar flow,

the friction factor is not dependent on relative roughness and can be determined with $f = \frac{64}{Re}$. For fully developed turbulent flow, the Moody chart can be determined using the colebrook formula [56] (originially published by Colebrook [22]):

$$\frac{1}{\sqrt{f}} = -2.0 \log \left(\frac{\epsilon/D}{3.7} + \frac{2.51}{\mathrm{Re}\sqrt{f}} \right) \tag{2.3}$$

As can be seen, the friction factor is not a material characteristic. It stems from a combination between material characteristics and flow properties. The derivation of friction factor then comes from empirical observations.

High Relative Roughness

The theory presented above is well suited for relatively smooth piping. The relations given by the Moody charts are based on empirical observations that considered only tubing with relative roughnesses up to 5% according to Stimpson [62]. Low relative roughnesses occur when the surface is very smooth, or when the pipe hydraulic diameter is very large. In the case of AM microchannels, we find the opposite scenario for both: small cross sectional areas with high roughness levels. As a result, the relative roughness of AM microchannels tends to be higher than traditionally manufactured channels (e.g. milled channels), which can cause the Moody charts to become less reliable.

Huang et al. [37] performed an experimental study on the effects of large relative roughnesses on the friction factor of channels. Tubes with relative roughnesses up to 42% were tested, and it was shown that even in the laminar flow regime, relative roughnesses of 7% and higher already resulted in higher friction factors than predicted by the $64/Re$ relation from the Moody chart. Dai et al [23] further confirmed this trend by showing that even at relative roughnesses above 2%, friction factor coefficients were higher than predicted by Moody.

A study on the effects of ϵ/D and friction coefficients on the heat transfer in small channels, performed by Stimpson et al. [62], compares the performance of various channel sizes (all manufactured using AM). An overview of the resulting friction factors at various flow conditions can be found in Figure 2.5 :

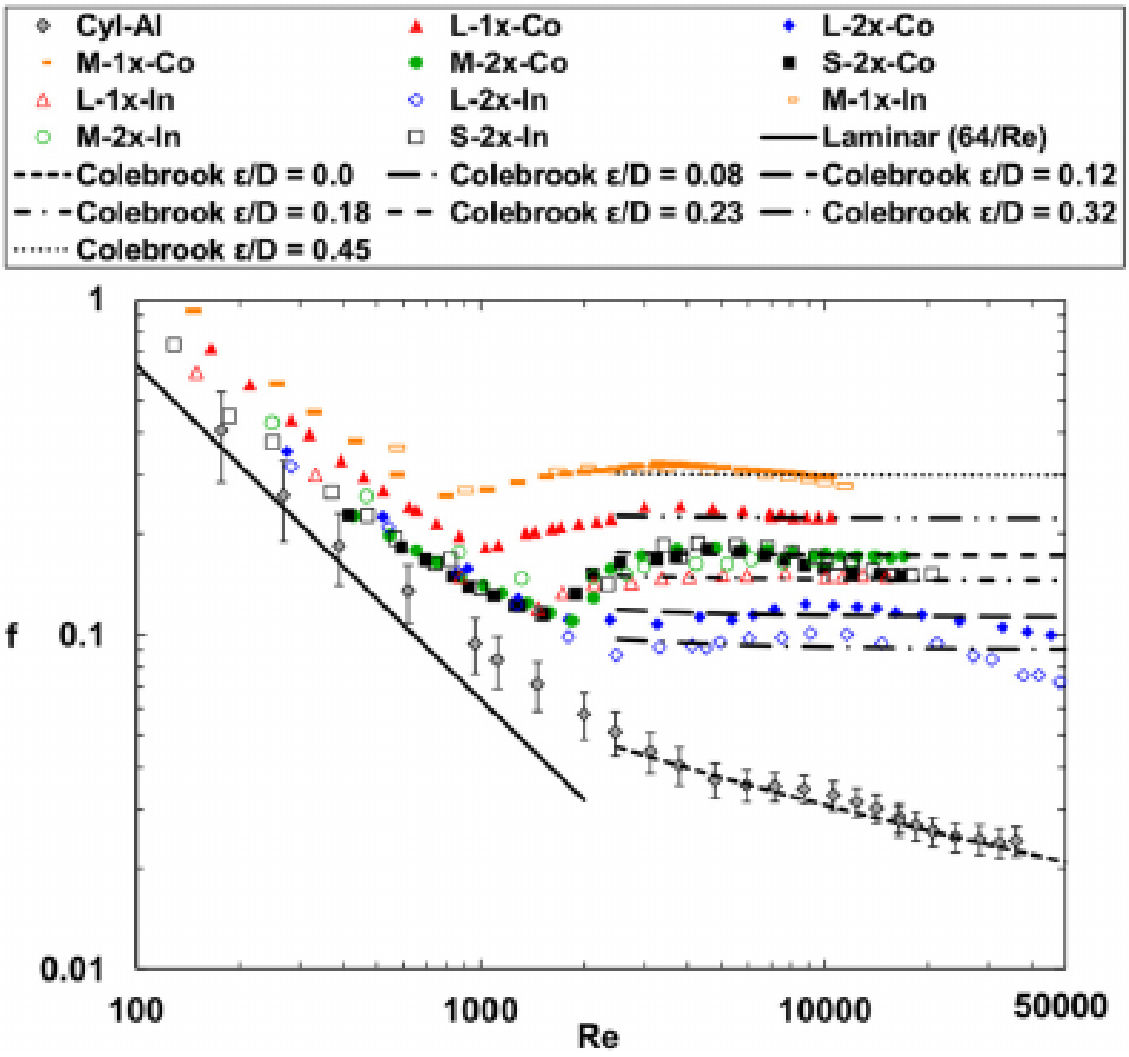

Figure 2.5: Stimpson et al. [62] experiment results

The figure presents results from the studied rough microchannels (coloured markers), a smooth control channel (Cyl-Al, a cylindrical aluminium channel) and the theoretical predictions for a variety of relative roughnesses. The friction factors were derived from the Colebrook equation using the measured pressure drop, and plotted to be compared to their theoretically matching relative roughness.

Firstly, it can be noted that the smooth aluminium channel reliably follows the predicted friction factor. Although it shows some divergence in the transition from laminar to turbulent, the friction factor is generally in good accordance with theoretical levels for $\epsilon/D = 0.0$.

The rough samples however, show a deviation from the theory for laminar flow. More interestingly, the friction factor shows some dependency on surface roughness in the laminar flow regime. This is in contrast to the theoretical $f = 64/Re$, that suggests friction factor is constant for all tubes in the laminar regime. Stimpson et al. [62] determined the hydraulic diameter of the channels using CT scans and found that the absolute roughness ϵ was approximately an order of magnitude higher than the measured arithmetic mean roughness R_a. They further note that the friction factor is highly dependent on hydraulic diameter, which underscores

the importance of dimensional accuracy for both controlling and verifying the pressure loss through a channel.

It is highlighted by Stimpson et al. that very few studies examine flow in small channels, and fewer still look at high relative roughness channels. Some papers will cite the fact that predicting pressure drop in small channels is simply not possible as one of the motivations to look into post processing methods such as chemical milling [27]. However, efforts to relate the friction factor or pressure drop to various surface roughness metrics do not exist, and would be able to provide a better understanding to how these characteristics influence each other. In order to perform such a study, it is important to understand what metrics and methods are available to quantify surface roughness. section 2.3 and section 2.4 take a closer look at this.

Effective Hydraulic Diameter

One assumption made by Moody when modelling the Colebrook equation into the Moody chart, is that the full diameter of the pipe is available to the flow. However, in high roughness pipes, the effective diameter available to the flow may be reduced due to flow separation induced by surface irregularities. Kandlikar [38] proposed a modified Moody chart based on the concept of a constricted hydraulic diameter $D_{h,cf}$. This constricted diameter accounts for the fact that, for higher roughness levels (with respect to the available cross sectional area), the flow effectively "sees" a lower available area through which it can pass. Kandlikar defines this constricted diameter for a pipe with circular cross section as:

$$D_{h,cf} = D_h - \epsilon \tag{2.4}$$

Where ϵ represents the average surface height. The corresponding flow Reynolds number and Darcy friction factors are then defined as:

$$Re_{cf} = \frac{\rho v D_{h,cf}}{\mu} \tag{2.5}$$

$$f_{D,cf} = \frac{2\Delta p D_{h,cf}}{L\rho v^2} \tag{2.6}$$

Note that if the flow speed v is derived from a mass/volumetric flow, it should also account for a constricted flow area. This led to an adapted version of the Moody chart, accounting for the constriction of flow at higher roughness levels (shown in Figure 2.6. The correction for flow constriction reduced the effective friction factor with respect to the original Moody chart (see Figure 2.4), because $D_{h,cf} < D_h$ in equation Equation 2.6.

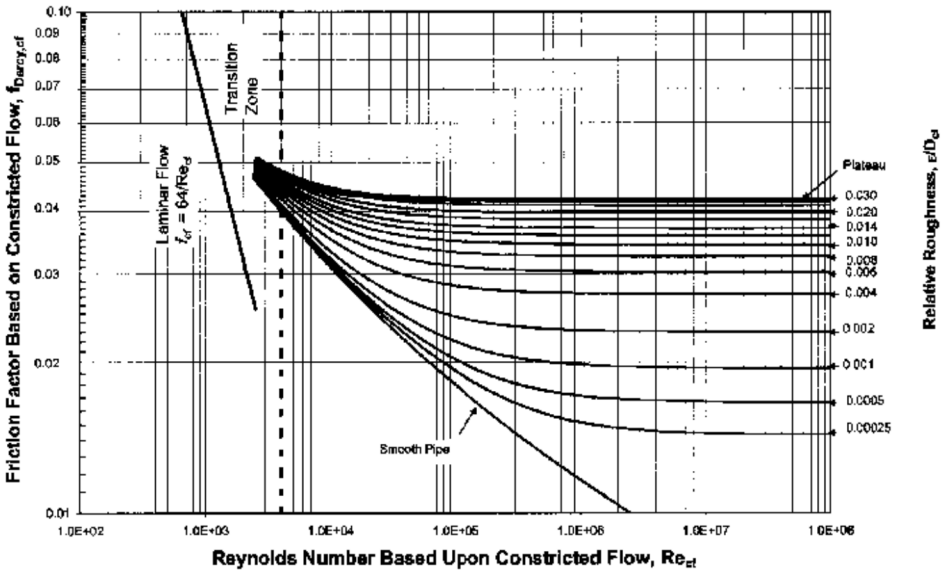

Figure 2.6: Darcy friction factor representation based on constricted flow diameter [38]

The difference between using a theoretical D_h and an effective Dh, cf may depend on the relative roughness. At higher relative roughnesses, the difference between these two approaches may be larger then in pipes where the roughness is very low compared to the diameter. The results presented in this study will be analyzed using both full and constricted flow assumptions in order to assess this difference.

Surface polishing

Due to various reasons (further discussed in section 2.5), additively manufactured metal surfaces tend to have a high surface roughness (compared to traditionally manufactured surfaces). At times, the prediction of pressure drops resulting from this roughness is even discarded as being impossible to estimate [27]. This can be remedied with a number of processes such as use of contour tracks, surface re-melting or post-processing using conventional methods such as machining. Unfortunately these post-processing techniques are not always applicable to internal geometries (machining for example cannot easily reach them). Another method for post-processing surface quality are electrochemical-based methods. That being said, there is currently no effective method available in the literature for electro-polishing of internal surfaces with various designs and geometrical features. This is because the electro-polishing process requires a comprehensive understanding and optimization for each geometry [10]. This means that, while the use of chemical processing might make it less relevant to relate print settings to expected pressure drops, there is still a need for understanding how the part geometry and print settings affect the as-built surface roughness. section 2.3 discusses how surface roughness is quantified using a variety of metrics. These metrics are then used in subsection 2.5.1 to describe the phenomena that typically occur in L-PBF printing and are at the source of surface roughness.

2.3 Surface Roughness Metrics

Surface roughness parameters, also referred to as surface texture parameters, are metrics used to quantify the geometric properties of surfaces. They are widely used to measure surface roughness in the context of research, where the goal is often to understand the influence

various processing parameters/manufacturing practices have on the resulting surface finish, or to relate surface roughness to part performance. Increasing part performance through the use of post-processing techniques (such as chemical milling) might also require the quantification of a baseline roughness level. While a subset of existing parameters are also widely used for validating that a manufactured part conforms with the requirements on surface finish, a much larger set of parameters are typically used in the context of research and analysis. The relevance of each depends on the topic of research, and it is useful to further subdivide these parameters according to a few characteristics before explaining them in more detail.

A first distinction can be made between linear and areal parameters. Linear parameters are defined by measuring the surface height variation along one line. This can be done using less sampled data, which enables the use of relatively simple and low cost equipment such as contact profilometers. In contrast, areal parameters use the surface height variations of a two-dimensional plane on a measured surface. These take into account a larger data set, and have more recently been popularized thanks to advances in measurement technologies (see section 2.4). Since both linear and areal parameters rely on the analysis of surface height variations, most linear parameters have an areal equivalent. The areal parameters permit further analysis such as volume based metrics, that are not possible with one-dimensional data sets. Because the data used for areal metrics represents a significantly larger sample then linear metrics, they are often able to be more representative of the part surface.

These parameters are officially referred to as profile and areal texture parameters, and are defined in ISO 4287 [1] and ISO 25187-2 [2] respectively. Parameters are then further subdivided into the type of information they provide, or require. For example, depending on the input data, profile parameters are either referred to as primary, roughness, or waviness parameters [75]. On the flip side, areal parameters are primarily categorized into field and feature parameters. Where field parameters are calculated using every data point in a sampled data set, feature parameters use data segmentation to separate features into an isolated data set. Both can then separately be analyzed in order to remove the influence of unique features on general surface roughness.

As a result mostly of historical development of the field of texture metrology in different disciplines, there exists a very large number of different parameters. While this gives the impression that each parameter has a specific use case and utility of its own, it should be noted that some of these parameters are functionally very similar. According to [76], values of Ra and Rq differ only marginally, and there is no evidence that different parameters of the same type yield *functionally* different results.

2.3.1 Profile Texture Parameters

Profile texture parameters are commonly used in the manufacturing industry, including the additive manufacturing sector. According to a survey by Todhunter et al. in 2017 [71], over 90% of participants reported using the most common profile parameters. Profile parameters are derived from surface height deviations from the surface form along a predefined linear track. This section provides information on the characteristics and definition of profile parameters.

Primary, Roughness and Waviness Parameters

Profile parameters are measured along a linear surface track, and different parameters are calculated and/or filtered based on the track length used. During a measurement, the traversing length, assessment length, and sampling length are distinguished [75]. The traversing length is the full length over which measuring equipment is in contact with the surface, and includes periods of acceleration to get up to constant speed. The actual usable data is contained in the assessment length. The sampling length is the smallest distance over which a surface parameter is assessed, and it can be smaller than the assessment length.

The sampling length is typically set to filter out waviness, a larger wavelength oscillation in surface form deviations, while being short enough to reliably determine a parameter [75]. Waviness is the reason why profile parameters are divided into primary (P), roughness (R), and waviness (W) parameters. Primary parameters account for both roughness and waviness characteristics of the surface, while roughness and waviness parameters are calculated by filtering the counterpart out of the measurement using, for example, the sampling lengths. Whitehouse [75] suggests that if the waviness is a result of machine imperfections that are not the subject of the research, they should be separately considered from roughness. However, the relevance of this distinction depends on the influence of waviness on the performance of the part in its final application.

After deciding whether or not to consider roughness and waviness separately and how to determine the cut-off wavelength, various parameters are available, falling under four categories: height, hybrid, functional, and spacing parameters. Height and hybrid parameters are the most widely used and discussed in this section. Height parameters relate to the variations in height of the chosen sampling track, while hybrid parameters are derived from secondary characteristics like surface slope. It is important to note that the same formulas can be used to determine the equivalent primary or waviness parameters using different filtering and cut-off approaches.

Height Parameters

As previously mentioned, Ra is the most commonly used profile roughness parameter across a variety of industries. The metrology calibration industry is the largest user, accounting for 97% of surveyed usage. However, over 90% of the automotive, aerospace, electronics, and product manufacturing industries also report using the parameter.

When a surface deviates from the intended design surface, certain points on the surface will be above the intended profile, while others will be below it. The local maxima and minima resulting from these deviations are called peaks and valleys, and the surface height eventually averages out to a mean line. This mean line is the reference line with respect to which most profile parameters are defined.

Ra represents the "arithmetic mean of the magnitude of the deviation of the profile from the mean line" [76]. In other words, if all negative surface deviations were made positive, Ra would bisect the surface profile such that an equal amount of material lies above and below it. Mathematically, Ra is defined as follows [76]:

$$Ra = \frac{1}{l_r} \int_0^{l_r} z(x)dx \tag{2.7}$$

Where z(x) represents the profile height deviation from the surface form, and lr is the sampling length. To obtain a more representative figure of the analyzed surface, the average over multiple cut-offs or sampling lengths can be used. Alternatively, the roughness profile R can be characterized using the root-mean-square (rms) of the deviations instead of an average of absolutes. According to Whitehouse [76], rms differs from Ra in that it is more easily relatable to functional performance. In this case, it is denoted as Rq and calculated using Equation 2.8:

$$Rq = \sqrt{\frac{1}{l_r} \int_0^{l_w} z(x)^2 dx} \tag{2.8}$$

The Rq parameter may be larger than Ra by 10% to 25%, depending on the surface and measurement technique used [76]. Moving on to other profile parameters, Rp and Rv are used to represent the maximum peak height and valley depth, respectively. Rz is then used to denote the maximum peak-to-valley height within one sampling length, while Rt is the peak-to-valley height determined over the entire assessment length. Both Rz and Rt are calculated by adding the magnitudes of the deviations from the surface form of the highest and lowest surface peaks.

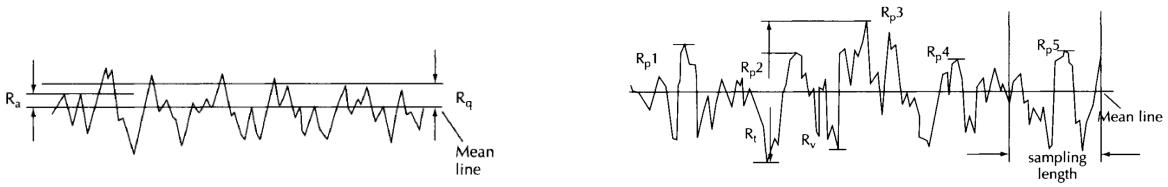

(a) R_a, R_q **(b)** R_p, R_v, R_t, R_z

Figure 2.7: Overview of profile height parameters [75]

Hybrid Profile Parameters

Profile texture parameters are limited to measuring height variations along a single direction, which makes them one-dimensional analysis tools. However, in reality, surface topography is characterized by height variations on a two-dimensional surface. If the goal is to predict part performance or better understand the mechanisms influencing surface texture, a three-dimensional analysis can provide a much larger set of information. Areal texture parameters, as defined in ISO 25178-2 [1], were intended to measure surface height variations along the two dimensions of a surface, allowing for a more complete picture of the surface. These parameters are also referred to as 3D texture parameters, but for the purposes of this literature review, they will be referred to as areal texture parameters.

One-dimensional measurements might capture a less complete picture of the sample surface, as a single line might not be representative enough of the variations across the whole area. Areal measurements provide a much clearer picture of the overall surface, making surface anomalies easier to analyze. Figure 4.3 compares an areal and profile analysis of the same surface.

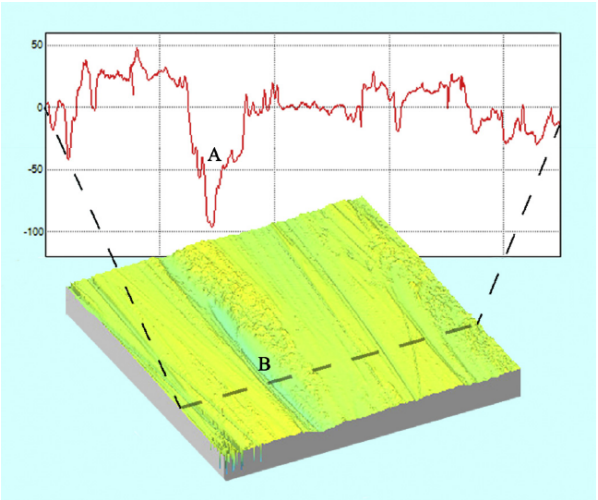

Figure 2.8: Profile and Areal Surface Analysis [72]

The top figure of the profile analysis shows signs of a pit, groove or scratch at a specific point A. When the directional profile is appropriately chosen, it can identify unusual features such as the one displayed in this figure. However, in many cases, obtaining significant information about the anomaly using the profile analysis can be challenging. Conversely, the areal analysis at the bottom provides a clear indication that the anomaly is caused by a scratch [72]. Had the profile analysis been more aligned with the groove rather than being perpendicular, it may not have identified the anomaly, or it might have returned results that are difficult to interpret, depending on the angle between the scratch and the track. This demonstrates that while profile measurements are easier to use and more straightforward, they come at the cost of incomplete information. ISO 25178-2 [1] presents several areal texture parameters that can generate a more thorough analysis of surface roughness. Similar to profile parameters, areal parameters are categorized into several groups. Areal characteristics are mainly classified as field or feature parameters. Field parameters are calculated using all points in the measurement data set and consist mainly of height, functional, and hybrid parameters. Feature parameters are reliant on the segmentation of the data set into individual features and a feature-deprived data set, and pertain to the individual examination of both data sets.

Despite requiring more advanced and expensive measurement equipment, the industrial survey of 2017 [71] shows that areal field parameters have been widely adopted across various industries, with 56% of participants reporting their use, and up to 13% reporting their use of areal feature parameters. The most commonly used areal parameters are equivalent to the earlier mentioned profile height parameters Ra, Rz, and Rq, namely Sa, Sz, and Sq.

Areal Field Parameters

Areal height parameters are similar to their profile counterparts in terms of calculation. The only difference lies in the fact that data is collected over a sampling area instead of a linear sample track. According to Leach [45], the arithmetic mean height and root mean square height of a sampling area can be calculated as:

$$
\begin{aligned}
S_a &= \frac{1}{A} \iint_A z(x,y)dxdy \\
S_q &= \sqrt{\frac{1}{A} \iint_A z(x,y)dxdy}
\end{aligned}
\tag{2.9}
$$

In the calculation of areal height parameters, the key difference from their profile equivalents is that the measurement data is collected over an area rather than a linear track. Leach [45] provides formulas for calculating the arithmetic mean height and root mean square height over the sampling area A, which is dependent on the sampling lengths along the x and y axes. Similar to profile texture parameters, Leach notes that the root mean square parameter is often more closely related to functional performance. The areal equivalent of the maximum surface height parameter Sz is defined as the sum of the absolute values of the maximum peak height Sp and valley depth Sv. Notably, in areal surface analysis, there is no differentiation between assessment length and sampling length, so the areal equivalents of Rt and Rz are combined into a single parameter, Sz.

$$
S_z = S_p + |S_v| \tag{2.10}
$$

Although profile skewness and kurtosis are considered hybrid parameters, Whitehouse [76] classifies the areal equivalents as height parameters. They are calculated with:

$$
\begin{aligned}
S_{sk} &= \frac{1}{S_q^3} \frac{1}{A} \iint_A z^3(x,y)dxdy \\
S_{sk} &= \frac{1}{S_q^4} \frac{1}{A} \iint_A z^4(x,y)dxdy
\end{aligned}
\tag{2.11}
$$

2.3.2 Sand Grain Roughness

As reviewed in previous sections, modern day measurement equipment allows for the measurement of a variety of surface roughness parameters such as Sa, Sq, and Sz. While they allow surface roughness to be characterized and interpreted in a variety of ways, they all depend on either a linear or areal height map of the measured surface. This stands in contrast however to the definition of "absolute roughness" in the Colebrook equation (Equation 2.3), used to define the relative roughness of the widely used Moody charts (see section 2.2). This relative roughness is calculated using the hydraulic diameter D_h and the "absolute roughness", or sand grain roughness, ϵ. The use of ϵ for the definition of the Moody charts stems from the fact that the experimental data generated by Nikuradse in 1933 [53], and subsequently used by Colebrook in 1939 [22], was obtained by coating several pipes with sand grains of differing average diameter. The average diameter of the sand grains used in a pipe came to be defined as the sand grain roughness [9], and was subsequently referenced to as "absolute roughness" by Moody [47].

As a result, the sand-grain roughness is not a surface property that can be derived directly from measurement data of additively manufactured surfaces, whose texture is highly irregular in comparison to sand coated surfaces. This makes it difficult to translate data on from existing surface/channel to a point on the Moody chart in order to derive its friction factor and subsequently predict pressure drops. Later revisions of the Moody chart, such as the one proposed by Kandlikar [38] and discussed in section 2.2, used the height of the saw tooth used to generate the rough surface to characterize the head loss using an equivalent sand grain roughness. While this method enables the resulting chart to be compared to Moody's original

chart, the regularity of the roughness in their samples is not representative of L-PBF printed surfaces.

Relations have been proposed for a so-called *equivalent* sand grain roughness, which provide a conversion between the sand grain roughness ϵ and some typically measured roughness parameters discussed in this chapter. Adams et al. [9] performed a series of flow measurements on pipes, and determined conversion factors to establish a relation between parameters Ra, R_{RMS}, Rzd and the experimentally determined sand grain roughness ϵ_{exp}. Here, the sand grain roughness can be explicitly solved for using the Colebrook equation, because the Darcy friction factor was determined using pressure drop data from the experiment:

$$\left(\frac{\epsilon}{D_h}\right) = \epsilon_{rel} = 3.7\left(10^{\frac{-1}{\sqrt{f}}} - \frac{2.51}{Re}\sqrt{f}\right) \tag{2.12}$$

It should be noted however, that the intent is still to convert roughness parameters of a highly irregular surface to an equivalent value comparable to surfaces coated in sand grains. Furthermore, the relations found here apply to linear parameters, and have not been proven applicable to areal parameters. As concluded by Adams et al. [9], the track employed by a profilometer can have a big influence on the conversion factor. Depending on the scan direction, ϵ was found to be between a factor of 5.8 to 11 times higher than Ra. This dependency on scan direction suggest that areal parameters might provide more consistent at calculating an equivalent sand grain roughness.

2.4 Surface Roughness Metrology

The experiments carried out in the context of this thesis include the measurement of surface roughness on additively manufactured metallic samples. To provide background on the methodology and equipment used to this end, this section gives a brief overview of measurement technologies and their main characteristics.

The large majority of measurement approaches are either contact based, non-contact optical, and non-contact non-optical. Contact based techniques involve some form of direct contact between the measuring equipment and the measured surface, while non-contact techniques assess the surface without physically interacting with it. Optical approaches involve using visible light to form a topography image, while non-optical approaches use other parts of the radiometric spectrum. The technologies listed in Table 2.2 have been used in the context of Metal AM surface topography analysis [72][80][48]:

Table 2.2: Overview of common surface roughness measurement technologies

Contact based	**NC - Optical**	**NC - Non-Optical**
Contact Profilometry	Microscopy - Optical	Scanning Electron Microscopy
	Microscopy - Confocal	X-ray Computed Tomography
	Microscopy - Focus Variation	X-ray Diffraction
	Interferometry - Coherence Scanning	Energy Dispersive Spectroscopy
	Interferometry - Structured Light	Atomic Force Microscopy
	(High Speed) Digital Camera	
	Conoscopic Holography	

The majority of optical measurement techniques fall under either microscopy or interferometry [72]. Microscopy techniques include optical, confocal and focus variation microscopy, and

rely on magnified imaging to determine surface roughness [73][52]. Interferometry mainly consists of deriving surface roughness characteristics from the interactions between different light waves [25] and is commonly done using white light, in which case it may be referred to as white light interferometry (WLI) [43]. Optical measurement techniques present a few advantages over contact based methods. The lack of physical contact rules out any mechanical filtering, resulting in a more accurate representation of the measured section. In addition, the measurement path is less constrained. This makes it possible to acquire topography scans of entire sampling areas, and prevents the need for extrapolating the results of a small section to the entire geometry. Using optics to measure surface roughness does introduce additional complications that need to be taken into account. The reflective properties of a part will depend on the manufacturing process, and need to be taken into account for each measured surface [72].

Contact-based and optical methods are typically used for generating quantitative data from which roughness metrics can be derived. Non-contact non-optical methods such as SEM have generally been used mostly as a qualitative supplemental data set, although recent advances in data processing have allowed the quantitative use of data from tomographies. The selection of a measurement strategy depends primarily on the type of data that is required. Contact-based methods suffice if profile parameters are to be determined, but for calculating areal parameters it is essential to have optical measurement capabilities.

In a comparative analysis of the primary optical methods, Tato et al.[67] provides insight on how coherence scanning interferomety (CSI), confocal microscopy (CONF/C-CONF) and focus variation (FV) compare in terms of measurement results. In terms of calculating area texture parameters, the four optical methods showed relatively little variation. Height (Sq, Ssk, Sku, Sa), spatial (Sal) and functional (Vmp, Vvv) parameters showed less than 8% deviation across different measurement technologies. An exception was found in the calculation of developed surface area, where more inconsistencies between measurement techniques were present.

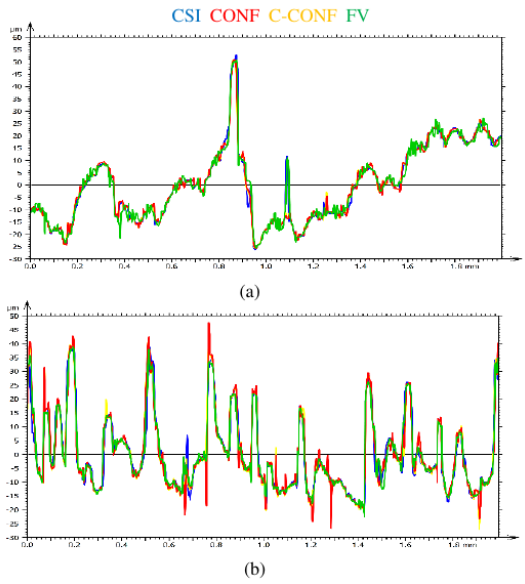

(a) top: surface B [0-deg]; bottom: surface W [90-deg]

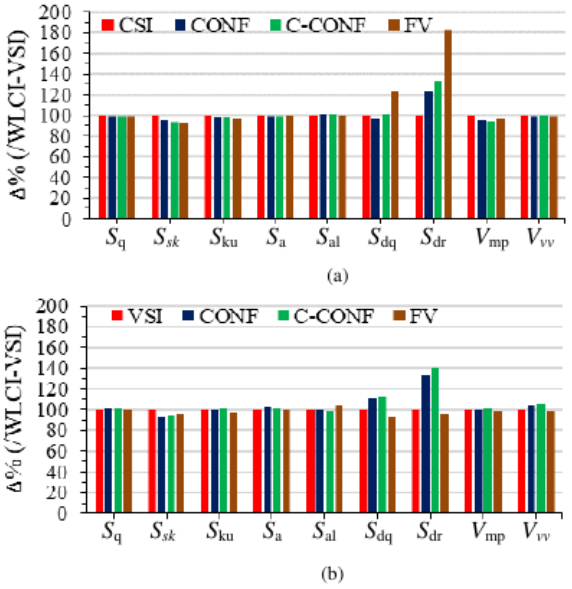

(b) Measurement discrepancies in areal texture parameters, compared to reference CSI data

Figure 2.9: Comparative study of optical measurement techniques[67]

Each of these measurement techniques also presents different advantages in terms of speed, cost, availability and accuracy. In combination with the part geometry, these parameters should eventually be weighed to determine what the best measurement strategy is. The literature study performed prior to this masters thesis [68] provides a more in depth analysis of each of these methods. In the context of this thesis, selection was additionally done considering the available equipment, and is further discussed in subsection 3.8.2.

2.5 Processing Parameters and Print Effects

This section gives an overview of the most important processing parameters and discusses their relation to main elements of surface roughness. Discussion was kept to the processing parameters relevant to this experimental study. For a more in depth study on the effects of all processing parameters, the reader is referred to [68].

2.5.1 Common Print Defects

Stairstep effect

The stairstep effect is the most commonly observed type of roughness in L-PBF printing, and is a direct result of the layered approach to melting the powder. Since each layer is melted separately on top of previous layers, any exposed surface which contains a transition from layer to layer will contain a small ridge. This means horizontal surfaces do not exhibit this effect. On the other hand, vertical and inclined surfaces, depending on the build angle, will experience an increased surface roughness. Many studies note this effect to be of largest impact on the roughness of upskin L-PBF surfaces, specifically for inclined up-skin surfaces. Figure 2.10 illustrates how the layered approach to L-PBF printing results in a stair-like profile for an inclined surface.

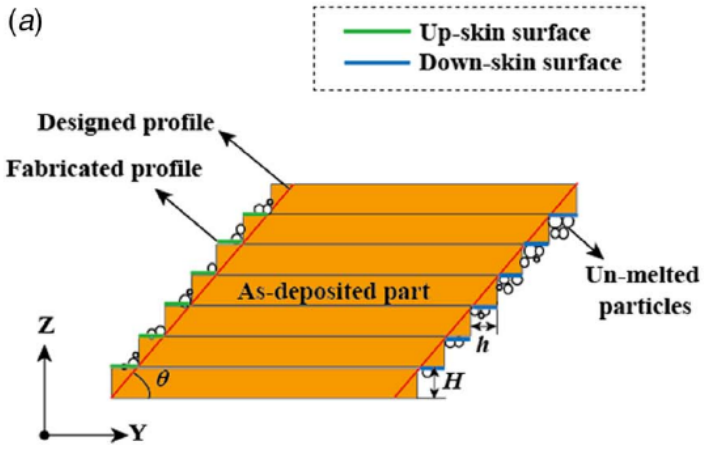

Figure 2.10: Stairstep effect visualization [80]

As can be seen, there are two main processing parameters that influence the characteristics of the stairstep effect: the build angle θ, and the layer height H (the layer overhang/offset h being a result of their combination). The build angle represents the angle of a printed surface as measured from the horizontal plane. A diagram of these build angles for the sample printed in the context of this research can be found in Figure 3.2 As a result of this effect, every down-skin (DS) surface printed under an angle also contains small horizontal

overhangs. Therefore, in addition to the surface roughness induced by the stairstep profile, DS inclined surfaces are additionally susceptible to surface roughness effects on these horizontal overhangs like dross: the melt pool penetrates too deep as a result of being printed over powder [61], and drops lower due to gravity [19]. As can be seen in Figure 2.10 however, the increased amount of un-melted particles on the down-facing skin sections actually serve to some degree as a compensation for the step-profile by reducing the effective step height.

It has been widely shown that the stair-step effect exhibits a strong dependency on the build angle, and is a major contributor to the overall dependency of surface roughness on build angle [63][80]. Figure 2.10 shows how additionally, the layer thickness can be used to reduce the impact of this effect. Strano et al. [64] explain that, from a theoretical standpoint, the stairstep induced roughness can be modelled purely based on layer thickness and sloping angle using:

$$R_a = \frac{1}{L}\int_0^L |y(x)|dx = \frac{1}{4}L_t \cos(\alpha) \tag{2.13}$$

Where L_t is the layer thickness and α is the build angle. This model reduces in accuracy as the slope increases and gives way to other sources of surface roughness (e.g. increased amount of unmelted particles on vertical surfaces [51], dross on down-skin surfaces [19][81]). The variations of surface roughness with respect to build angle are discussed in more detail in subsection 2.5.4.

Balling and Spattering

Melt pool stability and track continuity play a big role in controlling surface roughness of as-built L-PBF parts. A stable melt pool will exhibit the formation of continuous tracks, which improve surface roughness. However if the laser power, speed or combination thereof is not properly optimized, the melt pool may become too viscous. Discontinuous tracks as a results of roughness sources like balling have a significant impact on surface roughness, but an equally great impact on the ability to deposit powder of future layers on a freshly melted layer uniformally [35]. As a result, the balling phenomenon and its impact have been widely researched.

Gu and Shen [35] make a distinction between first line scan balling (FLSB), and later line scans. A steeper thermal gradient is usually found on the initial scan track as it is printed directly on the powder bed. This increased gradient typically results in higher surface tension, which will cause the melt pool to fragment into spherical agglomerates in order to reduce surface energy. A a consequence of significant balling on the initial scan track, the powder deposition of future layers can be disturbed. Adjusting the powder bed temperature to optimize this surface tension may alleviate this effect on initial scan tracks, though with L-PBF this is mostly done when printing high conductivity alloys like copper [35] or Aluminum [19]. A further distinction is made by Gu and Shen based on the origin of the phenomenon: 'shrinkage-induced balling' and 'self balling'. Shrinkage-induced balling occurs when an excessively viscous melt pool fragments in order to reduce its surface energy. This is typically observed when the laser power is too low, or the speed to high. While laser power and speed are the primary influencing factors, balling can be limited by reducing the oxygen content of the atmosphere to 0.1% [55].

Conversely, at excessive laser powers or too slow laser speeds the energy absorbed by the melt pool risks becoming excessive, resulting in spatter. When excessive energy input is applied to a melt pool, the material conductivity may not be high enough to transfer heat away from the laser focus, resulting the vaporization of the center part of the melt pool. The vaporization

of metal on the top surface of the melt pool exerts a pressure on the melt pool, called recoil pressure. While low amounts of recoil pressure aid in flattening the melt pool surface, Kruth et al. [40] explains that excessive recoil pressure can cause the ejection of liquid droplets. Figure 2.11 shows the how the liquid spatter due to recoil pressure is ejected at the tail-end of the laser [48]. Note that the ejection of un-melted powder ahead of the laser is typically referred to as powder denudation [49], and is discussed in subsection 2.5.2.

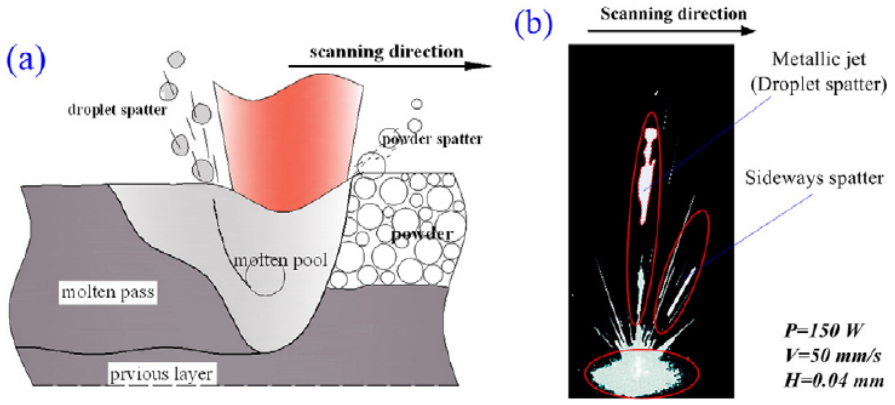

Figure 2.11: (a) Schematic of spatter formation; (b) High speed camera shot of typical spatter behaviour [48]

The experiment performed by Gu and Shen [35] exhibited melt pool stability at a power/speed combination of 400 W/0.04 m/s. When increasing the speed to 0.06 m/s the scan track was shown to break up into metallic balls with a mean diameter of 400 μm, an example of shrinkage-induced balling. Liu et al. [48] explain that the input energy density is the most influential parameter when it comes to spatter behavior. When increasing the laser power to 425 W, Gu and Shen [35] found that the scan track was also discontinuous but instead, a large number of small metallic balls in the order of 10 μm could be found around the track. This is an example of spattering induced by excessive energy input. Figure 2.14 shows SEM scans of all three scenarios.

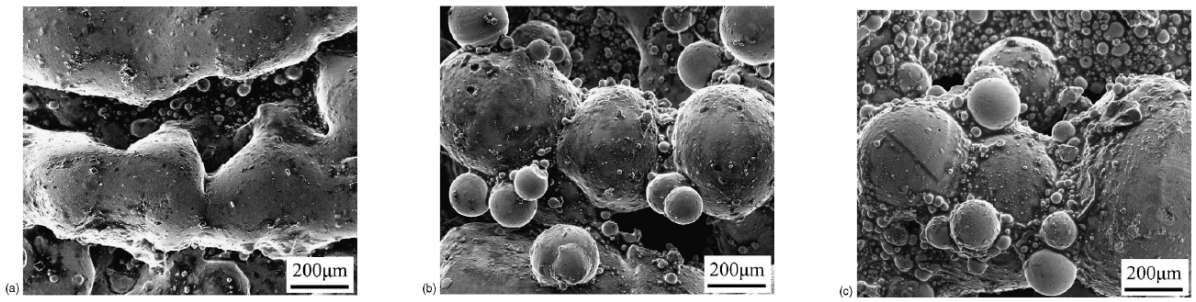

(a) P = 400 W, v = 0.04 m/s **(b)** P = 400 W, v = 0.06 m/s **(c)** P = 425 W, v = 0.04 m/s

Figure 2.12: continuous scan track (left), the shrinkage-induced balling (middle) and the spatter-induced balling (right) [35]

Tian et al. [70] reviewed the effect of processing parameters on the surface roughness of L-PBF printed Hastelloy-X and found that with a laser power of 170W, continuous tracks could be observed at speeds between 1100 mm/s and 2300 mm/s. For 270W, the upper limit for continuous tracks extended to 2700 mm/s. For 370W, continuous tracks could be observed up to 3100 mm/s. This is consistent with the fact that a minimum amount of energy input is

required to properly melt material. The higher the input power is, the less exposure time is required to melt powder, and the faster the laser can go. The lower and upper energy input limits found by Tian et al. [70] corresponded with the settings for which balling and spattering occurred respectively.

Dross

Dross is a type of surface texture that is specific to downskin surfaces, and is typically the largest scale of surface roughness found on as-built L-PBF parts [19]. The particularity of overhanging or downskin surfaces stems from the fact that the to-be-molten layer is printed above powder, as opposed to a substrate or a previously solidified layer. As a result, the thermal properties are different and the melt pool becomes more difficult to control. Generally, dross is a direct consequence of excessive energy input causing the melt pool to locally penetrate deeper than intended [61], as well as gravity and the lack of supportive material underneath causing molten particles to drop lower [19][81]. Tian et al. [70] analysed the dross effect on a 45° overhanging edge at laser powers and scan speeds. Figure 2.13 shows a schematic of the dross roughness below an overhanging edge (left), as well as a micrograph cross section of the Hastelloy-x sample on the right.

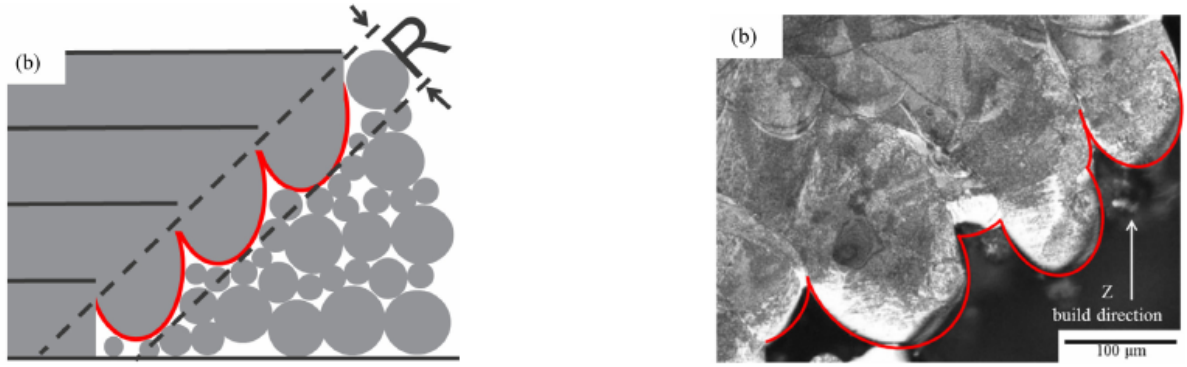

(a) P = 390 W, v = 1990 mm/s

(b) P = 390 W, v = 1990 mm/s

Figure 2.13: Higher power, lower speed. Left: dross schematic, Right: SEM scan of 45° overhang dross.[70]

As can be seen, the protruding elements are of significant scale: the surface peak-to-valley distance at 370 W and 1900 mm/s can be in the order of 100 μm. Similarly to the balling effect, the characteristics of dross are dependent on the selection of processing parameters. As could be expected from general trends in melt pool physics, Tian et al. found that the melt pool depth increases with increasing laser power and decreasing scan speeds, both consistent with an increased input energy density. An interesting measure is the comparison of the melt pool depth to the median powder particle size. By analysing down skin surface roughness for different melt pool depths, it was found that the best surface roughness was achieved when the depth is similar to the mean particle size. This is reasoned to be because the melting only covers one layer of powder, resulting in a minimized melt pool surface contour. The same experiment confirmed this by reducing the laser power and increasing speed to 200 W and 3000 mm/s respectively.

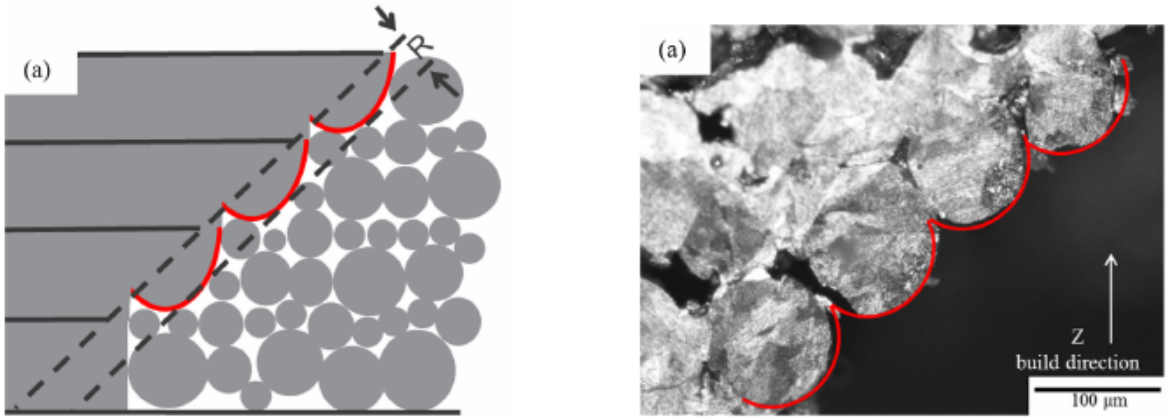

(a) P = 200 W, v = 3000 mm/s

(b) P = 200 W, v = 3000 mm/s

Figure 2.14: Lower power, higher speed. Left: dross schematic, Right: SEM scan of 45° overhang dross.[70]

This adapted power/speed combination represents a 66% reduction in linear energy density. This reduction in input energy results in a smaller melt pool, an change that has also been shown to reduce dross formation in L-PBF printing of titanium (Ti6Al4V) samples [20]. In the experiment performed by Tian et al. [70], the processing parameters were tuned in order to achieve a melt pool depth of $30\mu m$, equal to the median powder particle diameter. The result shows how the laser power and speed can indeed be used to minimize the down skin surface melt pool depth. A lower power level and higher speed result in a reduced energy density input. This reduces the melt pool depth and surface contour, resulting in an overall smoother surface.

2.5.2 Gas flow and Denudation

Denudation is very similar to spatter in that it concerns the ejection/entrainment of particles as a result of physical phenomena related to the melting process. It is sometimes referred to as powder spatter, but for purposes of clarity will be called denudation hereafter. Where spatter concerns the ejection of molten particles from the melt pool (see section 2.5.1), denudation refers the the ejection or entrainment of un-melted particles ahead of the laser spot and on either side of a track. It is primarily caused by the modification of the nominal gas flow by the metal vapour [21]. As a result the nominal gas flow itself is one of the driving forces behind denudation [49]. Note that the influence of denudation on surface roughness concerns primarily top/horizontal surfaces.

To prevent oxidation of the metals during printing, L-PBF machines typically fill the process chamber with an inert gas. A constant flow of this gas is maintained through the process chamber to ensure the removal of soot which would otherwise spread through the chamber. Roidl et al. [57] explain how a well designed gas flow can prevent soot from spreading through the chamber and potentially obstructing the laser. This would reduce the effective power and distort the laser (reflecting it off expelled powder). In combination with a good scanning strategy, a good gas flow can also help prevent the creation of ejecta and contact with the laser beam. Gas flow characteristics are also closely related to the denudation of powder (i.e. the removal of powder particles around the melt track before they are molten). Matthews et al. [49] determined that the denudation zone, which has a significant influence on the surface quality, shows a strong correlation to the gas pressure. This is because a portion of the entrained particles may end up in the melt pool as it re-solidied, causing the appearance of unmelted

particles on the surface. Matthews et al. confirmed this to be the case by observing the melt process with a high speed camera. Figure 2.15 shows how the width of the denudation zone (DZ) changes with gas pressure. Here, the denudation zone width measures the extent to which powder is removed on either side of the melt track.

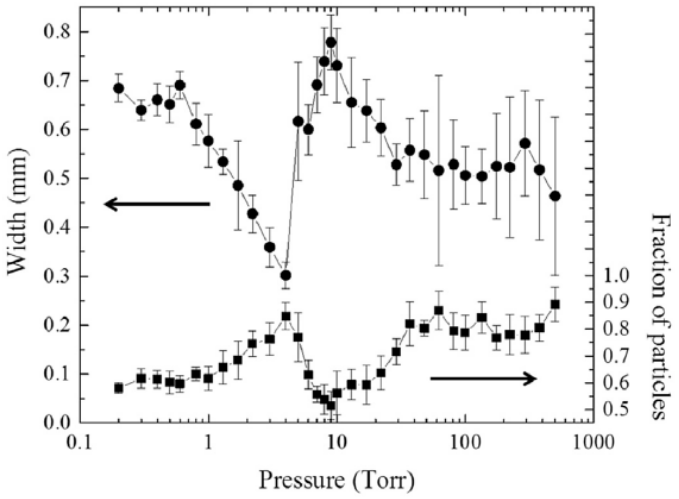

Figure 2.15: Denuded zone with as function of gas (Ar) pressure (Torr) [49]

It was found that with decreasing pressure, the DZ width increases to 0.8mm until a pressure of 10 Torr. It then decreases to 0.3mm at a pressure of 4 Torr, after which it increases again to 0.7 mm. According to Matthews et al., this pressure corresponds to the point at which the drag force on the particles reduces to a point where the particle motion is reversed and dominated by other sources. At lower pressures, it was theorized that motion becomes influenced either by tangentially vaporizing particles, or by an undulating melt pool that directs metal vapor flow along the surface.

2.5.3 Recoater blade

The recoater arm and recoating speed have recently also been found to influence surface roughness. The recoater arm is used to distribute powder in a compact layer before the melting process. As a result, its properties can have a large influence on the printing process [24]. Recoater materials typically include steel, ceramic, carbon and silicone [24][60]. The recoater arm is discussed in this section because its influence on the surface roughness of L-PBF parts is tightly connected to the spreadability of powder. Brika et al. [17] note that flowability is not a powder property, but a function of the ability of powder to flow in a desired manner. In order to quantify this, Snow et al. [60] assessed powder flowability based on four parameters, two of which provide insight on how the surface roughness might be affected: Build plate coverage percentage $\%C$, powder deposition rate $\dot{m}$. Generally, it is desirable to have a highly flowable powder to improve surface quality [17][60]. Ideally then these metrics should behave like those of a highly flowable powder, meaning high cover percentages and deposition rates are preferrable.

Snow et al. [60] performed various measurements on the first layer deposition of three Al-10Si-0.5Mg powders (with different particle size distributions) in order to assess these parameters. Experiments were repeated with two recoater arm materials (steel and silicone), two layer thicknesses (40 μm and 80 μm), and two recoating speeds (50 mm/s and 150 mm/s). The

table below summarizes the values of the parameters that were varied. Note that the powders are here differentiated by their angle of repose. This is defined as the steepest slope of the unconfined material, measured from the horizontal plane on which the material can be heaped without collapsing [14]. A low repose angle is associated with a fine PSD, while a higher repose angle corresponds to a coarser PSD. The trends in cover percentage and deposition rate are shown in Figure 2.17

Factor	Low (-1)	Medium(0)	High (+1)
Layer Thickness	40 µm	—	80 µm
Recoating Speed	50 mm/s	—	150 mm/s
Recoater Material	Silicone	—	Tool Steel
Powder Quality	30°	40°	50°

Figure 2.16: Factor levels used in experimental design [60]

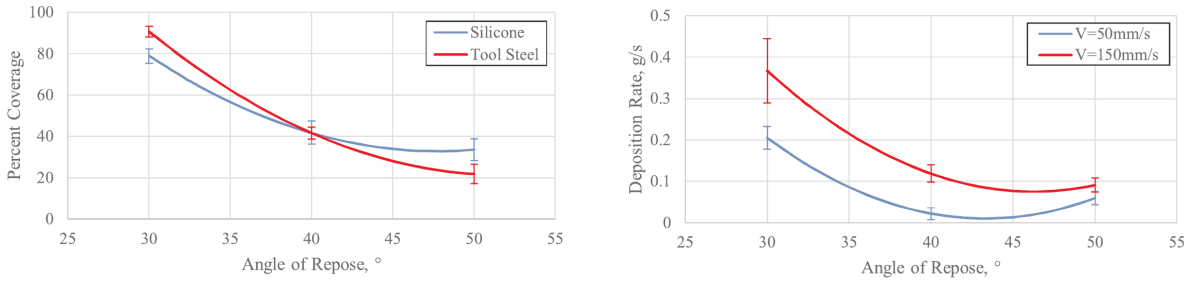

(a) Cover percentage results

(b) Deposition rate results

Figure 2.17: Results of parametric analysis on the effect of recoater arm type, recoating speed and PSD [60]

As can be seen, the recoater material has a notable influence on both the cover percentage and deposition rates. Variations of up to 15-20% in cover percentage can be found depending on the material used. It can also be noted that the influence that the recoater arm material has on cover percentage cannot be dissociated from powder characteristics. At lower repose angles (i.e. finer PSD), the steel recoater arm increases the cover percentage by 10% over the silicone recoater. However at higher repose angles (i.e. coarser PSD), this trend is reversed. While the recoater arm material clearly has an influence on coverage percentage, and thus print quality, Snow et al. [60] note that its effect is nearly five times less impactful than that of the powder quality itself. Improving the feedstock quality (by increasing flowability) is thus a more effective way of improving powder deposition. Nevertheless, the influence of the recoater arm should be considered when printing similar parts with various machines (as may be the case both in experimental research and production scenarios). Concerning the deposition rate, it is found that increasing the recoating speed is most effective at lower repose angles (i.e. finer PSD) powders. At 50°, multiplying the recoating speed by three only marginally improves the deposition rate.

Le et al. [44] perform further analysis on the areal surface roughness observed on stainless steel samples printed with different recoater blade materials and recoating speeds. Their experiments confirm that the surface Sa is influenced by both parameters, as well as that their influence is heavily interdependent. They find that while sharp metal blades provide the most uniform density along the recoating direction, rubber/silicone blades provide a more

consistent layer thickness and lower surface roughness. While excessive recoating speeds yield poor quality, too low speeds also tend to increase surface roughness. They find that, across all recoater arm materials, mid-range speeds yield the best results (10-80 mm/s for steel). The generally higher roughness resulting from the use of metal blades is theorized to result from a higher sensitivity to powder moisture content. Figure 2.18 depicts the results from their analysis.

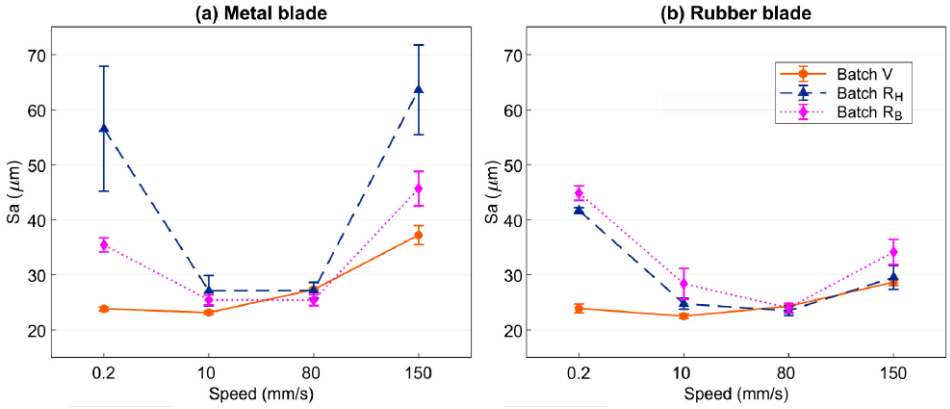

Figure 2.18: Surface roughness at varying recoater speeds and materials [44]

2.5.4 Build angle

The build angle θ represents the angle of a surface as measured from the horizontal build plate on which a part is constructed. Horizontal surfaces are parallel to the build plate and have a build angle of 0°, while vertical surfaces are perpendicular and have a build angle of 90° (as indicated in Figure 2.19). The build angle should not be confused with the orientation, with concerns the angle between a surface and the re-coating direction.

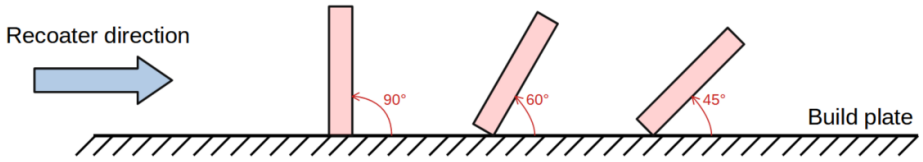

Figure 2.19: Build angle schematic

It is well established that the surface roughness is strongly correlated to the angle of the printed surface. As a surface transitions from horizontal upskin to horizontal downskin through a range of angles, the dominant source of surface roughness changes. A number of studies have performed experiments on the effect of angle on roughness, and though the general type of roughness associated with a certain angle seems to be quite consistent, varying results on the magnitude of roughness metrics as a function of build angle can be found across some studies.

Since the different sources of surface roughness all present some level of dependency on the build angle, a prediction of the dominant source for different angles can be made based on theory. In general, it is expected that horizontal upskin surfaces exhibit the lowest amount of surface roughness [51][63]. Since a horizontal surface is printed in one layer, it is not subject to the stairstep effect. Additionally, an upskin surface is not susceptible to dross or effects resulting from the removal of support structures. The roughness of these surfaces is typically a

result only of weld tracks [78], balling [35] and/or spatter [48]. As the build angle increases, the stairstep effect becomes more noticeable. The degree to which it causes additional roughness is not dependent only on the build angle, but also on parameters like the layer height (H) and overhang/offset (h) [63][80]. The stairstep effect can be expected to reduce again when surfaces near 90° inclination. At this stage roughness appears to be dominated by partially melted particles due to the surface being printed next to powder [51], as well as roughness resulting from the hatch distance (see [68] for a more in depth review). Overhanging or downskin surfaces are additionally susceptible to dross [81][19] and the effects of support structure removal, so they can generally be expected to have a higher surface roughness than upskin surfaces.

Chapter 3

Experimental Phase

The thesis presented here is largely composed of two phases. The first concerns the generation of experimental data to support the research, the second concerns the analysis of test results and study of correlations between the various observed characteristics. This chapter discusses the objectives, preparation and execution of the test phase. Note that actual results are presented and discussed in later chapters, the focus in this chapter is placed primarily on the methodology of the testing/machining itself. The test objectives link the test phase to the overall thesis goal, and are discussed in section 3.1.

The details of the test plan are then presented in section 3.3. Information on the design of the samples and the printing process is then given in section 3.4 and section 3.5 respectively. Finally, a number of post-processing steps are discussed in section 3.6.

3.1 Test Objectives

As mentioned in chapter 1, each research (sub-)question is related to a specific set of objectives. These objectives are defined such that, when completed, the (sub-)question can be answered. For each sub-question, the following objectives were defined:

SQ-1: What is the influence of varied build angle on the surface roughness of L-PBF flow channels?

This question addresses the need to understand how specific aspects of the printing process influence the surface roughness of internal flow channels. The following thesis objectives are related to this question:

a. Design and print test samples representative of small internal flow channels (see test plan for more details)

b. Determine the value of relevant surface roughness parameters for the various test samples

c. Assess the relation between surface roughness parameters and the build angle (plus any other printing parameters that were varied)

SQ-2: What is the influence of varied build angle on the friction factor of L-PBF flow channels?

This question addresses the need to understand how the friction factors of small L-PBF channels with high a relative roughness is dependent on aspects of the printing process, as well as how much it deviates from the traditional Moody charts approximation. The following thesis objectives are related to this question:

a. Manufacture/install test setup equipment for measuring pressure drop of flow tubes

b. Measure pressure drops for all samples at various flow conditions

SQ-3: How representative are open-contour samples of closed-contour prints?

This question addresses the need to scale the roughness verification process to that of full chambers/nozzles printed with internal flow channels. To avoid having to cut open a full print to verify the surface roughness, it is helpful to print open contour samples and compare the measured surface roughness with that of closed contour tubes. This will provide insight into whether those roughness measurements are representative of those inside a full print. The following thesis objectives are related to this question:

a. Print a set of open-contour samples with the same dimension/build angle as the closed contour samples

b. Determine the value of relevant surface roughness parameters for the open contour samples

c. Compare the roughness measurement of open and closed contour samples

SQ-4: How do the performed measurements and tests relate to the primary research question?

This question addresses the conclusions that can be drawn from data gathered with roughness measuring and flow testing. It essentially connects the answers to previous sub-questions to the primary research question. The following thesis objectives are related to this question:

a. Investigate relation of surface roughness metrics to friction factor

b. Investigate relation of build angle to friction factor

c. Investigate relation of relative roughness to measured roughness and friction factors

3.2 Test Matrix

Care must be taken to ensure that the defined test plan in fact generates the results required to answer each of these objectives, and conversely that every step undertaken indeed has a clear objective matched to it. This is done through the means of a test matrix, which can be used to verify which test phases contribute to which objective. The test matrix for this experimental thesis is shown in Table 3.1.

The experimental phase broadly consisted of three phases: manufacturing, flow testing, and microscope testing. Here, the flow testing was aimed at obtaining the desired flow performance data, while the main objective of the microscope testing was surface roughness and cross sectional area measurements. The microscope testing therefore consisted of three sub-items: Cross sectional area measurements, closed-contour [CC] surface roughness measurements, and open-contour [OC] measurements.

Table 3.1: Test Matrix

Test/Objective	Q1-a	Q1-b	Q1-c	Q2-a	Q2-b	Q3-a	Q3-b	Q3-c	Q4-a	Q4-b	Q4-c
Printing	x					x					
Flow testing				x	x				x	x	x
Cross sect. area measurement									x	x	x
CC SR measurements		x	x					x	x		x
OC SR measurements							x	x			

As can be seen, each objective is met by either one or a combination of tests. The details of these tests, as well as the required steps between each test, are discussed in section 3.3.

3.3 Test Plan

Table 3.2 provides an overview of all the steps involved in reaching the above discussed objectives. Broadly speaking, after the samples were printed, the test campaign consisted of a series of tests and machining processes. The purpose of each machining process was to prepare the samples for the next measurement. Each step is reviewed in more detail in subsequent sections.

Table 3.2: Test Plan Elements

ID	**Step**	**Type**	**Method**	**Responsible**
P	Printing	Manufacturing	L-PBF	3DSystems
M1	Tube separating	Machining	Water jet cutting	DEMO
M2	Pressure port holes	Machining	Electric Discharge Machining	DEMO
M3	Welding clamp	Machining	Milling	A. Thiam (@3ME)
M4	Adapter Welding	Machining	Arc Welding	3ME
A	Setup assembly	Assembly	-	A. Thiam (@HSL)
T1	Flow testing	Testing	-	A. Thiam (@HSL)
M5	Sample splitting	Machining	Electric Discharge Machining	DEMO
T2	Area characterization	Testing	Keyence Microscope	DASML
T3, T4	SR characterization	Testing	Keyence Microscope	DASML

3.3.1 Involved Parties

A number of external parties were involved in some of the manufacturing/testing steps. Their involvement in the project is described here:

- **3DSystems**: 3DSystems is the 3D printing company that provided input on sample design for printability, and subsequently manufactured and heat treated the channels. The company allocated a budget to funding research on the topic of surface roughness, and their willingness to fund these samples was the main driver for their selection.
- **DEMO**: Dienst Elektromechanische en Mechanische Ontwikkelingen [DEMO] is a manufacturing lab located on the TU Delft campus. Their water jet cutting and electric

discharge machining [EDM] capabilities were required for the separating and sectioning of the samples in between test phases. Manufacturing drawings and instructions were provided to machinists at DEMO, and the machining processes were supervised where necessary to provide further input.

- **3ME**: A 3-axis mill at the workshop of the faculty of Mechanical, Maritime and Materials Engineering was used for manufacturing the welding clamp, as well as the cutting and polishing of sample extension tubes. The welding itself was performed by workshop staff, once again supervised to provide inputs and instructions.
- **DASML**: Microscope measurements were performed using the equipment of the physics lab at Delft Aerospace Structures and Materials Lab [DASML].
- **HSL/LSL**: Facilities at the High Speed Lab [HSL] of the Aerospace Engineering faculty were used to perform the flow testing. The experimental setup was assembled near a supply of clean, dry, pressurized air. Equipment such as flow controller and National Instruments readout modules were borrowed from both HSL and LSL (low speed lab) for data readout.

3.4 Sample Design

This section addresses the sample design, functional requirements for the samples, and motivations for selection of sizes/materials based on literature and discussion with 3DSystems.

3.4.1 General Design Approach

Part design is a process often driven by a combination of the need to satisfy functional requirements of the end product, and the need to be compatible with any limitations imposed by the employed manufacturing methods. Thanks to the design freedom provided by the nature of additive manufacturing, this latter point represents a much less significant constraint during this process. The limitations imposed by the printing machine largely consist of the following:

- Build volume is limited in width, length and height
- *Most* surfaces cannot feature overhangs of 45° or less without the use of supports (i.e. not possible for internal geometries where no supports can reach). Small surfaces with little material above them are the exception here (edges/lips of 6-8 mm, requirement obtained from manufacturer)

Other limitations may arise due to part specific properties (e.g. risk of bending with long and slender components), but most design considerations are made with these two rules in mind. As discussed in section 3.1 and section 3.3, the sample then needed to provide two primary functions: a channel for the measurement of pressure drop of an air flow, and both internal and external surfaces for the measurement of surface roughness. While the purpose of this thesis is to assess surface roughness properties of micro-channels, there are certain risks associated with the printing of small internal geometries that had to be considered. As shown by Gradl and Protz [34], small channels run the risk of being clogged with powder. In addition, the smaller a geometry is, the larger the relative deviation from the design cross section will be.

Next to geometry, channel length also presents a risk, especially in cases where samples are printed under angles. Long and slender items run the risk of deforming under heat treatment.

Furthermore, incorrectly calibrated print settings and recoater blade issues can lead to witness lines, also referred to as recoater-hopping and/or recoater-streaking [50]. These can introduce large surface anomalies that may throw off a pressure drop measurement. To minimize the risk of these issues affecting too many samples, the geometry was kept at 2x2 mm internal geometry, and 150 mm sampling length.

Further discussions on the dimensions were held in consultation with 3DSystems regarding the allowable print volumes (i.e. volume of solidified, non-reusable powder) and dimensional constraints on printer height. These dimensional choices were also made in view of budgetary limitations imposed by 3DSystems, as the printing was performed as part of a sponsorship. The design was thus also driven by the need to deliver testable samples with a minimized need for re-prints due to defects/optimizations.

3.4.2 Sample Requirements

As discussed in section 3.1, the test matrix serves the purpose of aligning the testing process with the thesis objectives. It ensures on one side that every step of the test campaign actually contributes to an objective, and conversely that every objective is met with a test result. The next step is to ensure that the sample design and production/post process enable each of the tests to be carried out. This was done by defining a list of requirements, relevant either to the design of the samples or to a particular process performed on the sample. The latter is crucial because, as shown in the test plan in section 3.3, a variety of third parties are involved in both the printing and post processing of the samples. The outcome of each of these externalized processes can greatly influence the accuracy of the results obtained during testing. As such, requirements on these processes were included in the overview provided below. Requirements were subdivided into design requirements (D), printing requirements (P), and machining requirements (M).

Table 3.3: Sample design & process requirements

ID	Requirement	Relevant objective (if applicable)
Req-S-D-001	The samples shall provide closed channels with 150 mm straight channel sampling length	SQ1-a/c; SQ-2b; SQ-3c; SQ-4a/b/c
Req-S-D-002	Sample cross section shall be square	
Req-S-D-003	Sample wall thickness shall withstand a MEOP of 20 bar	
Req-S-D-004	Each channel shall contain pressure ports up and downstream of the measurement section	SQ-2a; SQ-2b
Req-S-D-005	Internal cross section of closed channels shall be large enough to prevent clogging with a high confidence level	
Req-S-D-006	Sample in/outlets shall provide a circular cross section for welding to 6 mm Swagelok tubing	
Req-S-D-007	The samples shall provide open contour witness surfaces	SQ-3a/b/c
Req-S-D-008	Open contour witness channels shall have the same dimensions as the closed contour channels	SQ-3a/b/c
Req-S-D-009	Channels shall be distanced from eachother sufficiently to allow for separation by water jet cutting	
Req-S-P-001	If the printing requires support structures they shall not connect to surfaces intended for measurement	SQ-3a/b/c
Req-S-P-002	The sample shall be printed at build angles 90°, 60° and 45°, measured from horizontal	SQ-4b
Req-S-P-003	Printed samples shall be heat-treated for stress-relief	
Req-S-M-001	Pressure ports shall minimize disturbance of flow uniformity in the channel	
Req-S-M-002	Any manufacturing/machining carried out on the sample after printing and before flow testing, shall be selected and performed to have minimal impact on flow uniformity	

3.4.3 Structural integrity

The sample flow testing entailed subjecting the channels to pressurized flow. To ensure the samples could withstand this testing, an assessment of the allowable internal pressure was conducted. Due to the square cross-sectional nature of the channels, hoop stresses can not be calculated as straightforwardly as for circular cross sections.

In light of this complexity, a simplifying assumption was made. It was hypothesized that the walls would elongate to a circular cross-section before reaching the bursting point. This assumption formed the basis for calculating the maximum hoop stress. To account for this assumption, a safety factor of two over the yield strength was applied. This is in addition of the standard safety factor of two applied for safety margins.

Deriving an equivalent circular cross-sectional diameter from the perimeter facilitated the calculations. This allowed the utilization of Equation 3.1 to derive the maximum operating pressure:

$$P_{max} = \frac{2t\sigma_y}{d_{eq}SF_1SF_2} \tag{3.1}$$

Here, σ_y is the yield stress, d_{eq} is the equivalent diameter of a round tube with perimeter equal to that of the square channel, and SF are safety factors. The yield stress of heat treated Ni718 printed in the DMP Flex 350 machine was used [5]. As the yield strength depends on the direction of printing, the lowest possible value of 1160 MPa was used. The design thickness of 1.5 mm was used, and the equivalent diameter was calculated from external perimeter to be

conservative (d_{eq} = 6.366 mm).

The resulting maximum allowable operating pressure stood at 136 MPa, which provides ample margin over the expected operating pressure of 5-10 bar. It should be noted that the weld seams are likely to fail before the channel would reach its bursting point. The selected wall thickness of 1.5 mm was therefore considered an adequate design choice.

It's important to note that weld strength relies significantly on the quality of the weld, and analytical assessment might not accurately predict its performance. Considering this, low-pressure leak tests were incorporated into the test procedure. This measure aimed to prevent inadvertent leakage or burst of the welds at higher pressures, ensuring a robust and controlled testing environment.

3.4.4 Internal Roughness Witness Specimen

In the case of this particular study, channels are printed for the purpose of analyzing their internal roughness. As a result, they are made to be destructively tested and do not serve any further purpose beyond this study. In many cases however, printed parts cannot be cut open for investigation as they have to remain functional. If these parts contain internal geometries whose surface roughness is relevant to part performance (e.g. internal flow channels), some form of external validation of achieved roughness levels may be required. An example might be the cooling channels of a combustion chamber that need to be manufactured within a specific range of surface roughnesses. Acceptance testing cannot involve destructive processes, so an external method for the verification of requirements compliance is necessary. In the context of additive manufacturing, it is common to print witness specimens. These are specimens that are printed alongside the main part, meaning they are printed using the same powder, in the same machine, using the same process parameters. Material property requirements of the main part are then verified through the assumption of similarity with the witness specimen.

However, there is not necessarily a one-to-one comparison between open and closed contour surfaces. The sintering/melting process can for example send molten droplets flying towards surrounding surfaces. The absence of one of the four surfaces on an open-contour channel might change how this affects surface roughness.

As a result, it is of interest to investigate how closely the surface roughness of open channels compare to that of closed channels. Confirming the validity of this similarity assumption for small channels would allow for easy verification of surface roughness inside of a closed contour channel by printing open-contour specimens.

In order to verify this, the three channels contained within each sample were accompanied by two open contour channels (to account for both up and downskin surfaces). these were intended only for microscope testing, and their surface roughness was compared to that of the internal surfaces of the channels they were printed with.

3.4.5 Sample Design Overview

The requirements discussed in subsection 3.4.2 were used as a basis for designing the sample, which was then refined through an iterative process involving discussions with 3DSystems. Each sample was designed to contain 3 internal flow channels, and two external witness

specimen channels. The wall thickness of the internal flow channels was kept at 1.5 mm to provide ample margin on pressure resistance (see Appendix C) and potential defects/influence introduced by the thin walled nature. Channels within one sample were connected to each other through a thin plate, distanced from each other sufficiently to allow easy separation using water jet cutting. Note that this connecting plate was added by 3DSystems before printing, and is not shown in the technical drawings. Pressure taps were not included in the print, as the achievable dimensional accuracy would require post processing anyways to reach a good tolerance on diameter. Instead, electric discharge machining [EDM] was used at a later stage to introduce these taps.

Figure 3.1 shows a cross sectional view of the sample, highlighting both open and closed contour sample surfaces. A full technical drawing of the sample can be found in Appendix B.

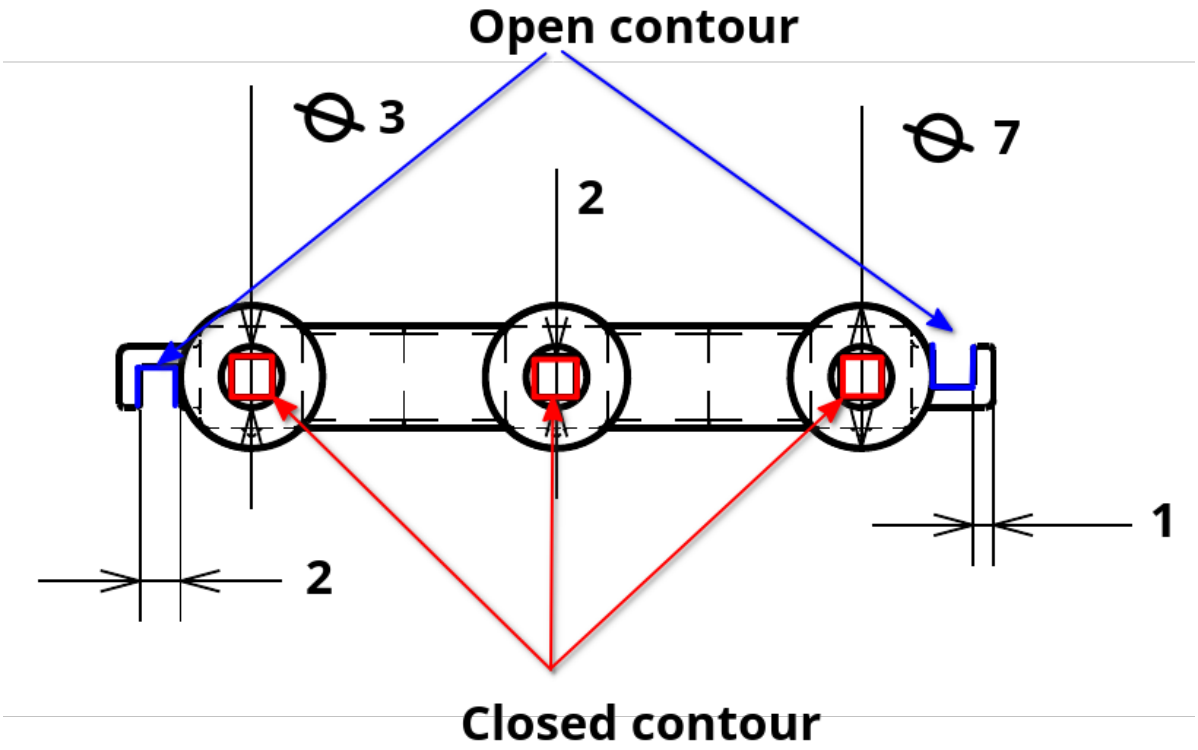

Figure 3.1: Layout of open and closed contour surfaces (cross section)

A square cross section was chosen over round sections for the internal channels. This is primarily because in the context of heat exchanging channels, a flat contact area between the coolant and heated surface provides more cooling efficiency. The printing process itself cannot effectively print sharp angles, so corners were given a 0.3 mm fillet (as recommended by manufacturer).

3.5 Printing [P]

This section discusses all aspects related to the printer model and processing parameters used, material selection, as well as printing outcome and identified defects.

3.5.1 Material Selection

As discussed in section 3.1, the purpose of the study is to investigate the effect of the build angle on certain performance parameters of internal flow channels. While the material should be selected to be representative of potential final application, it is not the subject of the study itself. Results, in absolute terms, are of course relevant to the printed materials, but it is ultimately the trends in performance parameters with respect to the build angle that are of interest. As a result of this, and taking into consideration what powders were made available by 3DSystems for the project, the selection was primarily based on final applicability to heat exchanging internal flow channels.

Available materials for printing with 3DSystems were the following:

- LaserForm 316L
- LaserForm Ni718
- LaserForm Grade 23 Titanium (Ti6Al4V)

In the context of heat exchanging channels in high pressure environments (such as combustion chamber cooling channels), strength and heat resistance are arguably the most important material characteristics to consider. Resistance to highly oxidizing environments may also be of interest, in cases where an oxidizer is used as a coolant. Finally, high thermal conductivity is of interest as it promotes the transfer of heat into the coolant fluid. Table 3.4 lists out these characteristics for the LaserForm powders proposed by 3DSystems:

Table 3.4: LaserForm material properties (for DMP Flex 350)

Property	Ti6Al4V [7]	316L [5]	Ni718 [6]	**Unit**
Ultimate tensile strength	1060	660	1400 (heat treated)	MPa
Melting range	1604 - 1660	1370-1400	1260-1335	°C
Thermal conductivity (at 20 °C)	5.9	15	11.4	W/m.K

Note that these properties do not depend only on the feed stock, but also on the printer used. Properties shown in Table 3.4 correspond to those obtained using the printer used for these samples. Printer type and settings are further discussed in subsection 3.5.2. As can be seen, while Ti6Al4V has a relatively high ultimate strength and melting temperatures, it's thermal conductivity is low, making it a poor choice when the end application concerns heat exchange. 316L on the other hand provides the highest conductivity of all three, but is significantly weaker. Heat treated Ni718 provides the highest strength of the three materials, melting temperatures only slightly below that of 316L, and relatively high thermal conductivity. Ni718 also offers high corrosion resistance [6]. As such, the samples were printed using LaserForm Ni718.

3.5.2 Machine Characteristics & Print Settings

In total, two batches of three samples were printed. For each batch, samples were printed at 45°, 60° and 90° for a total of 9 channels per batch. Both batches were printed using the DMP Flex 350. DMP stands for Direct Metal Printing, and is a trademark printing technique owned by 3DSystems (see subsection 2.1.1). It is a specific implementation of L-PBF. A primary characteristic of DMP is the fact the it sinters (i.e. only partially melts) the powder, as opposed to fully melting it. Since the 3D printing was done as part of a sponsorship of the thesis by 3DSystems, there was no particular tradeoff on the advantages/disadvantages of the available

printing machines. The machine selection was driven primarily by availability and cost, and was done by 3DSystems.

The second batch was mainly printed as a result of significant printing defects on the first batch (notable on the 60° samples). While not problematic for surface roughness measurements, they were deemed too large to provide reliable flow testing results (see subsection 3.5.3). Unfortunately, 3DSystems was strained in resources, and as a result had to print the second batch in a different facility. While the printer properties were largely the same, one notable difference is the use of a carbon blade recoater (as opposed to a soft blade recoater on the first machine). The use of this recoater type unfortunately introduced further defects in the sample. As is more extensively discussed in subsection 3.5.3, this goes to show that even for simple geometries it is difficult to get successful prints on the first iteration. New parts often have to go through a number of iterations before consistent results are obtained. This can be due to several factors, including the complexity of the process and the need to optimize various parameters such as layer thickness, printing speed and laser settings. This further highlights the utility of reliable witness specimens for internal geometries, essentially allowing the non-destructive verification of surface quality.

Because the samples were printed in two different facilities, the stress-relieving heat treatment was also different. Table 3.5 resumes the properties of the printing/heat-treatment used for each batch. The addition of microshot peening on the second batch is discussed in subsection 3.5.3.

Table 3.5: Print Specifications

Specifications	**Batch 1**	**Batch 2**
Printer	DPM Flex 350	DMP Flex 350
Laser Type	Fiber laser	Fiber laser
Laser Power	500 W	500 W
Laser Wavelength	1070 nm	1070 nm
Middle/Upfacing Energy Density	62 J/ mm3	62 J/ mm3
Downfacing (from 25°) Energy Density	30 J/ mm3	30 J/ mm3
Build Volume	275 x 275 x 420 mm	275 x 275 x 420 mm
Layer thickness	30 μm	30 μm
Deposition Method	Carbon blade recoater	Soft blade recoater
Process chamber gas	Argon	Argon
Heat treatment	1 hr @ 980°C	4 hr @ 720°C
Microshot peening	No	Yes

The samples were printed using a layer thickness of 30 μm, primarily based on recommendations from 3DSystems. Furthermore, the 3D print engineer recommended adding a 0.14 mm offset on the internal dimensions of the channels. Based on his experience, this was necessary to get a result as close as possible to the 2 mm design geometry. Support structures were then added for the inclined samples. The 45°, 60° and 90° samples were all printed in the same volume using the configuration shown in Figure 3.2:

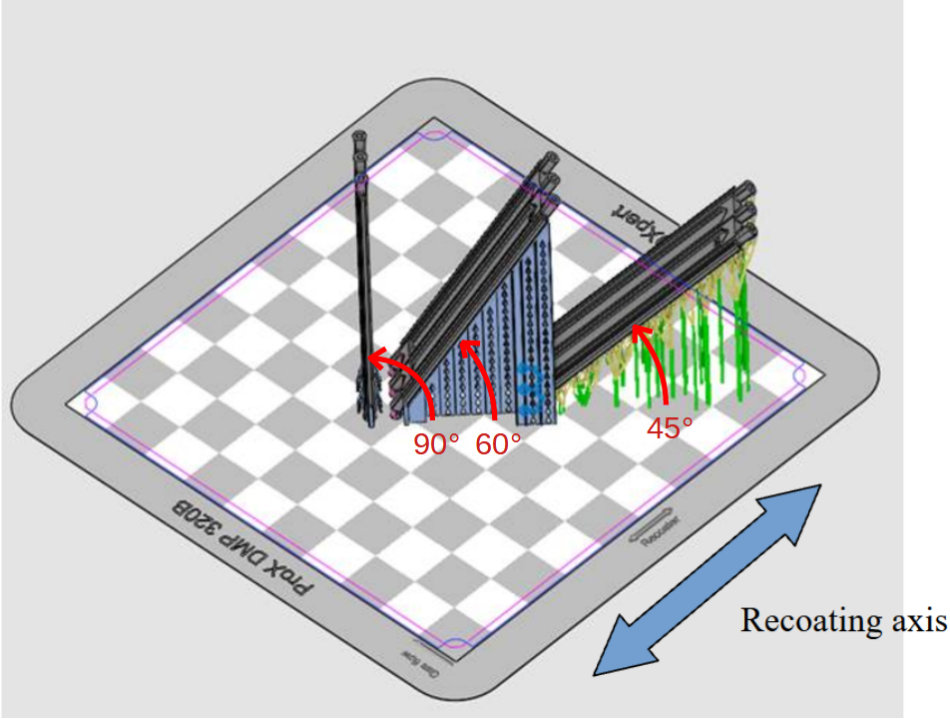

Figure 3.2: Print Configuration

As can be seen, support structures were required for the inclined samples. Where possible, anchoring the support material on the outer contour witness surfaces was avoided.

3.5.3 Print Defects & Sample Selection

The additive manufacturing of metals remains prone to a very large variety of defects [50], a number of which were discussed in section 2.5. The printing of these samples was no exception, and resulted in a number of samples not being fit for flow testing. The defects identified on samples of both batches are discussed in this section. A comprehensive overview of which sample was printed with what printer/settings, presented what defects, and was used for what testing, can be found in Appendix D.

The first batch of samples had to be printed in two iterations. Due to issues with the printer itself, the first print attempt was stopped halfway, resulting in only the most inclined sample of 45° (as a result of its lower build height) being completed. The second attempt of this print unfortunately created defects on the 60° sample which made it ill-suited for flow testing. Near the ending of exit of the 60° sample, the printer got off-set, causing a significant deformation in the channel geometry as shown in Figure 3.3. In order to study the variation of friction factor with build angle as best as possible, it was preferable to have at least one flow-testable sample from each build angle. 3DSystems proposed to repeat the entire print, and it was decided to follow through with this.

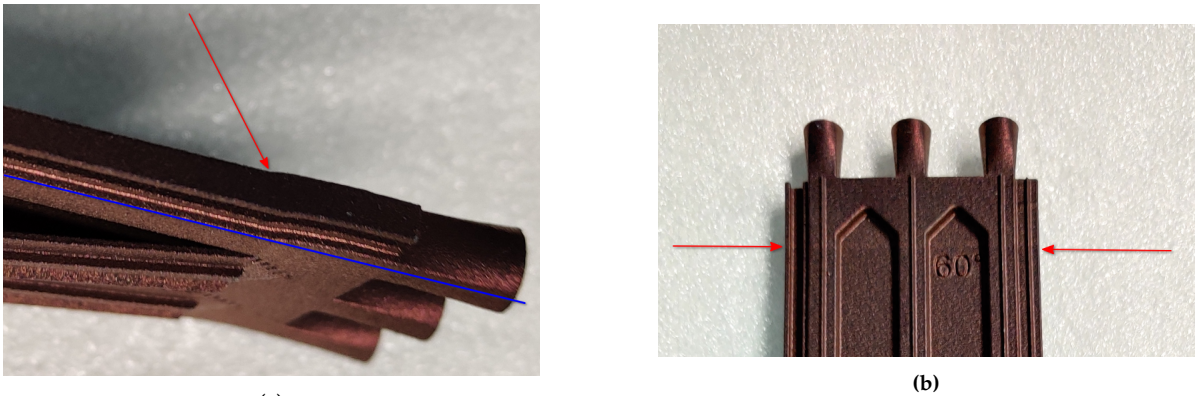

(a) (b)

Figure 3.3: Batch 1, 60° sample, kinked channels

The second batch was printed in the same printer, but using a different recoater blade material. Where the first print utilized a carbon brush, the second printer used a soft blade recoater. As mentioned in section 2.5, the use of a different recoater mechanism can have an influence on the surface roughness, and should ideally be kept unchanged for samples to be comparable. Unfortunately this was not possible due to 3DSystems' resources being stretched. The consequence of this however is that the second batch suffered from another defect. Samples presented witness lines, which are ridges in the print surface resulting from the interaction between the powder and recoater blade. Soft blade recoaters, according to 3DSystems, are more susceptible to this effect, and in particular with inconel.

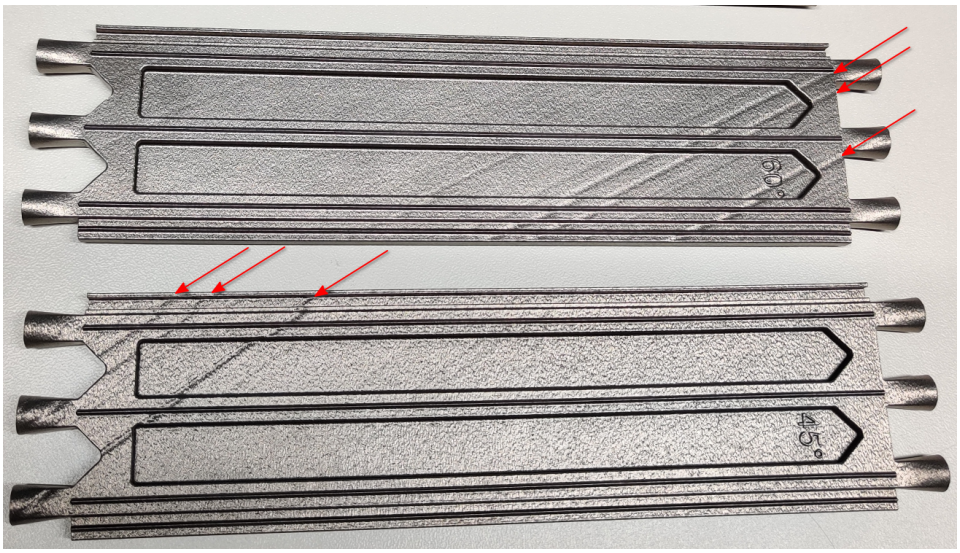

Figure 3.4: Batch 2, 45° & 60°, witness lines

The channels that were affected by these defects were removed from the selection for flow testing. For batch 2 this means only the 90° samples were kept, as all channels on the 45° and 60° samples were affected. Since the purpose is to characterize the effect of surface roughness of certain parameters of channel performance, it was chosen not to introduce any other potential sources of pressure loss. All samples are of course suitable for microscope testing, where care can be taken to avoid taking into account features originating from defects when assessing surface roughness. This resulted in lower sampling areas on low build angles, as shown and discussed in subsection 4.2.2. As will be discussed in section 3.6, one further selection for flow

testing was made as a result of curvature introduced after the release of internal stresses.

Microshot Peening

A final difference worth noting between the two batches is the surface colour. This is due to the fact that the post-process engineer in charge of the second batch used micro-shot peening to smoothen the external surface. This is a common process for final parts, and tends to be avoided only in a minority of cases such as when studying the surface roughness is the purpose of the print. Upon investigation it appeared that this was an internal misunderstanding within 3DSystems. Although the channels were taped shut, it does mean that the external witness channels cannot be directly compared between the two batches.

3.6 Post processing [M]

Each of the planned measurements requires some interfacing between the samples and the measurement equipment. In the case of flow testing, channels need to be separated from each-other, and attached to both fluid delivery components and sensors. In the case of microscope testing, samples need to be prepared so they have accessible dimensions, and the surfaces of interest are exposed in a way that they can be measured. The post-processing steps shown in the overview below were chosen to satisfy these needs, and are discussed in more detail in this section.

Table 3.6: Overview of post processing steps

ID	Step	Process type	Performed by
M1	Tube separating	Water jet cutting	DEMO
M2	Pressure port machining	Electric Discharge Machining	DEMO
M3	Manufacture welding clamp	3-axis Milling	A. Thiam
M4	Adapter welding	Arc Welding	3ME
M5	Sample splitting	Electric Discharge Machining	DEMO

3.6.1 Flow test preparation

The flow testing requires each channel to be connected to fluidic connectors, both upstream and downstream. In addition, temperature and pressure are to be measured. In order to facilitate the manipulation of fluidic connectors, channels that were printed as part of one sample were first separated using water jet cutting (M1). Next, Electric Discharge Machining [EDM] was used to create a set of holes for pressure measurements (M2). While the temperature can be measured upstream of the sample, the measurement length of the differential pressure was chosen to be within the channel length itself. This avoids having to attribute a certain portion of the measured pressure drop to the flow connectors and transition over the weld seam. Figure 3.9 shows the result of these two processes (note that there are also smaller holes present for the temperature measurement, these were made as a precaution but later plugged and replaced with upstream measurement to avoid flow disturbance):

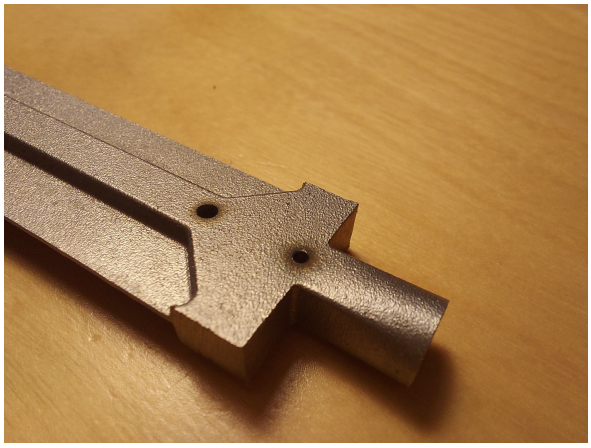

Figure 3.5: sample w/ holes, before welding

The separating of the channels resulted in the release of internal stresses that the heat treatment was not able to fully alleviate. As a result, a few channels came out of process M1 with a significant curvature. This was most prominent on the outer channels, which had a tendency to bend in-plane away from the center-line (as shown in Figure 3.6). These are the last channels that were eliminated for flow testing. Compounding all of the print/manufacturing defects resulted in a sub-selection of 5 fully nominal channels for flow testing, while the totality of both sample sets were used for microscope testing. A full overview of which channels were further prepared for flow testing can be found in section D.2.

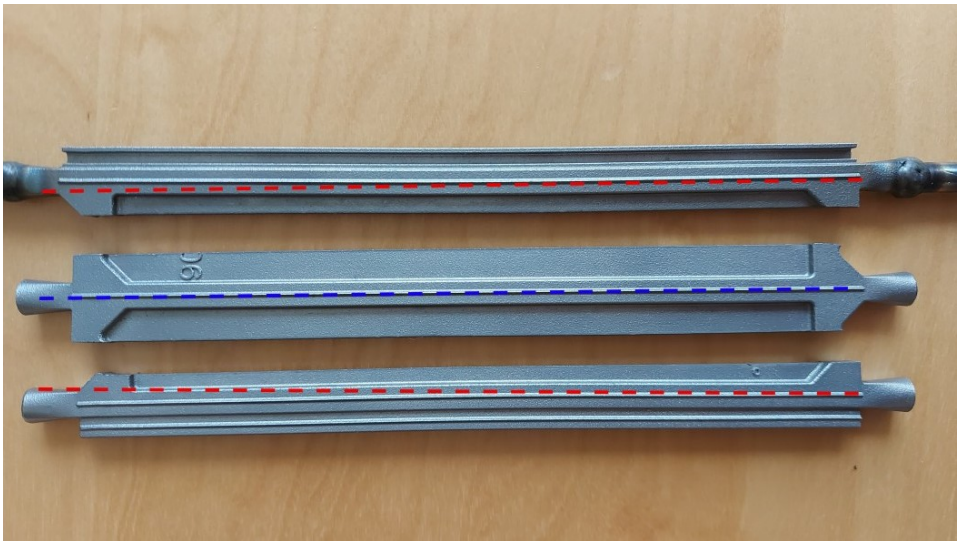

Figure 3.6: Curvature on outer channel samples

After completion of the M1 and M2 processes, an aluminium alignment jig was machined using Aluminium stock and a three axis mill (see Appendix C for drawing). It was then used to weld short sections of 6 mm Swagelok tubing with the same inner diameter as the round sample exits (see Figure 3.7). The primary reason an alignment jig was necessary is because the internal alignment of the channel with the Swagelok tubing cannot be verified during the welding process. The jig was designed to have two alignment channels and an open space for welding access. Alignment channel heights were sized such that internal diameters of the sample inlet and Swagelok tube transitioned smoothly. The welding process was done such

that there would not be a full through-weld, which could potentially disturb the flow right before the first pressure measurement.

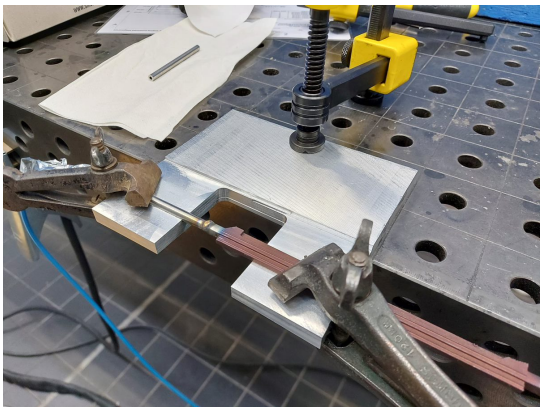

(a) Welded sample in clamp

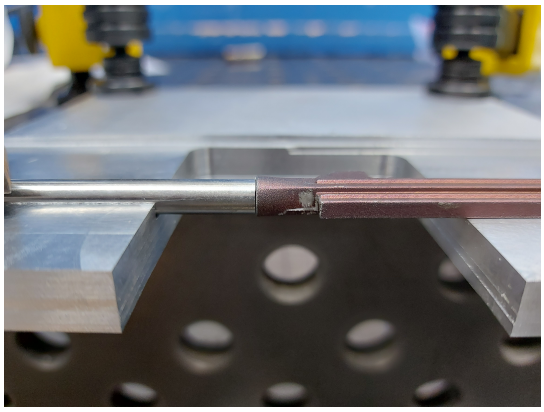

(b) Sample aligned with Swagelok 6 mm tube

Figure 3.7: Sample interface welding

Finally, 6 mm nuts and ferrules were attached to the welded extension tubes, and small pressure tap tubes were inserted in the pressure measurement holes and epoxied. At this point, the samples were ready to be integrated into a flow test setup:

Figure 3.8: Samples with compression fittings attached

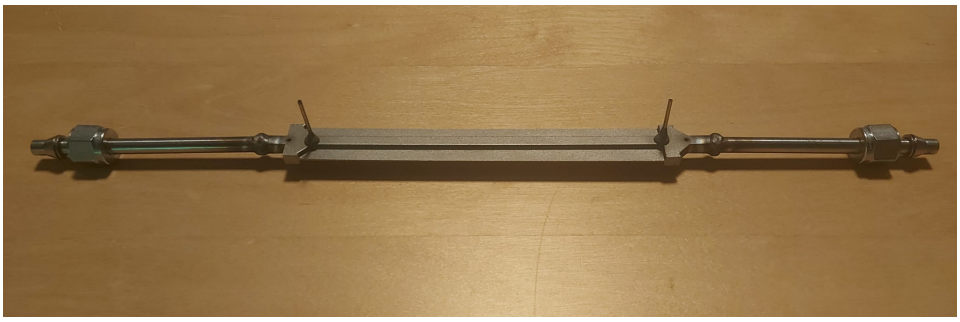

Figure 3.9: Sample ready for flow testing

3.7 Flow Testing [T1]

This section discusses all steps undertaken to perform the flow testing on the samples. Note that results are left out and discussed in more detail in chapter 4.

3.7.1 Measurement Strategy

Pressure measurements

As discussed in section 3.1, the influence of the build angle on micro-channel friction factor was assessed using measurements of pressure drops over the samples. The samples analyzed in the scope of this thesis are flow tested using air, primarily as a result of allocated budget and available facilities. Pressurized, clean water testing facilities are more complex (requiring pumps or upstream gas pressurization equipment), while air testing can be performed directly off of pressurized bottles of clean air using a pressure regulator to control inlet pressures. The main limitation this introduces is that air flow rather quickly reaches high Mach numbers. Reynolds numbers therefore had to be kept lower than a liquid test fluid might have allowed, resulting in a much lower pressure drop, and conversely a higher requirement on the accuracy of the pressure sensors.

To avoid compounding the error margin of two absolute sensors (e.g. one upstream and one downstream measurement), it was decided to use one absolute and one differential sensor. The differential pressure sensor can be rated to a much lower measurement range as the expected pressure drop is significantly lower than the actual fluid pressure. The absolute sensor is then placed upstream to ensure the true fluid pressure is also known. This information is mainly used for deriving fluid density and viscosity.

For measuring the pressure drop, a unidirectional differential sensor with an accuracy of +/- 0.08% was selected. The sensor had a total measurement range of 7 bar, and an output signal of 0-10 Vdc. G 1/4" Female fittings were chosen for both sides to interface with Swagelok compression fittings (using a male-male converter from BSP thread to Swagelok metric thread). While higher sensor accuracies were available, they came at a significantly increased cost. A brief investigation of the maximum expected measurement error was therefore done using this accuracy. Sensor accuracy is expressed as a percentage of its full measurement scale. With a 7 bar differential sensor, a maximum deviation from true value of 0.0056 bar was expected. For an expected friction factor of approximately 0.1 (end of Moody applicability range), flow testing at an absolute inlet pressure of 5 bar, this would result in a pressure drop of 0.57 bar. This would result in a measurement error of 1%, which was deemed acceptable.

Temperature measurements

The temperature measurement is mainly required to know what viscosity to assume when interpreting the measured pressure drops. The expected temperatures are all within ambient ranges, so from a flow compatibility point of view there were no particular requirements. That being said, it was important to ensure the thermocouple measured the flow temperature (i.e. not wall temperature through contact). Furthermore, the thermocouples should not be disturbing the flow nearby the channel entry. It was opted to make use of K-type probe sensors, inserted into the flow using bored-through Swagelok connectors, and sealed using compression fittings. The thermocouple probe was inserted such that it did not protrude into the circulating flow, but instead measured temperature in the stagnant part of the t-piece it was connected to.

Flow rate measurements

Because the flow rate was directly addressed using the flow controller, no external equipment was required for measuring it. The flow controller allowed both the addressing of a control value and readout of the true flow rate. The Bronkhorst EL-FLOW series F-202AV/F-212AV with a limit flow rate of 85 ln/min was used.

3.7.2 Fluidic Setup

Flow testing was executed in the High-Speed Lab at the Aerospace Faculty, as delineated in the previously established test plan. The experimental setup was strategically placed next to the Hypersonic Test Facility Delft (HTFD), enabling a steady provision of clean, filtered air supplied by high-pressure bottles, as well as power supply for sensors, read-out equipment, and the flow controller.

The core components of the setup comprised a flow controller, the sample under test, pressure and temperature sensors, and an exit valve. The latter ensured safe depressurization during leak testing procedures, as the system needed to be closed to allow leaks to be detected. Pressure supply was controlled by setting the outlet pressure of the compressed gas regulator connected to the supply bottle. Outlet pressure was reduced to ambient pressure in between tests to swap samples without having to close/re-open the gas bottle. Figure 3.10 represents a Piping and Instrumentation Diagram (P&ID) of the setup:

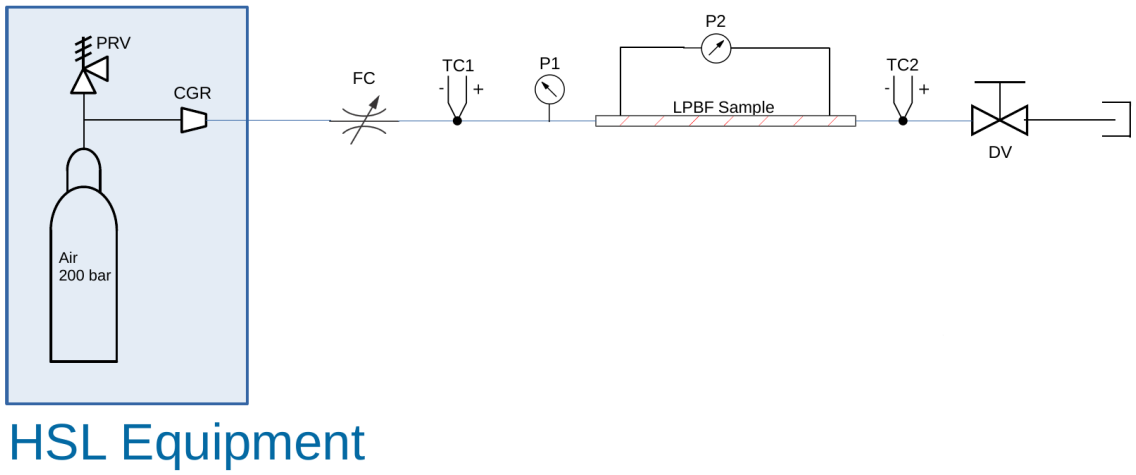

Figure 3.10: P&ID diagram of setup

The fully assembled set-up is shown in Figure 3.11.

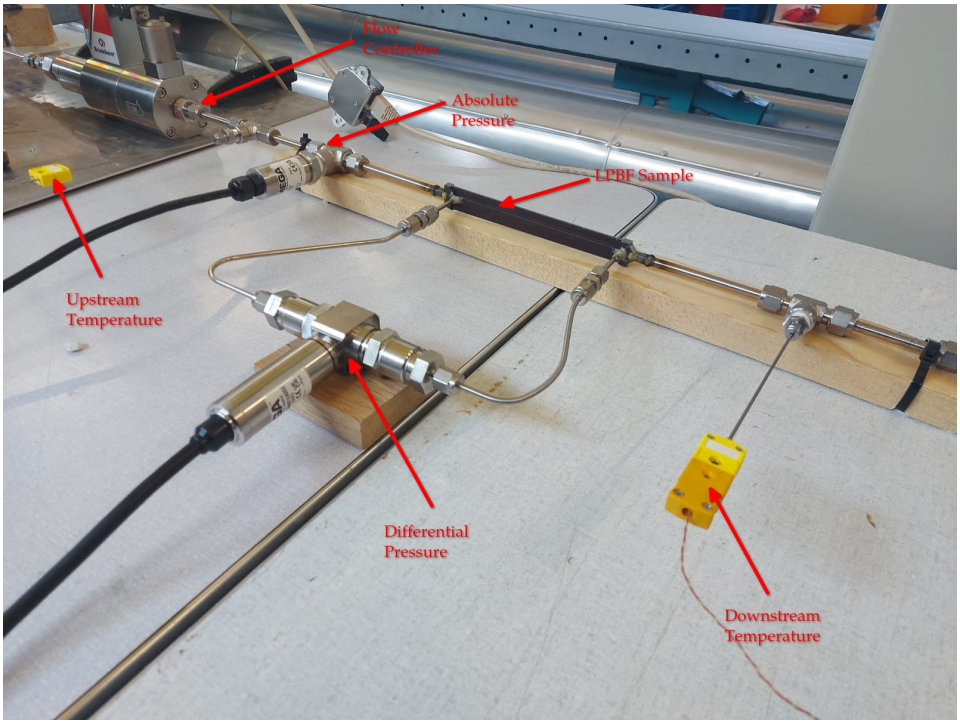

Figure 3.11: Test setup

Attention was directed towards ensuring all fluidic connections were leak-proof. A combination of Swagelok compression fittings, National Pipe Thread (NPT) fittings, gaskets and where necessary, epoxy and teflon tape, was used. The 1/2" parallel BSP threads to the flow controller were sealed using copper gaskets, while the 3/4" fittings to the differential sensor were sealed using steel+rubber gaskets. Teflon tape was only applied on the NPT fitting of the absolute pressure sensor. All other connections were sealed using compression fittings. These were installed using Swagelok guidelines, where 1 1/4 or 3/4 turns above hand tight were used to install the ferrules on 1/2" and 1/8" tubing respectively. Care was taken to install the ferrules on the thermocouples such that the probe tip would not protrude into the flow path.

To provide stability and prevent risk of damage/injury in the case any connection was improperly installed, the setup was anchored to the worktable using a durable metal plate, clamps, and tie-downs. This approach was checked with on-site safety officers, and ensured a safe and efficient workflow.

3.7.3 Leak Testing

Leak testing constituted a important component of the experiment for several reasons. From a safety aspects, low pressure leaks can result in dangerous situations when system pressure is further increased. From a data acquisition perspective, leaks can throw off pressure measurements and result in inaccurate interpretations of channel performance characteristics. This is particularly important when leakages occur within the measurement span of the differential pressure sensor.

To facilitate this, a hand-actuated valve was integrated into the setup, enabling both pressurization and safe depressurization of the entire system. Subsequently, gas leak detection spray was applied while the system was pressurized to approximately 3 bar in order to localize

any potential leaks. The fixed components of the setup underwent a single leak test. sample upstream and downstream connections and the two differential sensor pressure ports were leak tested after every sample swap.

3.7.4 Data Acquisition

Data acquisition during the flow testing was performed using National Instruments [NI] LabView, visual programming language developed by National Instruments for real-time sensor/data readout and actuator control. The software was configured to read out data from all sensors at a frequency of 10 Hz. Each sensor was connected to the NI module required for readout, and external power supply was provided where required. An overview of how the controller/sensors were set up is shown in Table 3.7.

Note that the flow controller was both controller and read out through different software. The communication to the computer was set up using FlowDDE software, and an RJ50 cable. Power was supplied through an external power supply. The flow rate was then controlled/measured using FlowView, an interactive UI developed by Bronkhorst (manufacturer).

Table 3.7: Component control/readout details

Component	Use	External power	NI Module	Readout	Control/Readout
P1	Upstream pressure	10Vdc (through NI module)	NI 9237	0-100 mVdc	NI LabView
P2	Differential pressure	24Vdc	NI 9215	0-10 Vdc	NI LabView
T1	Upstream temperature	-	NI 9213	mA	NI LabView
T2	Downstream temperature	-	NI 9213	mA	NI LabView
FC	Flow controller	Bronkhorst power supply	-	-	FlowView/ FlowDDE

Sensors were calibrated inside LabView according to the datasheets provided by manufacturers. Thermocouples were configured directly as K-type sensors. For the pressure sensors, the data provided by manufacturers was used to generate calibration curves, which were then applied inside LabView. Data shown in Table 3.8 was used to generate the calibration curves shown in Figure 3.12. All measurements were performed using a 10s averaging process to counter the effects of possible fluctuations.

Table 3.8: Calibration Data

Absolute [bar]	Output [mV/V]	Differential [bar]	Output [V]
0	0.0077	0	-0.003
150	4.9907	3.5	5.006
300	9.99971	7	10.007
150	4.9903	3.5	5.009
0	0.0076	0	-0.002

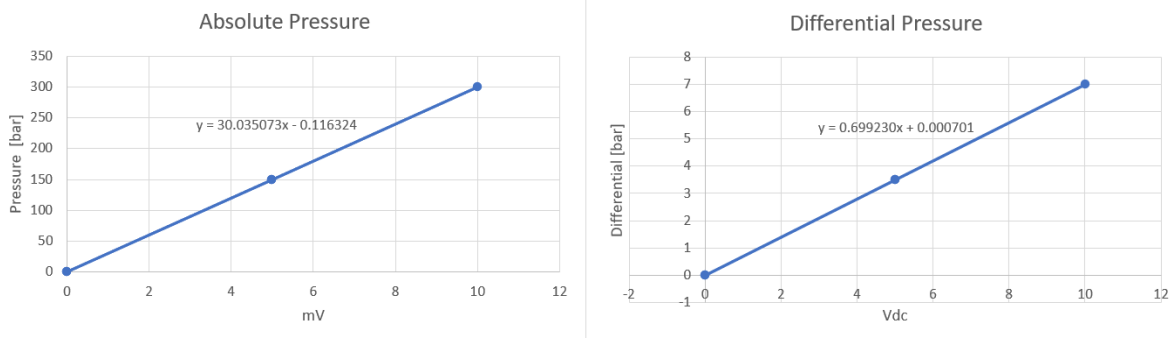

Figure 3.12: Sensor calibration curves

3.8 Surface Roughness Measuring

3.8.1 Microscope preparation [M4/M5]

The microscope measuring was done in two steps. The goal of the first phase was to characterize the true cross sectional area of the samples. At this scale, the dimensional accuracy of printing starts being proportionally more relevant, and it can not be assumed that samples have exactly the design area. Significant deviation from this design area could result in errors when calculating Reyolds numbers, and as a result, friction factors. In order to perform this measurement, channels were cut into thirds (56.5 mm each). The cutting was performed using EDM wire cutting, a form of electric discharge machining providing high dimensional accuracy and negligibly small effects in terms surface deformation. The two external sections were used to measure cross sectional area at two points on each channel.

Figure 3.13: Channel B1-45-B, processed for microscope analysis

The middle section of each sample was split open along the length, exposing both its internal upskin and downskin surfaces. These surfaces were then used to characterize the surface roughness of the channels. It should be noted that the side-walls of the channels are always inclined at 90° with respect to the build plate, and were not further investigated. While some dependency on the overall sample build angle may exist for these walls, it was assumed to be negligible. subsection 4.3.4 further discusses the averaging of upskin and downskin surface roughnesses to an average value for the sample, where the side-walls are assumed to have the same roughness level as those of the 90° samples.

3.8.2 Microscope Measurements [T2/T3/T4]

Measurements were performed using a Keyence VK-X3000. This microscope is capable of scanning surfaces using confocal scanning, focus variation, as well as white light interferometry. As discussed in section 2.4, the effective differences between these is relatively small (with a few exceptions). Focus variation was used for most measurements as it provides a reduced scan time over interferometry and confocal scanning. The focus variation was done optically in most cases, though a few surfaces could not be fully resolved. In these cases, the laser was used to obtain a slower but well resolved surface scan.

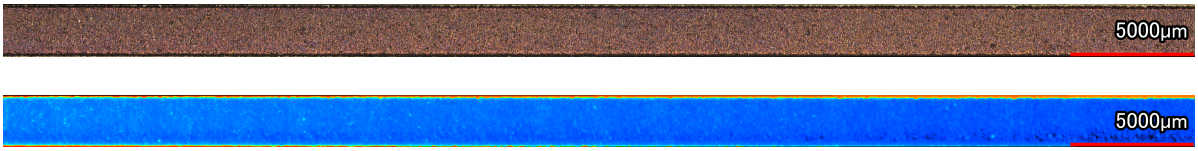

Figure 3.14: Example of stitched scan output after microscope inspection

Because a large amount of surfaces needed to be scanned, it was of interest not to scan the surfaces at an excessive magnification level. Higher magnification levels require more individual images to be taken in order to stitch together the full surface scan. For surface roughness scanning, magnification was set to 5X. No significant changes in measured roughness levels were found when further increasing this magnification level. However, 5X magnification enabled the scan image height to cover the full width of the channel surface, meaning the stitching grid consisted of only one image in height.

Chapter 4

Results and Analysis

4.1 Sample Selection

As explained in subsection 3.5.3, both sample batches suffered from a number of defects related to the printing and post-machining process. While these can typically be compensated for by repeating prints and adjusting parameters, time and budgetary limitations favoured the sub-selection of those that were successful for further flow testing. section D.2 provides an overview of exactly what defects were found on which sample/channel, and what testing they were eventually selected for.

A further sub-selection was made on what flow-testing data to use for further analysis. A few of the welds ended up creating a seam on the inside of the channel, causing the flow to be choked right before entering the sample. Pressure drop data from these samples was discarded after they were sectioned (visually confirming the presence of the weld seam). Data from the following channels was eventually used for analysis:

- Batch one 45°, channels A & B
- Batch one 90°, channels A, B & C

The complete set of samples were used for surface roughness analysis. In the following sections, results of both the flow testing and surface roughness are discussed. Although they were performed after the flow testing, microscope testing results are discussed first. The information retrieved from the microscope measurements is used to analyze the flow testing results, so it is more intuitive to address the surface quality first.

4.2 Internal Surface Analysis

Internal surface roughness was measured on both upskin and downskin surfaces of all channels, including those that were not flow tested. As evident from the theory discussed in section 2.3, there exists a large number of metrics by which the surface roughness can be characterized. The following sections discuss the data extracted from microscope measurements on the closed contour samples.

4.2.1 Visual Surface Feature Analysis

Before quantitatively analyzing the surface roughness, it is useful to assess the general trends and features displayed by scans of the sample surfaces. Scans presented in this section were all taken at a 10X magnification, and show a surface area of approximately 0.42 mm^2 (747 μm x 560 μm). The scans in Figure 4.1 and Figure 4.2 show the surfaces of the 90 degree samples (both open and closed contour shown). Note that while there is a reference to up- and downskin surfaces, these have the same build angle in the case of the 90 degree sample. The denomination was maintained for consistency, and to be able to identify the orientation of a surface inside the printer build volume.

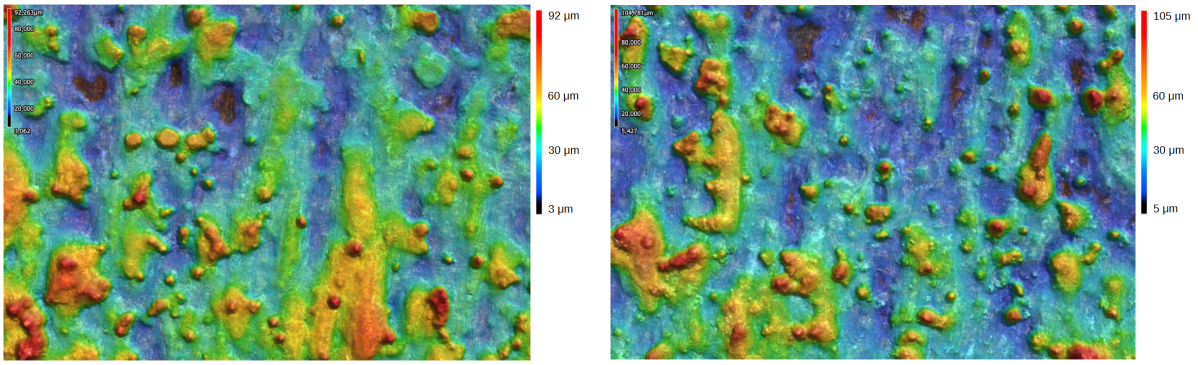

(a) Closed contour **(b)** Open contour

Figure 4.1: B1-90 downskin surface scans

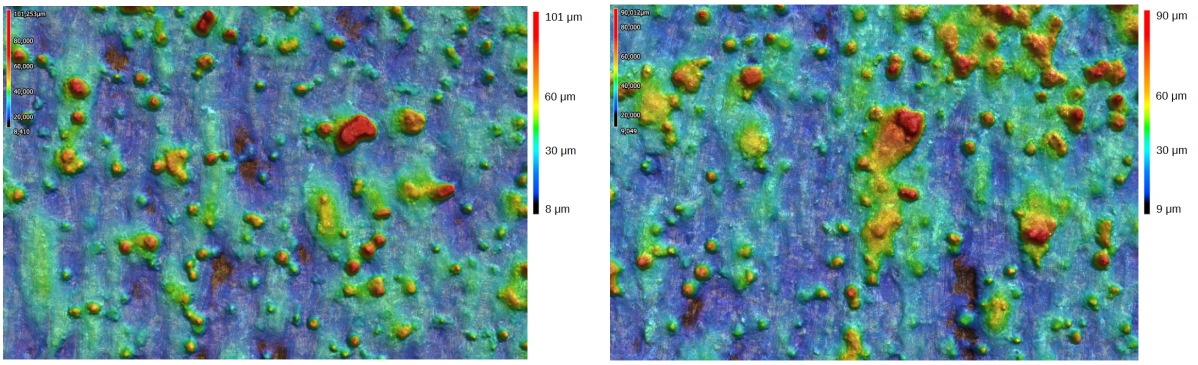

(a) Closed contour **(b)** Open contour

Figure 4.2: B1-90 upskin surface scans

The first observation to note is that the open contour surfaces are marked by very similar characteristics as the closed contour surfaces. This would suggest that surface roughness of open contour samples may be representative enough of closed contour channels to serve as a witness specimen, though this will be further investigated quantitatively in section 4.2.4. Interestingly, the surfaces printed at the orientation corresponding to the "downskin" denomination seem to show a slightly higher variation in surface height, though both up- and downskin surfaces remain very similar. The majority of the surface is flat and marked by striations parallel to the plane in which powder layers are added, and most irregularities seem to stem from isolated peaks. Upon closer inspection of visual scans (see Figure 4.3), they seem to originate from unmelted powder particles. They are relatively scattered and mark a stark difference with respect to the otherwise homogeneous surface texture.

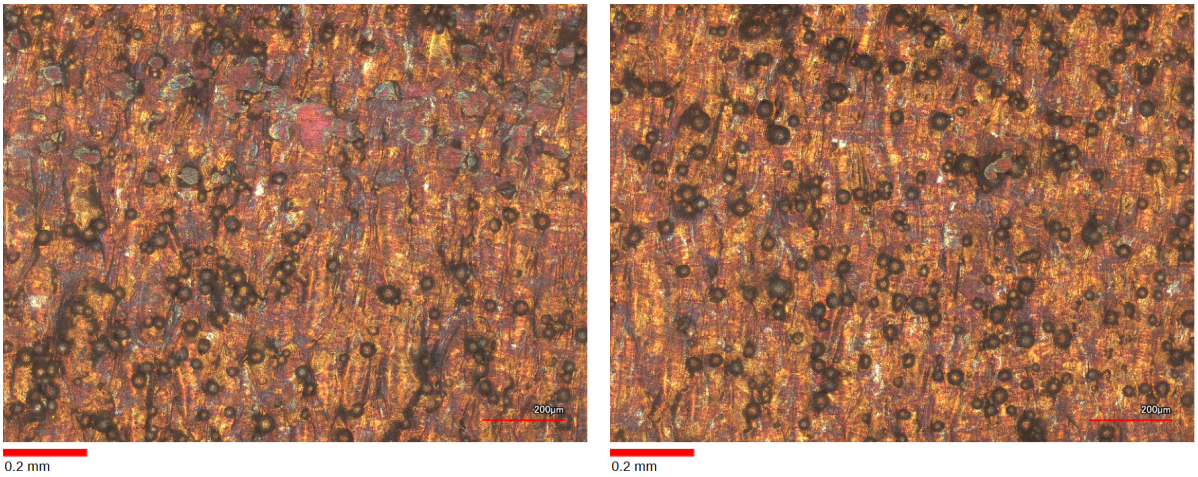

(a) 90° "Downskin" **(b)** 90° "Upskin"

Figure 4.3: Optical scans of 90° closed contour surfaces

These optical scans further show that the "upskin" oriented samples printed at 90° have significantly more unmelted particles that the downskin orientation at the same build angle. While these surfaces were printed at the same build angle within the same machine, their different orientation means they are differently exposed to the inert gas circulating through the build volume. This difference is addressed numerically in subsection 4.2.4. The same scans for the samples printed at 60° are shown in Figure 4.4 and Figure 4.5.

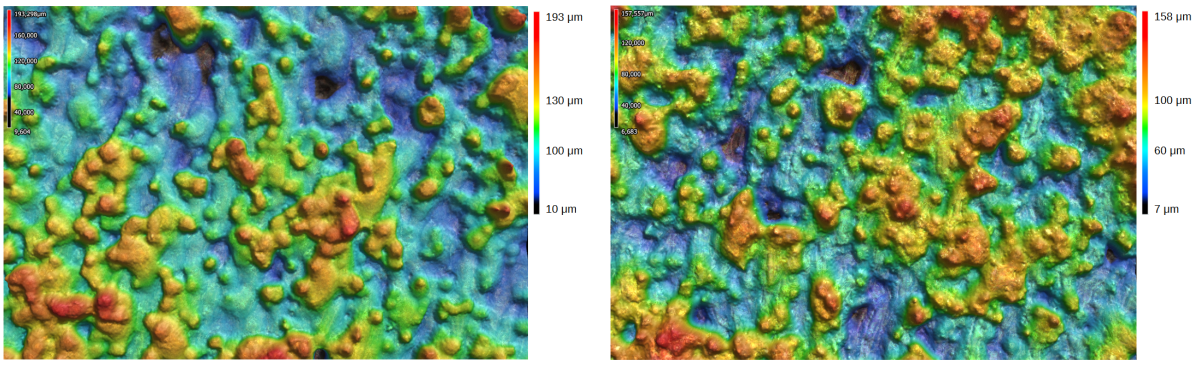

(a) Closed contour **(b)** Open contour

Figure 4.4: B1-60 downskin surface scans

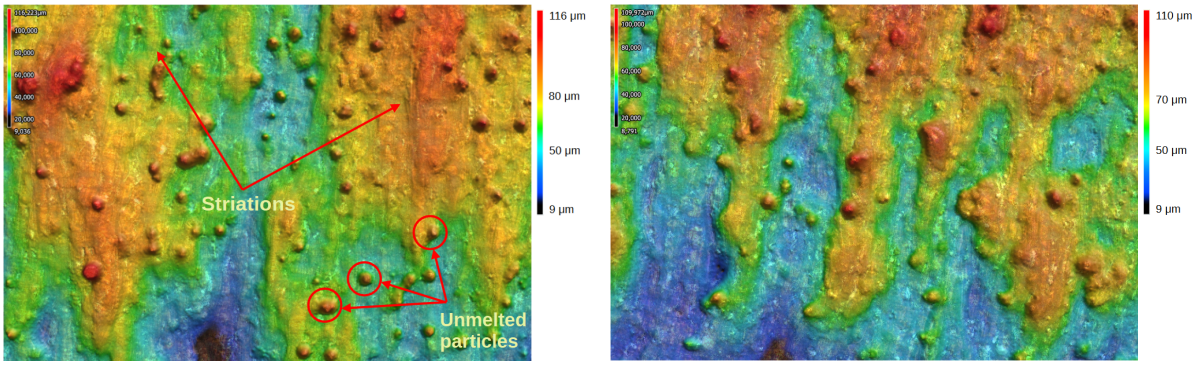

(a) Closed contour **(b)** Open contour

Figure 4.5: B1-60 upskin surface scans

When the print angle is reduced, upskin and downskin surfaces display different behaviour. Comparing Figure 4.4 to Figure 4.1, the downskin surface shows a significant increase in surface irregularity. The overhanging nature of the 60° downskin surfaces causes the meltpool to droop as it is solidifying, a surface defect known as "balling".

On the other hand, tilting the surface upskin reduces the quantity of unmelted particles (though not completely eliminated) and does not introduce any form of balling. However, the surfaces are marked by larger scale striations, most likely due to the stairstep effect being introduced in angled surfaces.

Once again, open contour scans show very similar behaviour to their closed contour counterparts, further indicating the potential usefulness of open channel witness specimens. Finally, scans of the 45° samples are shown in Figure 4.6 and Figure 4.7. The 45 degree samples were the lowest printed build angles.

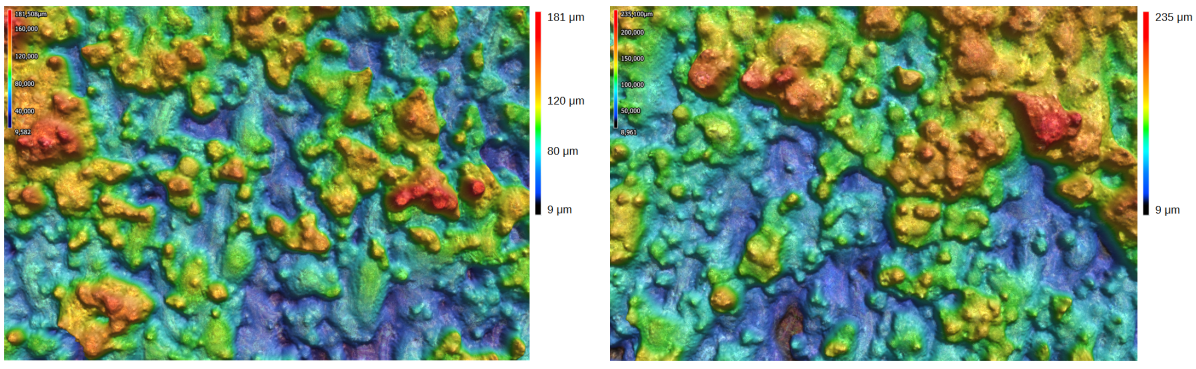

(a) Closed contour **(b)** Open contour

Figure 4.6: B1-45 downskin surface scans

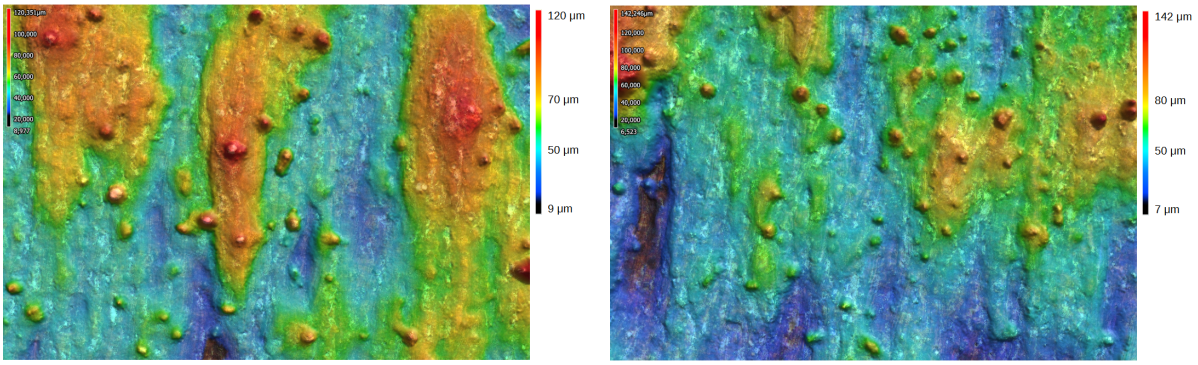

(a) Closed contour **(b)** Open contour

Figure 4.7: B1-45 upskin surface scans

The 45° samples very clearly show a continuation and strengthening of the trends seen in the 60° samples. Downskin surfaces become even more irregular, and upskin surfaces continue to show striations with less unmelted particles. Visually there does not seem to be a very large difference between the 45° and 60° upskin surfaces. The measurements discussed in subsection 4.2.4 will in fact reveal that there is also a quantitative overlap in terms of surface roughness between these two surfaces. Once again, the 45° samples do not show visually significant deviations between open and closed contour channels. The following sections turn to the quantitative analysis of these surfaces.

4.2.2 Sampling Area

The surface analysis presented in this study focuses primarily on areal surface roughness parameters. It is important to ensure then, that parameters are derived from sufficiently large sampling areas to properly represent the roughness of the entire channel. For the majority of channels, the surface roughness metrics were derived using the entirety of the available area of the middle section. The microscope magnification level was set to 10X to allow a surface to be measured using a one dimensional grid. The grid of images was then stitched using Keyence analysis software in order to derive parameters from one continuous scan. While the microscope offers larger magnification levels, they were not found to be of significant influence on the measured parameters. Any larger magnification level however increases the measurement time by a minimum of factor two, as the scan needs to be stitched from a two-dimensional grid, thus justifying the selection of 10X as a baseline.

In a few cases, the sampling area was reduced in order to avoid significant features skew the measurements. This was primarily done for large features such as the witness lines present on some samples (see section D.2). Figure 4.8 shows the sampling areas used for each sample. As shown in the chart, lower build angles required more concessions to be made due to witness lines than the higher build angles. On 90° samples, the entire sample area could consistently be scanned.

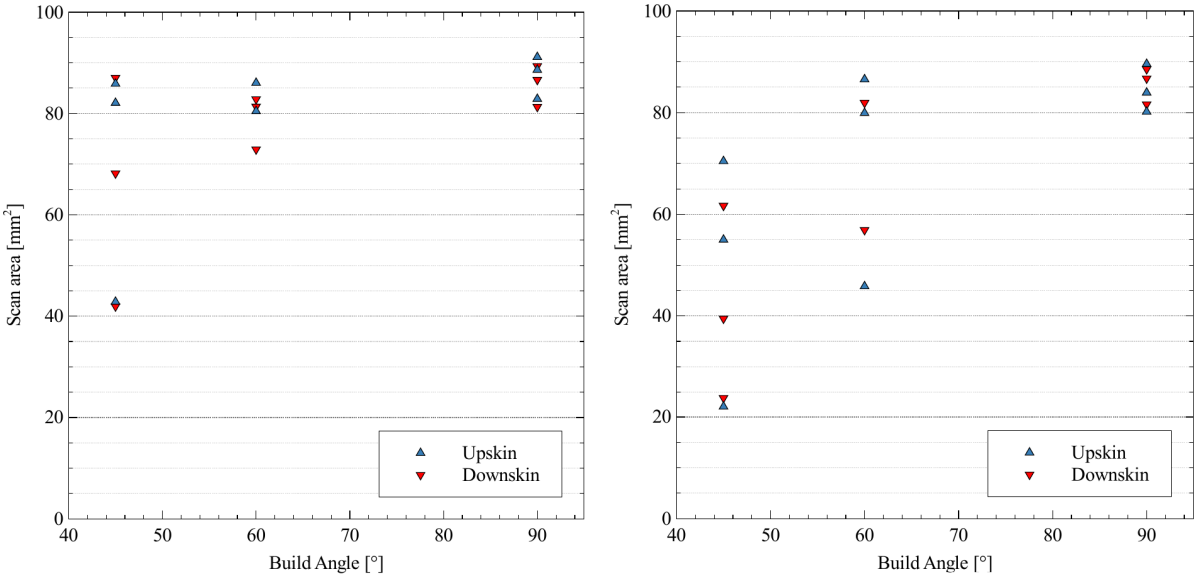

(a) Batch one **(b)** Batch 2

Figure 4.8: Microscope scan areas for both batches

4.2.3 Form Correction and Data Filtering

The areas sampled as described above were used to calculate all roughness metrics discussed in this chapter. Prior to calculating these, a number of corrections were made on the surface height maps. Primarily, the surface form of the height maps generated with the microscope had to be corrected for either one of the following:

- **Surface tilt**: When the sample is installed under the microscope, it inevitably will not be perfectly horizontal. The 'plane tilt' filter corrects for this by calculating a mean flat plane, and setting that as the reference plane for measuring surface height
- **Surface curvature**: Some samples curved away from the center line when they were cut open, due to the release of internal stresses that weren't alleviated by heat treatment. Where surface curvature correction was applied, no further plane tilt correction was needed.

The obtained data sets can be can be done by removing either the Waviness or Roughness components. Waviness consists of the larger wavelength oscillation in surface form. In this particular case, Primary roughness parameters were studied, meaning they constitute a combination of Roughness and Waviness (see subsection 2.3.1 for a more in depth discussion on the distinction). This decision was made because in the context of fluid channel performance, the flow is essentially agnostic to the surface form/roughness wave lengths.

An exception to this approach was made for the *Ra* calculations. Here, a 25mm cut-off wavelength was used to filter out surface form stemming from the curvature of the samples. This was done because the software allows for surface form curvature correction only on areal measurements, but not on linear track measurements. As such, without the filtering, Ra values were significantly higher than Sa values. While it is true that the flow technically "sees" all wavelengths of surface texture, in this case the curvature was caused purely by the manufacturing steps required to make these measurements (e.g. release of internal stresses during sample preparations). The flow was therefore not actually subjected to this curvature

during flow testing.

For samples that did not bend after the EDM machining, a simple plane tilt was applied to correct for the sample inclination during scanning. Adding a 25mm cut-off wavelength to these samples was found not to have an influence on the measured *Ra* values, further confirming that a plane-tilt correction was sufficient.

4.2.4 Areal Arithmetic Mean Height [Ra/Sa]

Figure 4.9 shows the Sa values of all channels in batches one and two. "Down" facing markers indicate the roughness for the downskin surface of the relevant channel, while "Up" facing markers indicate that for the upskin. Note that the denomination of "up" and "down" facing surfaces was maintained for the 90° inclined sample. While there is no distinction between up and down in this orientation, the denomination corresponds to the ridge marker used to differentiate between surfaces. This translates into the specific orientation of the surface in the printer as shown in Figure 3.2. This can have an influence on surface roughness as explained in subsection 2.5.2.

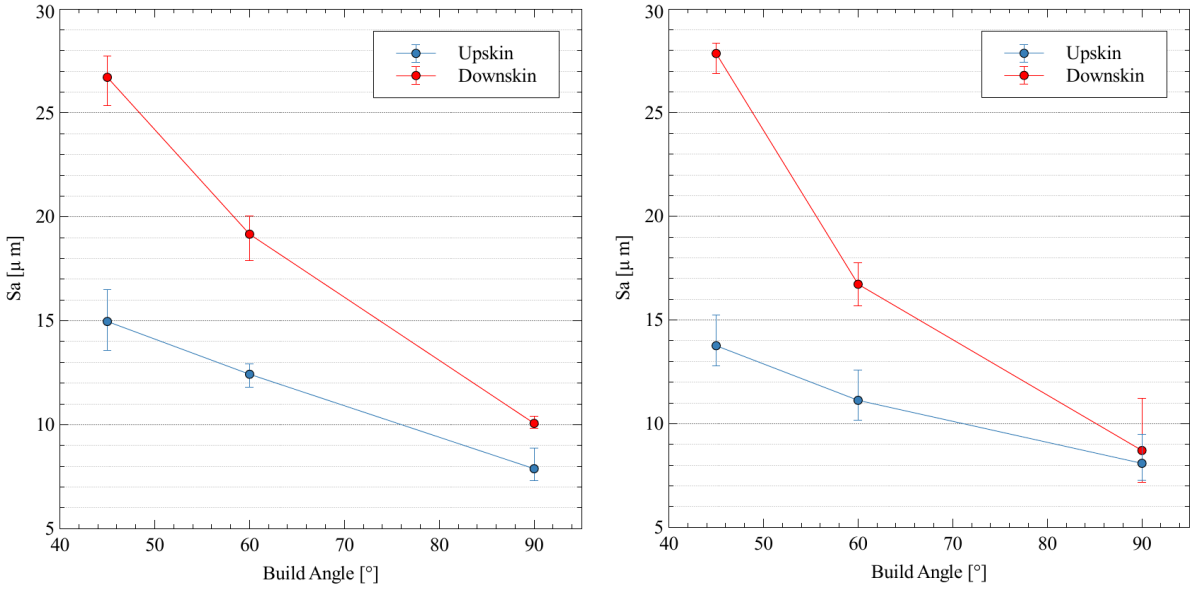

(a) Batch one

(b) Batch two

Figure 4.9: Sa values for both printed batches

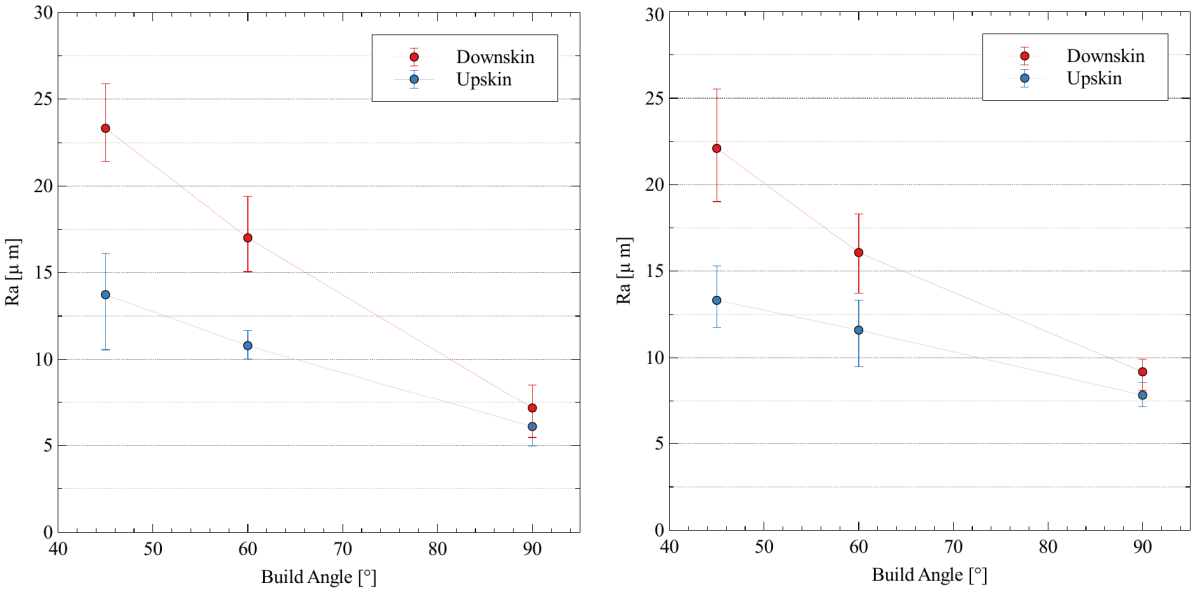

(a) Batch one

(b) Batch two

Figure 4.10: Ra values for both printed batches

For the areal measurements shown in Figure 4.9, error bars of each data point reflect the spread of Sa values measured on each channel within a sample. For the linear data, each channel was additionally sampled on 10 different tracks, so error-bars reflect the spread across 30 measurements on three different surfaces. The linear measurements were taken on a track length of of 43.5 mm.

Both sample sets show a very consistent trend of surface roughness reducing with increasing build angles. Roughness of the down facing 45° surface is in the order of 25-27 μm, while the 90° surfaces sit in the range of 7-12 μm. Furthermore, the difference between upskin and downskin surfaces nicely converges as the angle is increased, reducing from approximately 14 μm at 45° to 4 μm at 90° incline.

Recoater blade comparison

The purpose of this study is primarily to investigate the effect of only build angle on various surface roughness and performance parameters. To be able to attribute observed differences to the build angle, it was necessary to limit the variation of other parameters as much as possible. As a result, build angle was the only processing parameter that was varied within the print.

However, machine/facility availability at 3DSystems resulted in the two batches to be printed with two major differences. Firstly, the two batches were subjected to different heat treatment processes (see Table 3.5). Secondly, batch one was printed using a carbon blade recoater, while batch two used a soft blade. It is therefore necessary to assess what role these differences may play when comparing the results across the two batches. Note that in terms of analyzed surface areas, these are the only two differences that could play into a difference in surface roughness. Factors like surface kinks and witness lines will have had an influence on the affected areas, but these areas were excluded from the microscope measurements in order to avoid skewing the roughness data.

An average up- and downskin roughness was calculated for each sample. Values for batches one and two were then compared to each other using:

$$Sa_{avg}deviation = \frac{Sa_{avg,batch1}}{Sa_{avg,batch2}} \cdot 100\% \tag{4.1}$$

Here, the deviation is defined as a percentual difference of batch one over batch two. A positive deviation indicates a higher average surface roughness for batch one, while a value closer to 0% indicates stronger similarity. Figure 4.11 shows the evolution of this difference over each build angle for both up- and downskin surfaces.

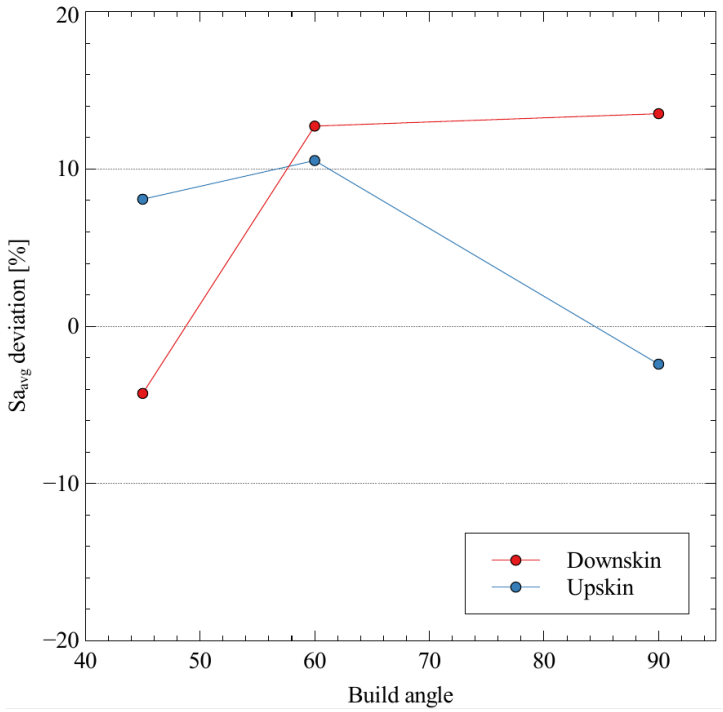

Figure 4.11: Average *Sa* deviation

This comparison shows that, for most surfaces, the roughness of batch one is around 10-12% higher than for batch two. This is consistent with results found by Lee et al. [44], who found that while sharp metal blades provide the most uniform density along the recoating direction, rubber/silicone blades provide a more consistent layer thickness and lower surface roughness. Exceptions are found for the downskin surfaces at 45°, and the "upskin" oriented surfaces at 90°. While these surfaces show a higher average roughness on batch one they both indicate a <5% deviation.

It should be noted that while the tendency indicates a higher roughness for batch one the deviation remains within the average spread of roughnesses found within a single sample. For example, a 10% deviation of the 60° downskin surface (approximately 19 μm on batch one) results in an average difference of 1.9 μm. The roughness spread within the 60° downksin surfaces of batch one is 2 μm. So while the averages do indicate a general tendency for batch one surfaces to have higher roughness levels, they are certainly within boundaries that allow for a meaningful comparison.

Witness Section Surface Roughness

Subquestion three (see section 3.1) of the research question investigates the difference in surface roughness between channels that are printed with an open face, and regular closed contour channels. The purpose of this question is directly aimed at understanding how surface quality can be verified for parts that cannot be destructively inspected.

To do this, each sample was printed with two open channels. By switching their orientation, every sample would also provide information on both upskin and downskin surface roughness for open channels. The surface roughness of these open channels could then be compared to the data presented in subsection 4.2.4. Figure 4.12 Shows the Sa of up and downskin open surface channels in solid color. Near each data point, the non-colored markers indicate the Sa values of the closed channels on the corresponding sample.

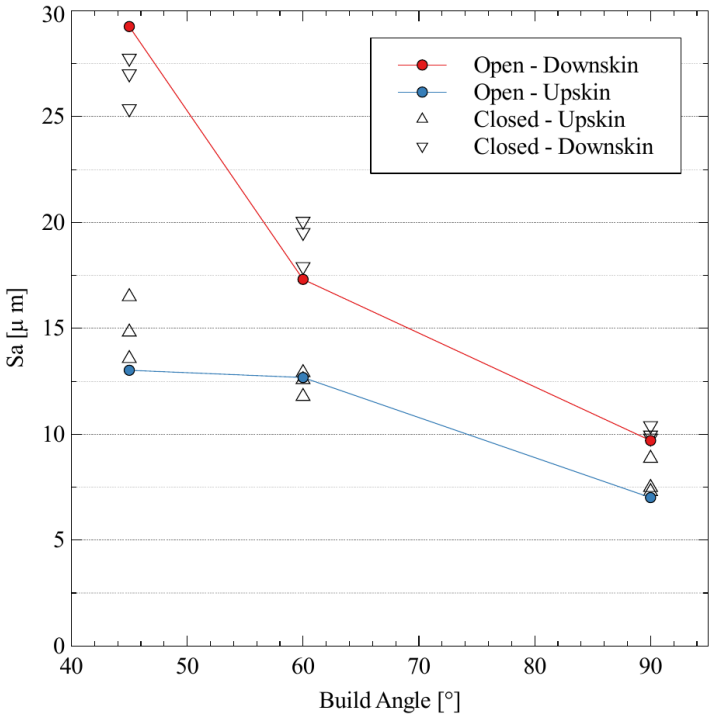

Figure 4.12: Open contour surface roughness

As can be seen, closed channel values remain largely within a range of 5 μm of the open channel equivalent. One might note that the deviation between open channel and its closed channel equivalents tends to reduce as build angle increases. At 45° the largest deviation is 5 μm, while at 90° the open channel sits in the middle of the range. This might suggest that other sources of roughness are acting as a function of the build angle, such as the sample orientation with respect to the inert gas flow inside the print chamber. Average Sa values shown in Figure 4.9 further indicate that this deviation is consistent for 90° samples across batches. Recommendations regarding this difference are made in chapter 6.

More relevant to sub-question three, for straight square channels of approximately 2mm in rib height, the data indicates that open contour channels provide a good indication for internal surface roughness. This information may prove useful in the printing of witness specimens for internal geometries such as fluid micro-channels, whose performance is very dependent on its

surface quality.

4.2.5 Peaks and Valley Heights [Spk/Svk]

The reduced peak height, Spk, and reduced valley height, Svk, offer insight into how high/deep the average peaks and valleys of the surface are. They are calculated as the mean height/depth of the peaks/valleys that extend beyond the core surface. Franco and Sinatora [28] describe the physical interpretation of these parameters as follows: Spk corresponds to the surface material that may be worn out in the initial contact with another surface – peaks above the core – and Svk represents valleys/pits whose depth goes down beyond the core and that might be filled with debris coming from the peaks.

In the context of fluid flow, a high Svk value may indicate that, though the roughness of the surface is high, valleys do not "obstruct" the flow, and may be of lower impact on the pressure drop. Conversely, a high Spk presents more "obstacles" to the flow, and might be interpreted as a more impactful parameter. Spk values for both batches are shown in Figure 4.13.

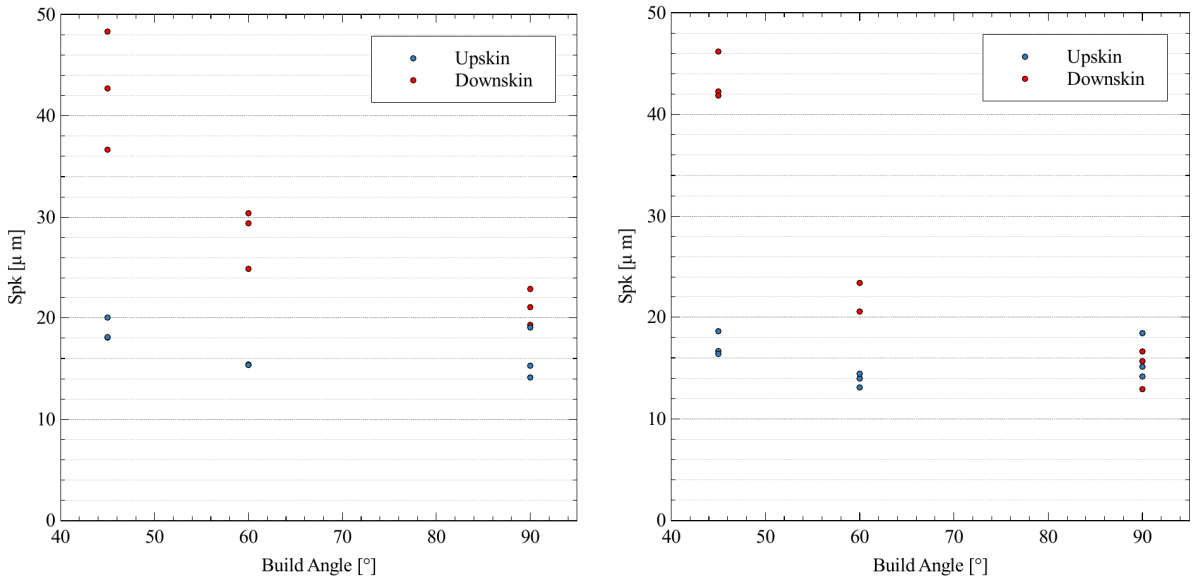

(a) Batch one

(b) Batch two

Figure 4.13: Spk values for both printed batches

Both batches show only minor variation of the upskin Spk with build angle. Downskin surfaces on the other hand show a much stronger correlation with build angle. The 45° overhanging surfaces have an average peak height approximately twice as high as its upskin counterpart, before converging to the same values at 90°. As the scans discussed in subsection 4.2.1 have shown, the irregularities in upskin surfaces are dominated by the presence of scattered unmelted particles. This stands in contrast to the downskin surfaces, which suffer from dross and have a much more uniformally irregular surface. This shows that the reduction of surface roughness with increased build angle for upskin surfaces may not necessarily originate from a reduction in peak height. The Svk graphs in Figure 4.14 offer further insights.

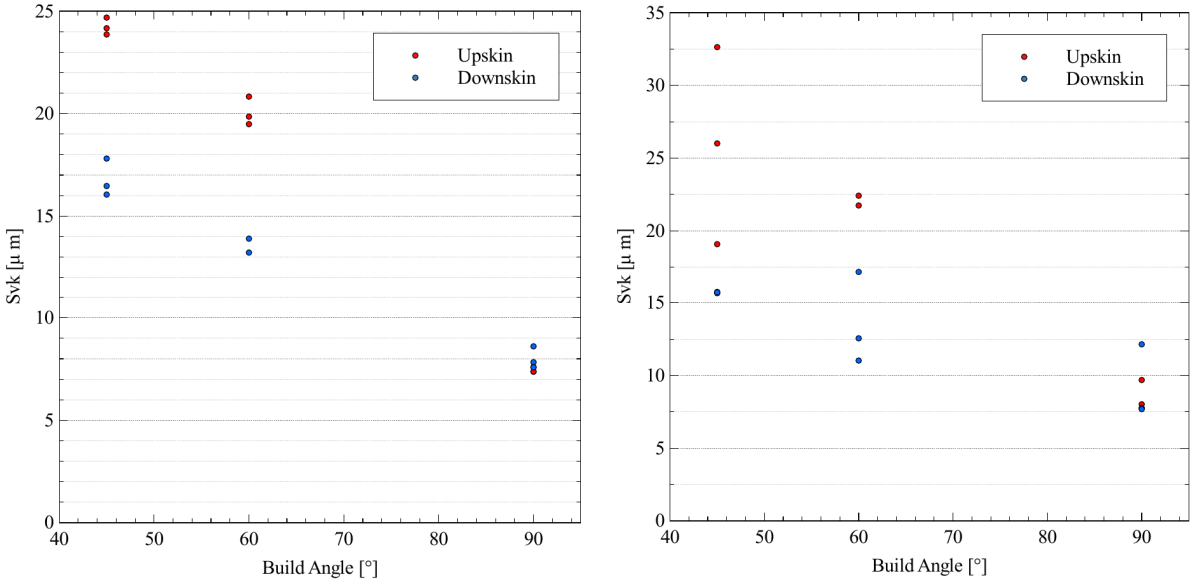

(a) Batch one

(b) Batch two

Figure 4.14: Ra values for both printed batches

The Svk parameter shows a stronger correlation with build angle for upskin surfaces. In fact, downskin Svk at 45° is only about 50% higher than the upskin Svk. The spread in the 45° data of Figure 4.14b can be attributed to an insufficient sampling area. The witness lines on the surfaces of batch two caused sampling areas to be lower, especially at 45° (see subsection 4.2.2).

4.2.6 Skewness [Ssk]

The Skewness and Kurtosis parameters, Ssk and Sku, can be seen as measures for whether or not a surface is dominated by valleys or peaks, and how sharp these are. Negative skewness indicates a plateau-like surface dominated by valleys, which reduces overall friction and increases wear resistance in contact situations [58].

As shown in Figure 4.15, all surfaces have positive skewness, meaning they are all dominated by peaks. Low build angle upskin surfaces however show a skewness close to zero, indicating the surfaces are symmetrically distributed. For more vertical surfaces the skewness increases significantly on both batches, which could potentially be due to the surface roughness being dominated by protruding unmelted particles. The trends are less clear on downskin surfaces, possibly due to the highly irregular nature of the surfaces.

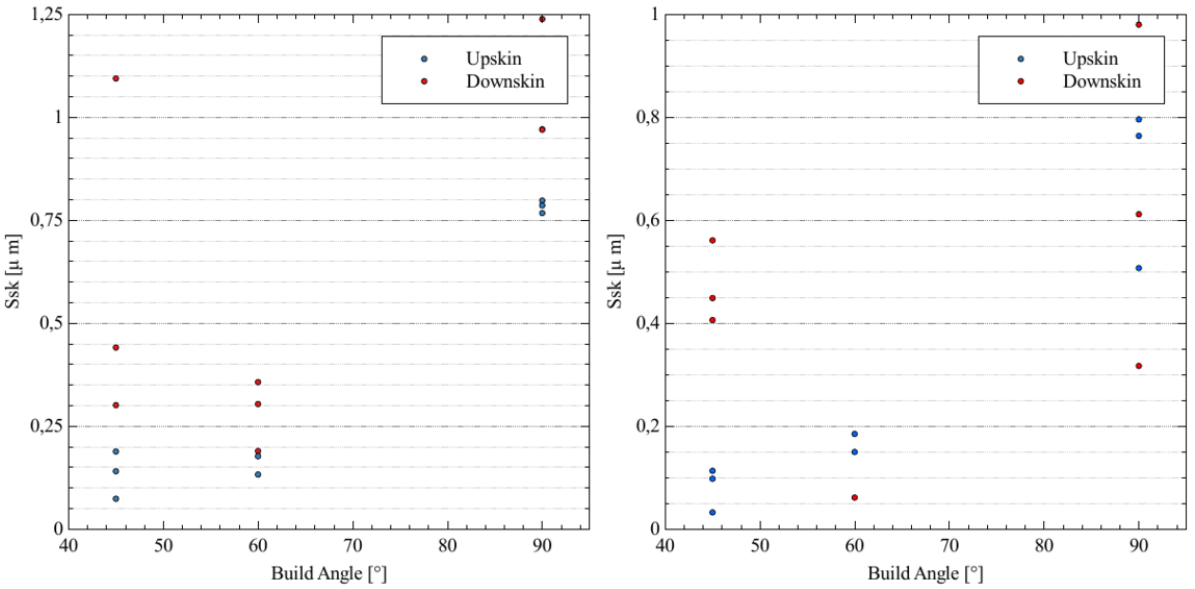

(a) Batch 1 (b) Batch 2

Figure 4.15: Skewness - Ssk

4.2.7 Visual Cross Sectional Analysis

The build angle affects not only the surface roughness but also the surface form (also referred to as dimensional accuracy). Figure 4.16 shows the cross sectional scans of the 45° and a 90° samples in batch one. As evident from Figure 4.16b, apart from an unmelted particle on the right wall, all four walls are relatively equal in form and roughness. In contrast, the down skin surface of the 45° sample (top surface in the image) is significantly less regular than the three remaining walls. In addition to the roughness, the scan shows that the overall surface form is also different, showing a more curved surface that interestingly extends upwards.

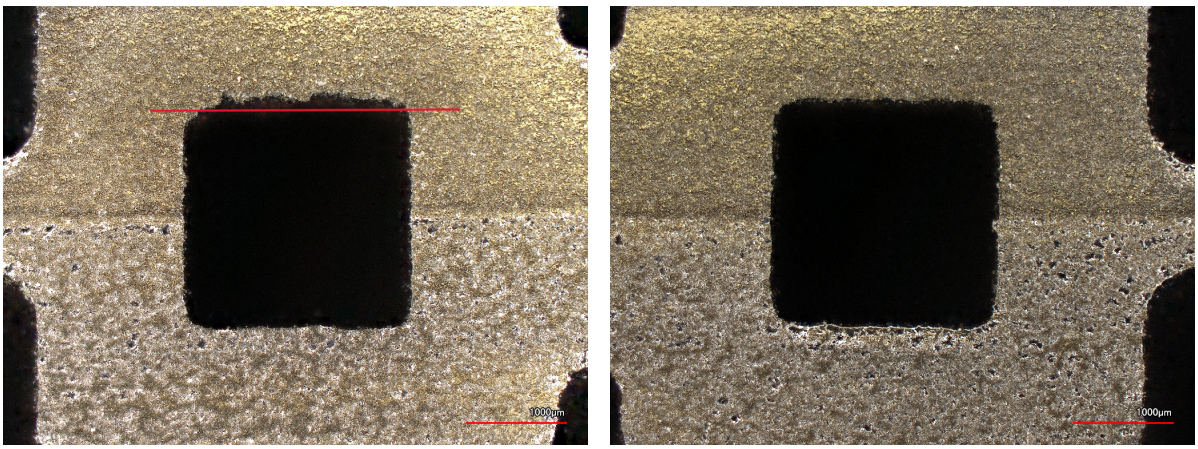

(a) B1-45-A **(b)** B1-90-A

Figure 4.16: Cross sectional scans of samples B1-45-A and B1-90-A

This difference in roughness and surface form highlights two things. Firstly, the varying surface form confirms that theoretical/design cross sectional areas cannot be used to calculate flow properties and friction factors. subsection 4.2.8 further details how the cross sectional areas were corrected for each channel to account for this. Secondly, the four walls clearly have

different surface roughnesses when a sample is printed under an angle. This means some attention should be paid to how an average channel surface roughness may be derived, as it may not be a simple case of averaging over the up and downskin surfaces. This is addressed in more detail in subsection 4.3.4.

4.2.8 Cross Sectional Area Measurements

To illustrate the impact of dimensional accuracy on the assessment of the friction factor, both a theoretical and a true Colebrook factor were calculated for each data point. The theoretical factor was based on the sensor data, but uses the design geometry to derive flow speed and Reynolds number.

The true Colebrook friction factor was derived by first assessing the true cross sectional area of the samples. After flow testing, the concerned samples were split into three sections. The middle section was then sliced open to allow the measurement of internal surface roughness, while the outer two sections were left intact for measuring cross sectional area. Figure 3.13 illustrates sample B1-45-B after sectioning and slicing.

Scans of the cross sectional areas were then used to derive a true cross sectional area for the samples that had been flow tested. This was done using ImageJ, an image analysis tool developed by the National Institute of Health and the Laboratory for Optical and Computational Instrumentation [4]. The tool was used to convert the cross sectional images into a Binary 8-bit to aid with the automatic detection of surface edges. The tracing tool was then used to outline the perimeter of the cross section, as shown in Figure 4.17.

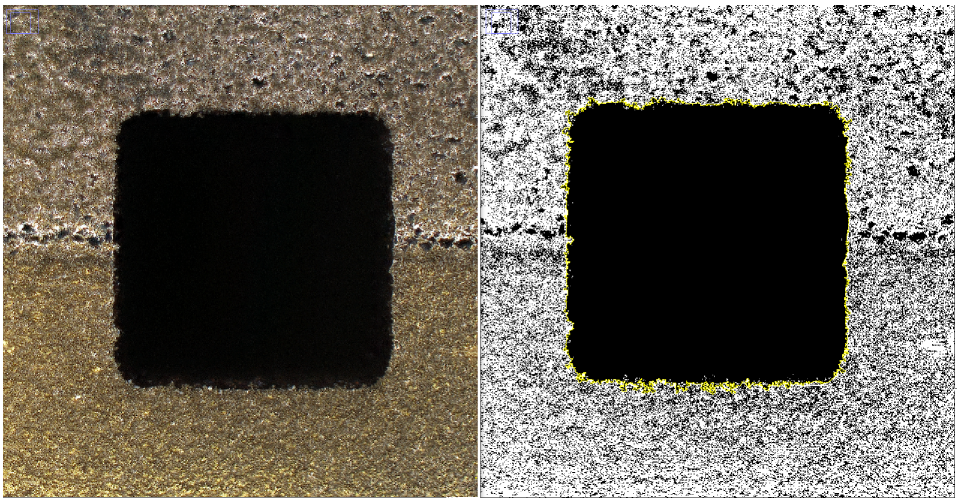

Figure 4.17: Cross sectional area measurement, processed w/ ImageJ [4]

In some cases, the converted image caused some of the porosity to be taken into account as part of the surface profile, due to the lower pixel density. In these cases, a paintbrush tool was used to locally alter the image and constrain the detected contour to the actual surface contour. Figure 4.18 shows how a porous cavity in the material gets detected as a surface feature by ImageJ. Use of the paintbrush tool then allowed the exclusion of this feature from surface contour measurements:

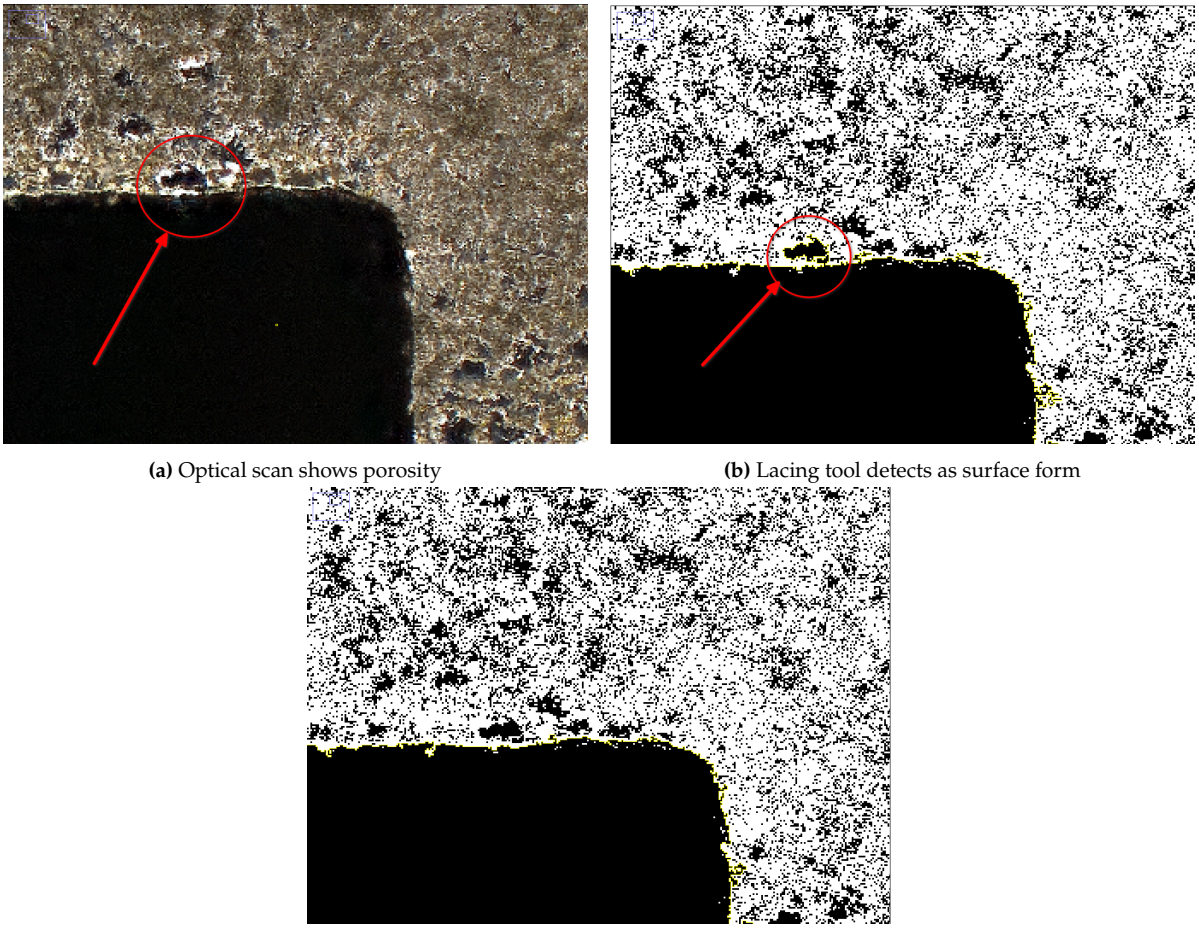

(a) Optical scan shows porosity

(b) Lacing tool detects as surface form

(c) After correction, porosity no longer accounted for

Figure 4.18: Correction process for areal measurements, processed w/ ImageJ [4]

Firstly, as evidenced by Figure 4.17, the cross sectional images show an interesting feature running horizontally through the cross section. This was found to be the case in all cut samples, of both batches. The center line of this feature aligns with the thin plate printed to connect individual channels to each other within one sample, as explained in subsection 3.4.5. It is likely that the feature seen in the cross section stems from the increased resistance in the EDM wire as it moved through this sheet during the sectioning process. As the roughness of this surfaces is not investigated, it is of no further consequence to the results discussed below.

Once the contour was identified, the measurement tool of ImageJ was used to calculate the flow area of the section. With the exception of one channel, all flow tested channels turned out to have a cross sectional area approximately 25% higher than the design value. These deviations were larger than expected, so measurements were repeated to rule out scan errors. Furthermore, the consistency of cross sectional areas across two sections of the same sample indicates it is unlikely that the deviation came from measurement mistakes. With the exception of one channel, the deviation was found to be consistent across all measured channels.
Measured surface areas and perimeters are shown in Figure 4.19a and Figure 4.19b respectively. The two measured sections on each channel correspond to the two external sections of the cut sample (see Figure 3.13).

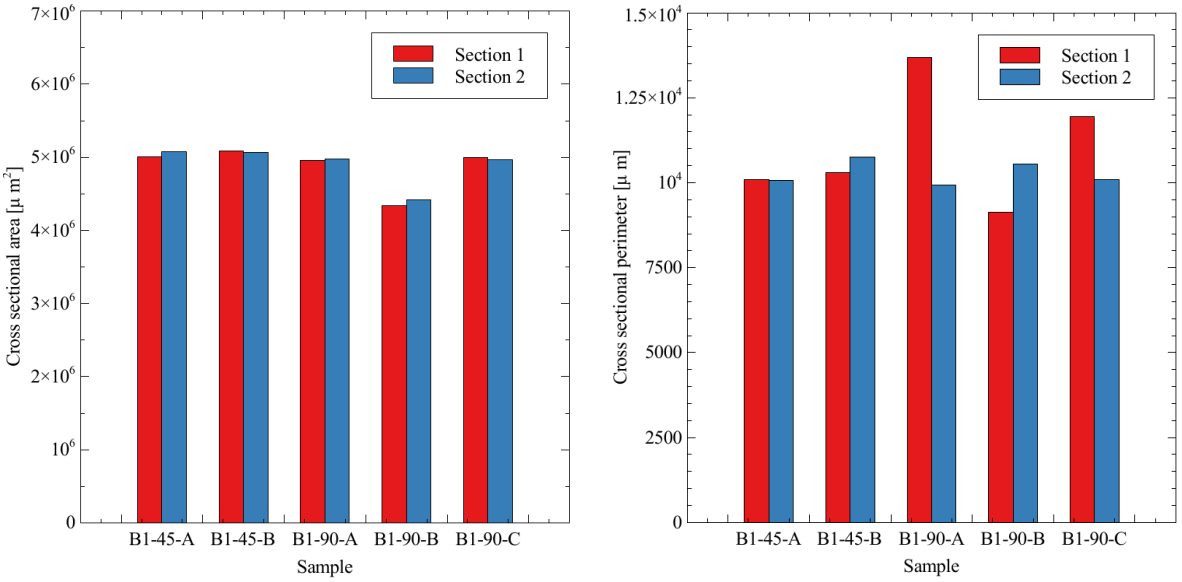

(a) Cross sectional areas

(b) Cross sectional perimeters

Figure 4.19: Area/perimeter measurements

Details on the measured cross sectional areas and their deviation from design values are resumed in Table 4.1. The relative average deviation is calculated by taking the absolute average deviation, and expressing it as a percentage of the averaged cross sectional area. Here, the absolute average deviation is essentially the average deviation of data points from the mean value. Since two cross sections were measured for each channel, a low relative average deviation indicates that both data points lie very close to each other, and gives more confidence that two data points are a valid set for estimating the average cross sectional area of the entire channel. As can be seen below, all data points lie within 1% of the data set average.

Table 4.1: Cross sectional area measurements for flow tested samples

Sample	**Cross sectional average [μ m^2]**	**Design deviation [%]**	**Relative average deviation [%]**
B1-45-A	5038925.596	25.97	0.68
B1-45-B	5075888.155	26.9	0.19
B1-90-A	4969133.771	24.23	0.18
B1-90-B	4376216.924	9.41	0.93
B1-90-C	4981598.39	24.54	0.35

While it is true that a correction is typically applied over the delivered step file before printing to account for some shrinkage, it is unlikely that it would be of this order of magnitude. This may point to operator errors at the time of applying these margins, as all other processes were applied to the entire sample as a whole and would not have resulted in different cross sectional areas within the same sample. Samples were cut at the same points, and the same measurement technique was applied to all sections. The measuring process was repeated from scratch to ensure the result was repeatable. This underscores the importance of this intermediate step between flow testing and surface roughness measurements, and the fact that the areas were quantified means they are of no further consequence on the accuracy of presented data.

4.3 Flow Test Results

This section addresses the results of the flow tests performed on the subset of samples detailed in section D.2.

4.3.1 Geometrical Parameters

The analysis of sample pressure drops and associated friction factors depends heavily on the geometric properties of the samples. As addressed by the sample design requirements (Table 3.3) and further sample selection (see subsection 3.5.3), measure were taken to limit the sources of pressure drop to surface roughness only. However, the dimensional accuracy of the printing process was not a controlled parameter in this experiment, and inevitably caused some deviation from design values. As addressed in subsection 4.2.8, flow tested samples showed deviations in cross sectional areas from their design values, as well as between each other.

This cross sectional area is relevant for determining flow speed and hydraulic diameter, two parameters which directly influence the Reynolds number and friction factor. It is therefore relevant to discuss how these area variations were interpreted, and ultimately used to calculate channel friction factors.

Assuming the sample areas shown in Table 4.1 are fully and effectively utilized by the flow, these measurements can be used to directly derive flow speed using:

$$v = Q/A \tag{4.2}$$

The hydraulic diameter can be derived by further assuming that the cross section is square-shaped. Another approach might be to use the perimeter lengths to do so, but given the deviations between two sections on the same sample were significantly larger than for the areas, the former approach was chosen:

$$D_h = \sqrt{A} \tag{4.3}$$

The assumption that the full cross sectional area is effectively available to the flow is likely to be incorrect however, as the boundary layer created by the surface roughness risks being of consequent effect in case of high relative roughness. As proposed by Kandlikar [38] and discussed in section 2.2, the constricted diameter can be used to account for this effect. Using the constricted flow theory, a constricted flow hydraulic diameter can be derived from the theoretical one using:

$$D_{h,cf} = D_h - \epsilon \tag{4.4}$$

Where ϵ represents average surface height, as shown in Figure 4.9. Constricted flow equivalents of the Reynolds number and friction factor can then be calculated based on this value. To assess the difference between each approach, all flow test data was processed using both methods.

4.3.2 Flow Properties

The flow rate itself was derived from the flow controller flowrate (given in normal liters per minute, Ln/min), and the air pressure/temperature. It is calculated using:

$$Q[L/min] = Q[NLPM] \cdot \frac{T_{gas}}{293.15} \cdot \frac{1.013253}{p_{gas}[bar]} \tag{4.5}$$

Temperature and pressure at the sample inlet were used, as they most closely reflect the conditions at the flow controller placed just upstream. The derived Mach numbers were observed to lie in the range of 0.21-0.22. Subsequently, the Sutherland equation was employed to determine the viscosity for each data point:

$$\mu = \frac{\mu_0 \left(\frac{T}{T_0}\right)(T_0 + C)}{T + C} \tag{4.6}$$

Where C is the Sutherland constant. Furthermore, density was calculated using isentropic relations, which adjusted for temperature and pressure relative to a reference point at ambient conditions:

$$\frac{\rho_1}{\rho_2} = \left(\frac{p_1}{p_2}\right)^{\frac{1}{\gamma}} \tag{4.7}$$

Based on the derived parameters, the Reynolds numbers for each experiment were computed as follows:

$$Re = \frac{\rho V D_h}{\mu}, \quad Re_{cf} = \frac{\rho V_{cf} D_{h,cf}}{\mu} \tag{4.8}$$

Here, the hydraulic diameter is derived from the cross sectional area. In the case of constricted flow, it is corrected using the average surface height as discussed in subsection 4.3.1.

4.3.3 Pressure Drop and Friction Factor

The pressure drop through the samples with respect to flow rate and Reynolds number are shown in Figure 4.20:

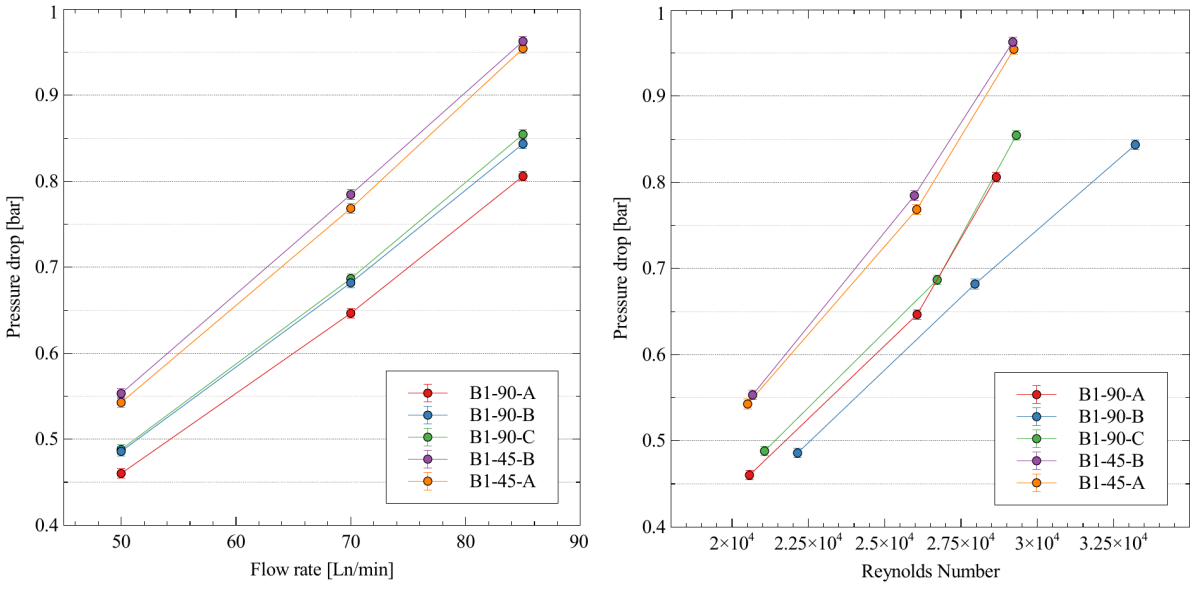

(a) Pressure drop by flow rate

(b) Batch two

Figure 4.20: Pressure drop by Reynolds number

Figure 4.20a essentially shows the raw data obtained from the flow testing: differential sensor output as a function of flow controller input. Error bars indicate the differential sensor accuracy range. The data shows a clear increasing trend of pressure drop with increasing flow rate. Furthermore, a clear separation is shown between the pressure drop through low build angle samples (B1-45A/B) and high build angle samples (B1-90-A/B/C). At 85 Ln/min, the pressure drop through the 90° samples reaches around 0.84 bar, while the 45° samples reach 0.96 bar. This marks a 14% increase over the lower build angles.

Figure 4.20b shows the same pressure drops plotted against the Reynolds number (non-constricted). Calculations show that Reynolds number in the order of $2e4$-$3e4$ where reached. Constricted flow Reynolds numbers are in the same order of magnitude.

Because the pressure drops were experimentally determined and correlated to flow rate and speed, the resulting friction factors could be explicitly determined using the Darcy-Weisbach equation:

$$f = \frac{2\Delta P D_h}{\rho L v^2}, \quad f_{cf} = \frac{2\Delta P D_{h,cf}}{\rho L v_{cf}^2} \tag{4.9}$$

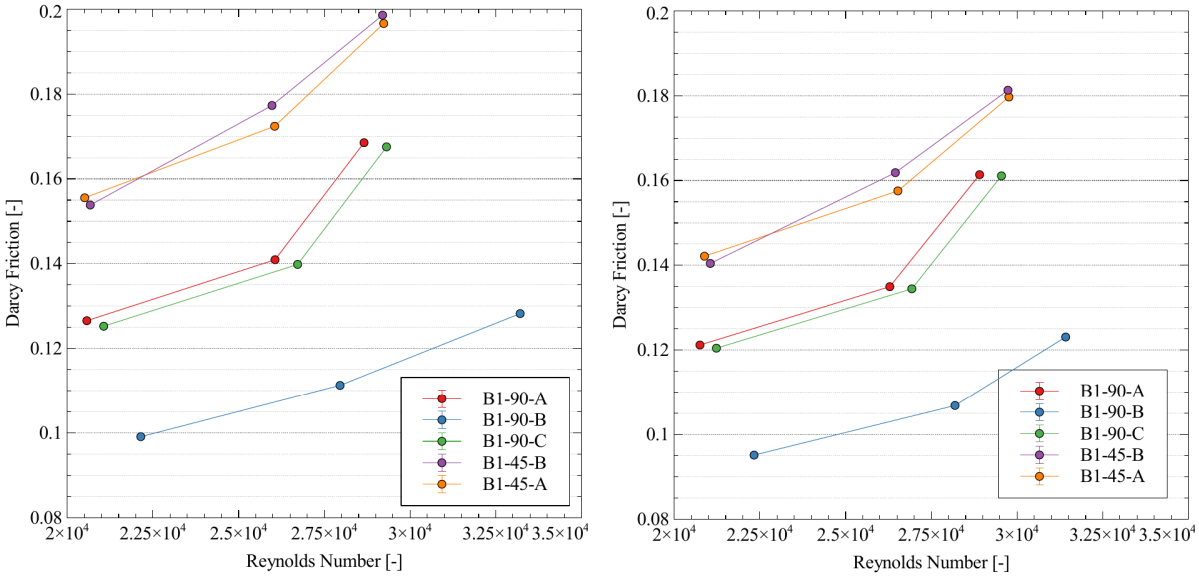

(a) Colebrook Friction factors

(b) Constricted flow friction factors

Figure 4.21: Derived friction factors

Results indicate that, in the range of tested Reynolds numbers, the friction factors increased with an increase in flow rate for any given sample. Generally speaking, friction factors tend to decrease as flow transitions from laminar to turbulent regime, as shown in the Moody charts Figure 2.4. It should be noted however that that trend holds true if the relative roughness is held constant. The relative roughness having a dependency on flow conditions means that for a single channel, friction factors actually increased over the measured range of Reynolds numbers.

At similar flow conditions, lower build angles consistently resulted in a higher friction factors. This is in agreement with the trends in pressure drop found in Figure 4.20, and aligns well with anticipated patterns.

4.3.4 Relative and Sand grain Roughness

The friction factors presented above were derived by explicitly solving the for the darcy friction coefficient as shown in Equation 4.9. This equation relates flow conditions directly to friction factor. The Moody charts shown in Figure 2.4 however, are derived from the Colebrook equation, which relates the darcy friction coefficient to flow Reynolds number and an equivalent sand grain roughness:

$$\frac{1}{\sqrt{f}} = -2log\left(\frac{\epsilon/D_h}{3.7} + \frac{2.51}{Re\sqrt{f}}\right) \tag{4.10}$$

Because the friction factor and Reynolds numbers were both experimentally determined, this equation can be solved for the relative roughness ϵ/D and the equivalent sand grain roughness ϵ:

$$\left(\frac{\epsilon}{D_h}\right) = \epsilon_{rel} = 3.7\left(10^{\frac{-1}{\sqrt{f}}} - \frac{2.51}{Re}\sqrt{f}\right) \tag{4.11}$$

$$\left(\frac{\epsilon}{D_h}\right)_{cf} = \epsilon_{rel,cf} = 3.7\left(10^{\frac{-1}{\sqrt{f_{cf}}}} - \frac{2.51}{Re_{cf}\sqrt{f_{cf}}}\right) \tag{4.12}$$

Where Equation 4.12 is used to correct the relative roughness using constricted flow theory. Evaluating this equation returns an equivalent sand grain roughness that, according to the Colebrook equation, would generate the observed friction factors at the given flow Reynolds numbers.

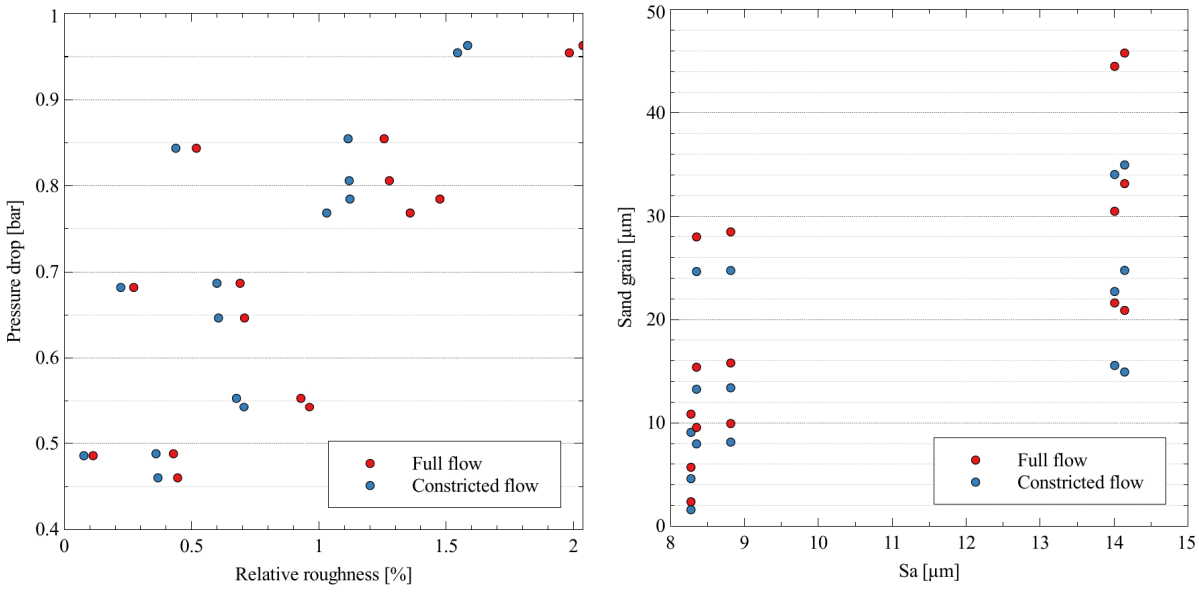

(a) Pressure drop by relative roughness

(b) *Sa* by eq. sand grain roughness

Figure 4.22: Relative and Sand grain roughnesses

In these graphs, each point represents a specific channel, at a specific test condition. To do so, an average surface roughness of each channel was calculated based on the up- and downskin measurements discussed in this chapter. It was assumed that an average/effective *Sa* value could be derived by averaging over the roughness of all walls in the channel. The top and bottom surfaces were pulled directly from measurement results. The two vertical walls were

accounted for by taking the average 90° inclination roughness from that specific batch. Relative roughness was then determined using Equation 4.11, and for each channel the equivalent sand grain roughness was calculated by multiplying by its hydraulic diameter.

The trends in Figure 4.22 show how the pressure drop changes with relative roughness, and how the measured Sa relates to equivalent sand grain roughness at tested conditions. It is important to note that this relative/sand grain roughness is not solely a surface characteristic like the Sa. As discussed in subsection 2.3.2, the concept of sand grain roughness originally comes from the coating of pipes with sand grains filtered to a specific particle diameter. These pipes were then characterized and related to Reynolds numbers and friction factors through empirically determined relations.

However, relating experimental data back to an equivalent sand grain roughness using these relations means there is a dependency on Reynolds number and friction factor, which both vary as fluid properties change under different test conditions. Ultimately this means that a single channel, despite having a fixed Sa, will have an equivalent sand grain roughness that is dependent on the flow conditions under which it is operated. Figure 4.23 shows how this ratio of equivalent sand grain roughness to the average Sa and average Sq (i.e. weighed average over four channels walls) changes as the friction factor varies:

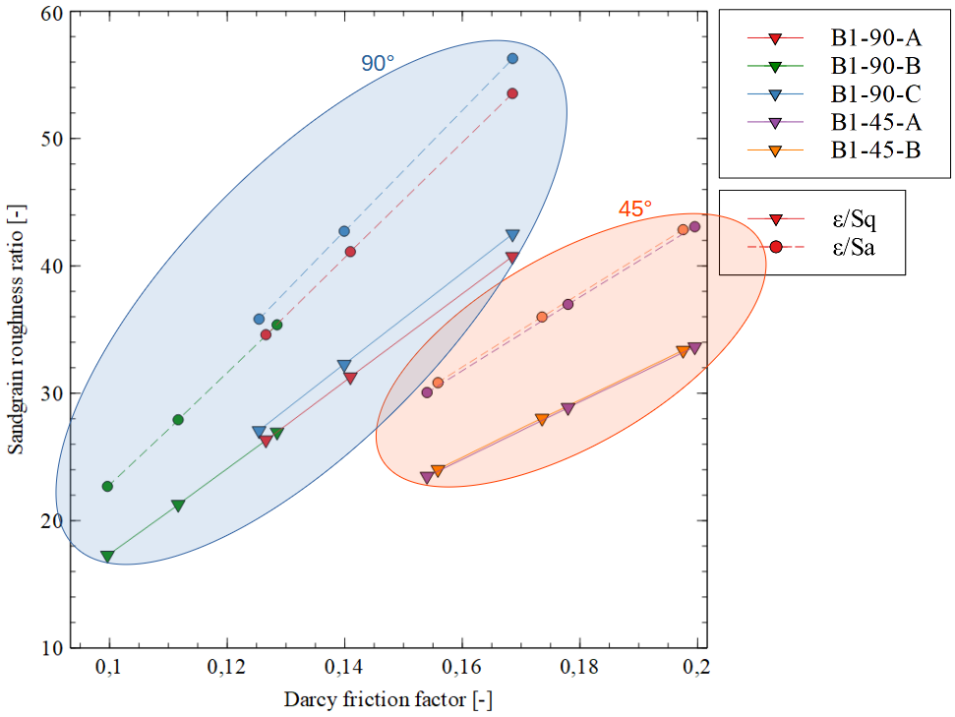

Figure 4.23: Equivalent sand grain roughness ratios

Here, individual colours correspond to tested samples. Continuous lines represent the ratio of equivalent sand grain roughness to Sq, while dotted lines are the ratios to Sa. As evident from the plot, the equivalent sand grain roughness (as explicitly derived from the Colebrook equation) varies with the friction factor as a channel is put through a range of fluid conditions. Over the range of tested conditions, the samples show a linear increase of the equivalent sand grain roughness ratio. Using the Sq parameter, ratios are smaller and slopes are slightly reduced, indicating this parameter might be a better fit for relating surface roughness to

equivalent sand grain roughness. Interestingly, the smoother 90° surfaces appear to reach higher sand grain roughness ratios than the 45° samples at equal friction factors. Plotting the sand grain roughness against the friction factor reveals a linear relationship between the two, as shown in Figure 4.24a. In Figure 4.24b, the friction factors are plotted against relative roughness values for all flow tested samples:

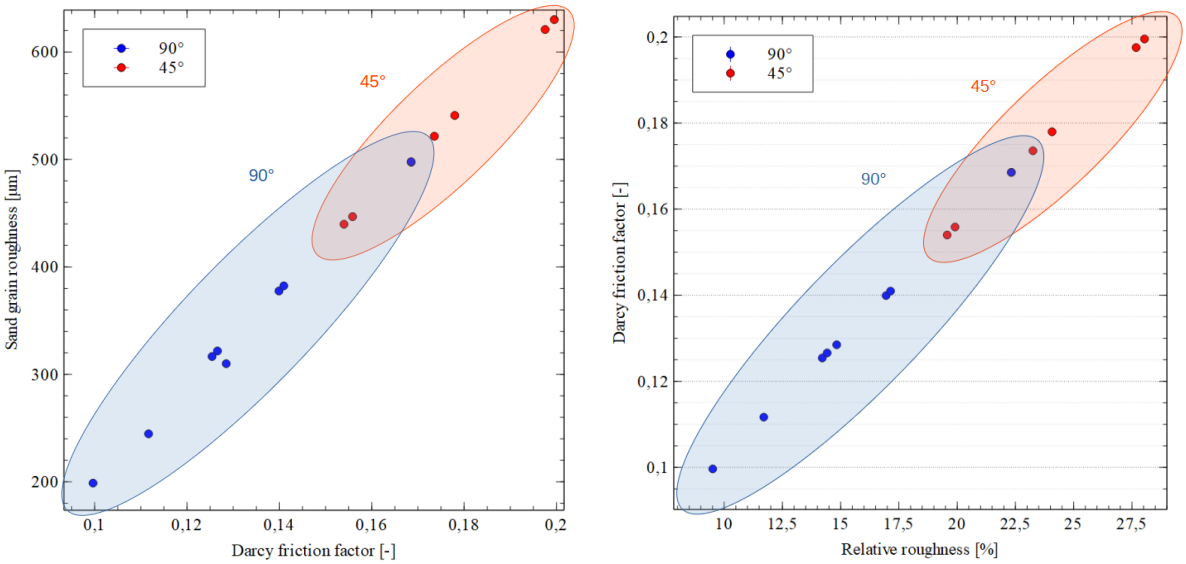

(a) Equivalent sand grain roughness by friction factor

(b) Relative roughness by friction factor

Figure 4.24: Friction factor by relative roughness

In the tested conditions, samples ranged in relative roughness from as low as 10% up to approximately 27%. 90° samples formed the lower end of this range, reaching a maximum value of 22.5%, while the 45° samples started at 20%. As these charts show, the relation between relative roughness and friction factor is clear.

Furthermore the values are significantly higher than the 5% used for creating the Moody charts. This relative roughness however is calculated with an equivalent sand grain roughness, and the challenge remains deriving this sand grain roughness from optically determined parameters such as $Sa/Sq/$etc. While the data shown in Figure 4.22b does indicate a tendency for higher Sa values to translate to a higher equivalent sand grain roughness, there is still a significant amount of overlap in the data.

Despite being relatively scattered, the relative roughness appears to be relatively correlated with the pressure drop. An increase in relative roughness clearly results in an increased pressure drop. This trend can be attributed to two things. Firstly, an increase in relative roughness is caused by a shifting in Reynolds number to change test conditions. A higher Reynolds number reduces the last term of Equation 4.11. Secondly, a lower build angle results in a higher Sa_{avg}, which is positively correlated to the sand grain roughness and increases pressure drop.

4.3.5 Experimental Data Comparison

To put the presented data in context of larger scale studies, it is useful to compare the relative roughnesses found in the flow tested samples to those found by Stimpson [62], previously discussed in section 2.2. This study was reviewed in more detail in section 2.2. Figure 4.25 shows all the data gathered by Stimpson. The relative roughness levels found on his samples are indicated by the horizontal dotted lines, and vary from 8% to 45% for the non-smooth channels. The overlaid blue bounding box indicates the range of Reynolds numbers over which the experiments presented in this thesis report were performed.

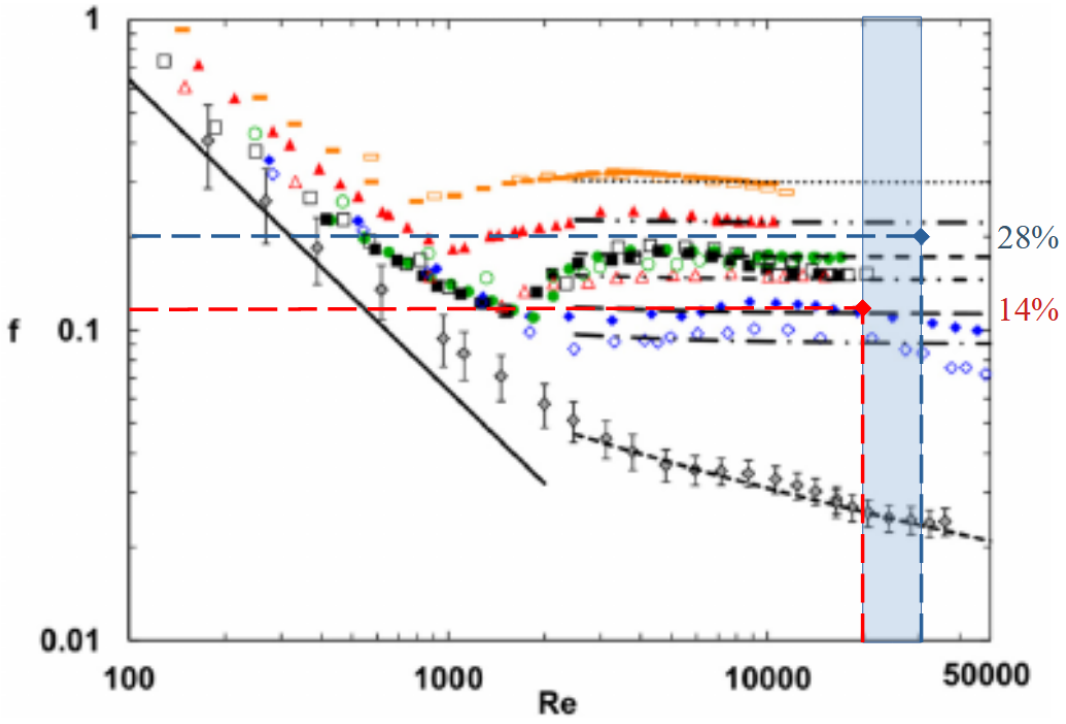

Figure 4.25: Comparison of experimental results with findings from Stimpson [62]

Two data points, one at each end of the range, were compared with the data from Stimpson. At the lower end of the Reynolds number range, sample B1-90-A (at 50 Ln/min) is indicated in red. The friction factor, calculated from the flow test data, was approximately 0.12. On the upper end of the range, sample B1-45-B (at 85 Ln/min) is indicated in blue. Its calculated friction factor was approximately 0.2. Using the true hydraulic diameters and equivalent sand grain roughnesses, relative roughnesses were calculated as shown in subsection 4.3.4.

The resulting relative roughnesses are indicated in percentage on the right hand side. At 85 Ln/min, sample B1-45-B had a relative roughness of 14%. The overlay on the graph aligns with Stimpsons' 12% line. At 50 Ln/min, sample B1-90-A had a relative roughness of 28%. The overlay on the graph lies in between Stimpsons' 23% and 32% lines. This shows that despite having higher hydraulic diameters and inlet pressures, the relation between Reynolds number, friction factor and relative roughness reported in this experimental study are consistent with results found by Stimpson [62].

4.4 Summary of Results

In this chapter, results of all phases of the test campaign were presented and analyzed in the context of research questions detailed in chapter 1. The test campaign consisted broadly of three phases: Flow testing, cross sectional area measurements, and surface roughness measurements. The various steps required to prepare for and perform these tests were detailed in the test plan overview shown in Table 3.2.

4.4.1 Flow testing

The first tests consisted of pressurized air flow tests on a subset of all printed samples. The subset was selected based on a review of the various defects all samples were subjected to. Defects were found to have been introduced at various stages of the printing/machining process:

- A number of printed samples displayed witness lines, causing significantly sized features on the inside of the channels
- Internal stresses, relieved during the separating of channels from each other, caused some channels to bend out of plane
- Two samples were clogged due to the weld seam extending into the channel flow path
- A few samples from the first batch were kinked at the entry due to a printing error

The samples selected based on this selection were used to calculate pressure drops at various flow conditions. From these, the friction factors were explicitly calculated. Cross sectional area scans were used to correct Reynolds number (as opposed to calculating it directly from the design cross sectional area). The calculated friction factors were found to lie between 0.1 and 0.2 over the range of tested fluid conditions, indicating that the bottom range of friction factors was in fact higher than the highest friction factor for which the Moody charts are applicable. At similar flow conditions, samples printed with lower build angles (e.g. higher surface roughnesses) exhibited higher friction factors.

The cross sectional area measurements revealed a higher area than intended by design, indicating a possible operator error at the time of applying correction factors for preventing unwanted sample shrinkage after printing. The corrected values were used for all flow calculations to ensure pressure drop was accurately processed.

4.4.2 Surface Roughness Measurements

After flow testing and cross sectional area measuring, samples were sliced open along the length to expose the internal surfaces. Samples were sliced using EDM machining in such a way that up and downskin surfaces were left untouched. Here, build angle was found to be inversely and linearly related with surface roughness. Sa values for vertical surfaces were found to lie the range of 8-10μm, while 45° downskin surfaces were most rough at 25-27μm. Within individual channels, downskin surfaces consistently had higher roughness than upskin surfaces. Measured surfaces were additionally shown to be positively skewed at all build angles, indicating they are dominated by peaks. Lower build angles showed a more symmetric distribution than vertical surfaces.

A comparison between the two batches (isolating the effects of build angle and surface orientation) revealed that the differences in recoater blade resulted in a maximum difference of 12%, i.e. within the error range of comparable surfaces printed on the same batch.

Finally, the comparison of open and closed channels of equal surface build angle and orientation revealed that open contour channels provide a good measure for closed contour surface roughness.

4.4.3 Relative and Sand Grain Roughness

Data from all test phases was combined to asses the relative roughness and equivalent sand grain roughnesses of the channels. Relative roughnesses were found to lie between 10% and 28%, further indicating that the samples (at these flow conditions) lie outside of the applicability range of the Moody charts (<5%). Furthermore, the dependency of equivalent sand grain roughness on friction factor (and therefore fluid conditions) was shown. Finally, while plotting the sand grain roughness against Sa showed a general positive correlation, the large amount of overlap indicates that it remains difficult to separate the flow conditions from the Sa - sand grain roughness relation.

Chapter 5

Conclusions

The research detailed in this report was conducted within the framework of a master's thesis focusing on the application of additive manufacturing to the spaceflight industry. Progress in manufacturing technologies like Laser powder bed fusion has led to greater use of Additive Manufacturing (AM) in designing combustion chambers and nozzles. This advancement allows for the creation of more intricate and efficient solutions, but generates the need for a better understanding of how surface roughness in micro-channels used for engine cooling relates to build angle and performance. The following research question was posed to guide this experimental thesis:

"How does the build angle of Laser powder bed fusion manufactured micro-channels relate to their internal surface roughness and fluid flow performance?"

To answer this question, six samples containing a total of 18 channels were printed. The printing was performed at 45°, 60° and 90° build angles, with the objective of investigating the relation between build angle, surface roughness, and friction factor. Pressure drops were measured across a range of air flow rates using a differential pressure sensor and flow controller to adjust the fluid conditions. The results were used to calculate friction factors, relative roughness and equivalent sand grain roughnesses for all channels. The acquisition and analysis of this data was aimed at answering above research question by addressing a specific set of sub-questions. Each sub-question is answered in the following sections.

Influence of build angle on surface roughness [SQ-1]
The first research sub-question was intended to provide insights on the direct influence build angle has on surface roughness. While generally well understood, it was important to verify the coherence of investigated samples with expected trends before performing more in-depth analysis. On the range of tested samples and angles, the build angle was found to be inversely and linearly related with surface roughness, with 45° surfaces exhibiting the highest Sa values. Within individual channels, downskin surfaces consistently had higher roughness than upskin surfaces.

These findings were consistent with expectations from both theory and experimental literature, and confirmed that the samples provided a good baseline for further analysis. Measured surfaces were additionally shown to be positively skewed at all build angles, indicating they are dominated by peaks. Lower build angles showed a more symmetric distribution than vertical surfaces.

Finally a small yet notable difference was found in surface roughness when comparing the two different recoater blades. The use of different recoater blades on the two batches was an unintentional manufacturing mistake, and an investigation of its impact roughness was done to ensure it had no consequential influence on other results. The trends were found to be consistent with literature, and small enough to fall within the roughness spread of a single sample.

Influence of build angle on friction factors [SQ-2]
The second research sub-question was aimed at determining the friction factors of samples at tested conditions, and relating this back to the build angle of the channel. Understanding the variation of friction factor with build angle is particularly relevant for cooling channels in liquid rocket engines, as they will tend to follow the contour of a nozzle or combustion chamber, resulting in various build angles along the track of a single channel.

Sample friction factors were calculated using experimental pressure drop data obtained from flow testing, and evaluation of the Darcy-Weisbach equation. Cross sectional microscope scans were used to correct the cross sectional areas for deviations with respect to their design values. The calculated friction factors were found to lie between 0.1 and 0.2 over the range of tested fluid conditions. This indicates that the bottom range of friction factors was in fact higher than the highest friction factor for which the Moody charts are applicable. At similar flow conditions, samples printed with lower build angles (e.g. higher surface roughnesses) exhibited higher friction factors.

Open-contour witness specimen analysis [SQ-3]
The objective of the third research sub-question was to understand if open contour channels could provide a good indication of roughness levels inside channels that cannot be destructively inspected before operation. Due to potential roughness induced by exposure to gas flow and spattering from neighboring surfaces, this similarity is not straight forward.

A comparison of surface roughness between closed contour channels and open contour equivalents was carried out. Investigation of the open contour channel roughness revealed good accordance with roughnesses found in closed contour samples. At equal build angles and under the same printing orientation (with respect to gas flow and recoater blade directions), open contour witness channels offer a good measure for the surface roughness of closed contour counterparts. These results indicate that open contour witness channels could be used to microscopically verify roughness levels of chamber/nozzle channels before the operation of the engine, or application of further post-processing steps.

Relation of performed measurements to primary research question [SQ-4]
The final research sub-question aimed at relating the found friction factors and surface roughness measurements to each other and back to the primary research objective of fluid flow performance. This was primarily done by calculating the relative roughness levels based on friction factors, cross sectional area measurements, and microscope measurement results.

Relative roughnesses were found to lie between 10% and 28%, confirming that small channels can fall outside of the applicability range of the Moody charts (originally created using tubing with up to 5% relative roughness). The equivalent sand grain roughness as derived from explicit evaluation of the Colebrook equation was shown to have a strong dependency on flow conditions. Additionally, trends of equivalent sand grain roughness with respect to Sa showed that while the general tendency indicates higher Sa values map to higher sand grain roughnesses, there is significant overlap in the data and it is difficult to separate the flow conditions from this relation.

Conclusion
The space industry is experiencing significant growth: demand for access to space is on the rise, which has translated to a need for scalable solutions while concurrently driving down

the costs associated with development and operational aspects. Among other aspects, access to space relies heavily on liquid propulsion. By extension, manufacturing represents a major element in the optimization of both cost and development time.

The implementation of additive manufacturing for combustion chamber nozzles has the potential to revolutionize the industry, providing quicker design turnaround times, and more scalable and cost-effective solutions. By providing increased design freedom, AM technology additionally enables engineers to solve problems that were previously prohibitively complex or expensive to approach.

L-PBF printing has established itself as one of the leading forms of additive manufacturing, owing to its metal printing ability and high dimensional accuracy when compared to alternative forms of AM techniques. However, the predictability of surface roughness and its relation to channel performance is one of the key elements holding back the reliable implementation of this technology for the manufacturing of liquid rocket engine combustion chamber nozzles.

The experimental analysis of surface roughness and fluid flow performance in small L-PBF printed channels presented in this thesis contributes to our comprehension of these phenomena, and through that enables a more reliable, scalable and ultimately efficient adoption of L-PBF for the manufacturing of liquid rocket engines. chapter 6 provides an overview of areas of improvement over the presented research, as well as suggested avenues for future research.

Chapter 6

Recommendations

The results and analysis presented in chapter 4 addressed three main areas of focus: the applicability of open contour channels as witness specimens for closed channels, the variation of surface roughness with channel build angle, and the relation of pressure drop to friction factor. While a good number of conclusions can be drawn from the presented work, it is important to identify what areas require further investigation, as well as what avenues of research are opened by the results of this study. This chapter provides a review of the main elements of the study that could benefit from an extended investigation, and may guide any future work performed on this topic.

Statistical relevance
As a result primarily of budgetary limitations, the number of measured surfaces was relatively limited, and of a single material. Print defects further caused a reduction of the sample size destined for flow testing, resulting in 6 out of 18 channels being used, with none of the 60° channels being measured. While the trends in the resulting data showed consistency with expected values and tendencies, a larger sample set would allow for a more statistically significant results analysis. Additionally, samples surface areas had to be reduced on lower build angle channels as a result of witness lines.

Roughness averaging
The analysis of surface roughness focused only on upskin and downskin surfaces, allowing channels to be split for microscope measuring in a single cut. That being said, correlating surface roughness metrics to flow test data requires the definition of some aggregate roughness value to be used for the channel. In this case, averaging was performed over the four walls. Since the vertical walls were not actually measured, the assumption was made that the non measured vertical walls would have an equal surface texture to the average of all 90° walls measured within the relevant batch. However, Sa measurements of the vertical channels have shown that orientation alone can have an influence on surface roughness. It is recommended that future studies measure all four walls in order to arrive at a better estimate of aggregate roughness values for channels. On very small channels where two perpendicular cuts might not be feasible, this may be achieved by dedicating some channels in a sample to up/downskin measurements, and others to sidewall roughness measurements.

Dimensional accuracy and hydraulic diameter
As discussed in subsection 4.2.8, the flow tested channels were found to have a significantly higher cross sectional area in comparison to their design. With the exception of one channel, all were approximately 25% higher than expected. The correction for this was done using microscopic scans to account for the true cross sectional area. Further corrections were made using constricted flow theory to account for a boundary layer with the height of the average surface deviation. The application of constricted flow theory shifted results towards lower equivalent sand grain roughnesses and lower friction factors as the effective area was reduced for the same pressure drops. It should be noted however that this could be considered as a double correction of of hydraulic diameter, and future work would benefit from a more detailed review of proper hydraulic diameter definition.

Witness specimen orientation
As discussed in section 4.2.4, the witness channels showed close correlation with their close contour equivalents in terms of surface roughness. That being said, all witness channels were printed in the exact same orientation as their counterparts, meaning the comparison does not suffer from any orientation-induced roughness effects. While this use of witness channels is easily applicable for straight channels, the same may not be true for all industrial applications. Beyond the removal of a need to destructively inspect printed parts, witness specimens should also provide a simple and straight forward way to determine roughness. With the increased geometrical complexity enabled by L-PBF printing, an increasing amount of designs feature curved, helical, or other complex shaped channels. It is recommended to investigate how well a single witness channel orientation maps to a closed channel that features a wide range of print orientations, and may be exposed to inert gas flow differently along its length.

Data filtering
Only primary parameters were investigated, with the goal of relating these to flow performance. If a more in depth analysis is performed on solely the surface roughness, contributions of both roughness and waviness should be analyzed separately in addition to the primary analysis.

Extended roughness parameter review
The surface roughness analysis was primarily aimed at investigating the effects of build angle on surface roughness, and how consistent the differences with open channels stay as the build angle changes. The large amount of available roughness parameters means only a sub-selection could be selected for analysis. Parameters such as developed surface area, that may be more relevant to studies that extend into the realm of heat transfer analysis, were not investigated. Future work that may expand the applicability of results to heat transfer analysis may benefit from looking at a more extensive sets of parameters.

Appendix A

Overview of Surface Roughness Metrics

Symbol	Type	Subtype	Description
Ra	Profile	Height	Arithmetic mean height deviation $R_a = \frac{1}{l_r} \int_0^{l_r} z(x)dx$
Rq	Profile	Height	RMS average height deviation $R_q = \sqrt{\frac{1}{l_r} \int_0^{l_w} z(x)^2 dx}$
Rv	Profile	Height	Maximum valley depth *Calculated from mean surface height to lowest point*
Rp	Profile	Height	Maximum peak height *Calculated from mean surface height to highest point*
Rt	Profile	Height	sampling peak-to-valley height *Maximum peak-to-valley height within one sampling length*
Rz	Profile	Height	Sampling peak-to-valley height *Maximum peak-to-valley height within one assessment length*
Rdq	Profile	Hybrid	RMS average of profile slope $R_{dq} = \sqrt{\frac{1}{l_r} \int_0^{l_r} (\theta(x) - \bar{\theta})^2 dx}$
Rsk	Profile	Hybrid	Profile skewness $R_{sk} = \frac{1}{R_q^3} \left(\frac{1}{l_r} \int_0^{l} {}_r z^3(x)dx \right)$
Rku	Profile	Hybrid	Profile Kurtosis $R_{ku} = \frac{1}{R_q^4} \left(\frac{1}{l_r} \int_0^{l} {}_r z^4(x)dx \right)$
Sa	Areal	Height	Areal arithmetic mean height $S_a = \frac{1}{A} \int \int_A z(x,y)dxdy$
Sq	Areal	Height	Areal RMS average height $S_q = \sqrt{\frac{1}{A} \int \int_A z(x,y)dxdy}$

Symbol	Type	Subtype	Description
Sp	Areal	Height	Areal max peak height *Calculated from mean surface height to highest surface peak*
Sv	Areal	Height	Areal max valley depth *Calculated from mean surface height to deepest surface valley*
Sz	Areal	Height	Areal max peak-to-valley height *Maximum peak-to-valley height within full sampling area*
Ssk	Areal	Hybrid	Areal skewness $S_{sk} = \frac{1}{S_q^3}\frac{1}{A}\int\int_A z^3(x,y)dxdy$
Sku	Areal	Hybrid	Areal kurtosis $S_{sk} = \frac{1}{S_q^4}\frac{1}{A}\int\int_A z^4(x,y)dxdy$
Sdq	Areal	Hybrid	Areal RMS average surface gradient $Sdq = \sqrt{\frac{1}{A}\int\int\left(\frac{\delta z^2}{\delta x} + \frac{\delta z^2}{\delta y}\right)dxdy}$
Sdr	Areal	Hybrid	Developed surface area *Excess of developed area above projected area*
Sxp	Areal	Functional	Peak extreme height $S_{xp} = S_{mc}(2.5\%) - S_{mc}(50\%)$
$Smr(p)$	Areal	Functional	Areal material ratio at cutting height c
$Smc(r)$	Areal	Functional	Inverse areal material ratio at material ratio p
Vm	Areal	Functional	Material volume $V_m(mr) = k\int_{0\%}^{mr}\left(S_{mc}(q) - S_{mc}(mr)\right)dq$
Vmc	Areal	Functional	Core material volume $V_{mc} = V_m(mr2) - V_m(mr1)$
Vv	Areal	Functional	Void volume $V_v(mr) = k\int_{mr}^{100\%}\left(S_{mc}(mr) - S_{mc}(q)\right)dq$
Vvc	Areal	Functional	Core void volume $V_{vc} = V_v(mr1) - V_v(mr2)$
Vmp	Areal	Functional	Peak material volume
Vvv	Areal	Functional	Dales void volume
Sal	Areal	Spatial	Autocorrelation length $Sal = \min\sqrt{tx^2 + ty^2}$

Symbol	Type	Subtype	Description
Str	Areal	Spatial	Texture aspect ratio $Str = \frac{r_{min}}{r_{max}}$
Std	Areal	Spatial	Texture direction *Indicates dominant texture direction*
$S10z$	Areal	Feature	Averaged significant heights parameter $Str = \frac{r_{min}}{r_{max}}$
$S5v$	Areal	Feature	Arithmetic mean of 5 most significant valleys
$S5z$	Areal	Feature	Arithmetic mean of 5 most significant peaks
Spd	Areal	Feature	Peak density *Density of determined number of peaks over full assessment area*
Sdc	Areal	Feature	Arithmetic mean peak curvature

Appendix B

Sample Design Drawings

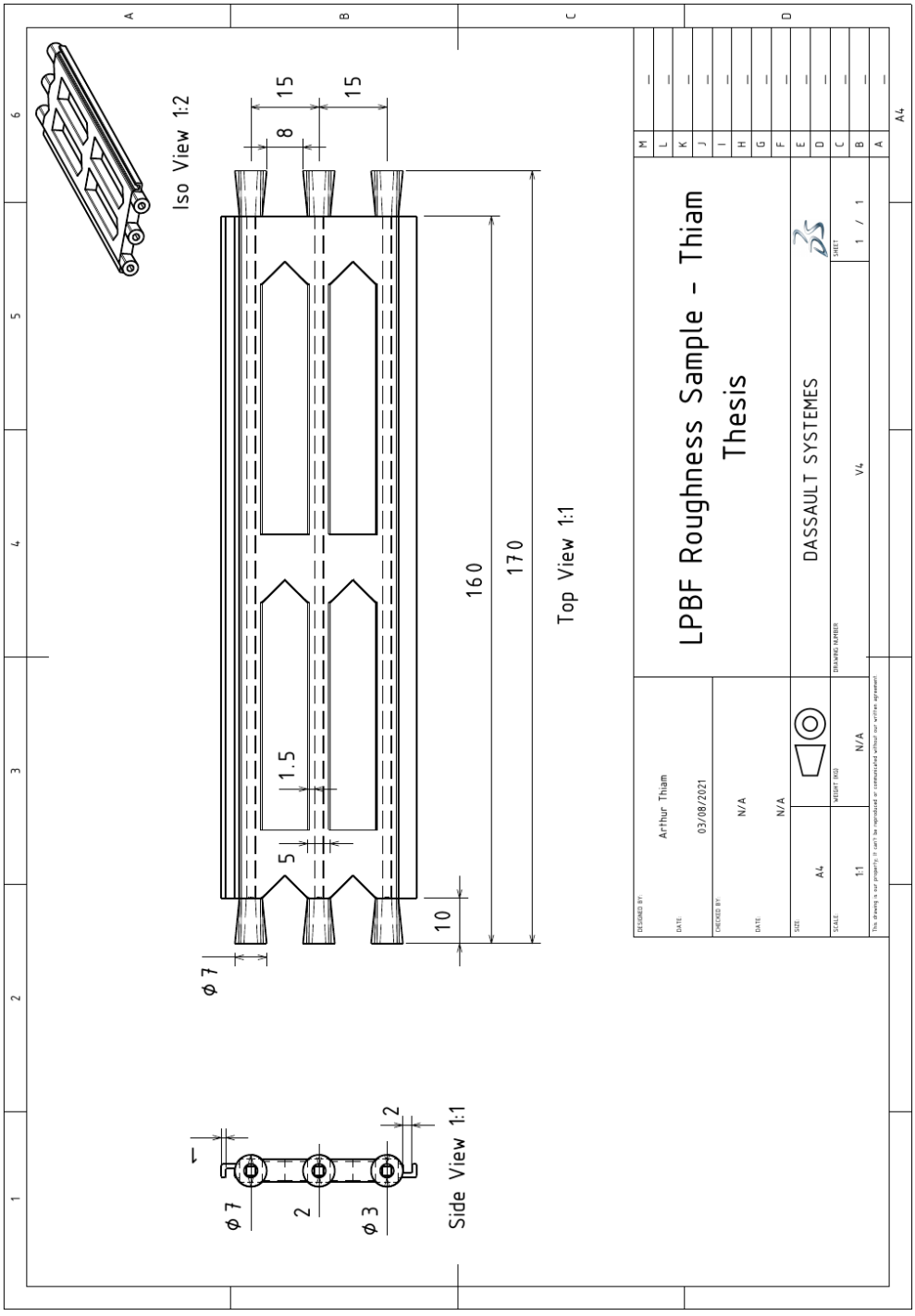

Figure B.1: Sample Technical Drawing

Appendix C

Welding Clamp Design Drawings

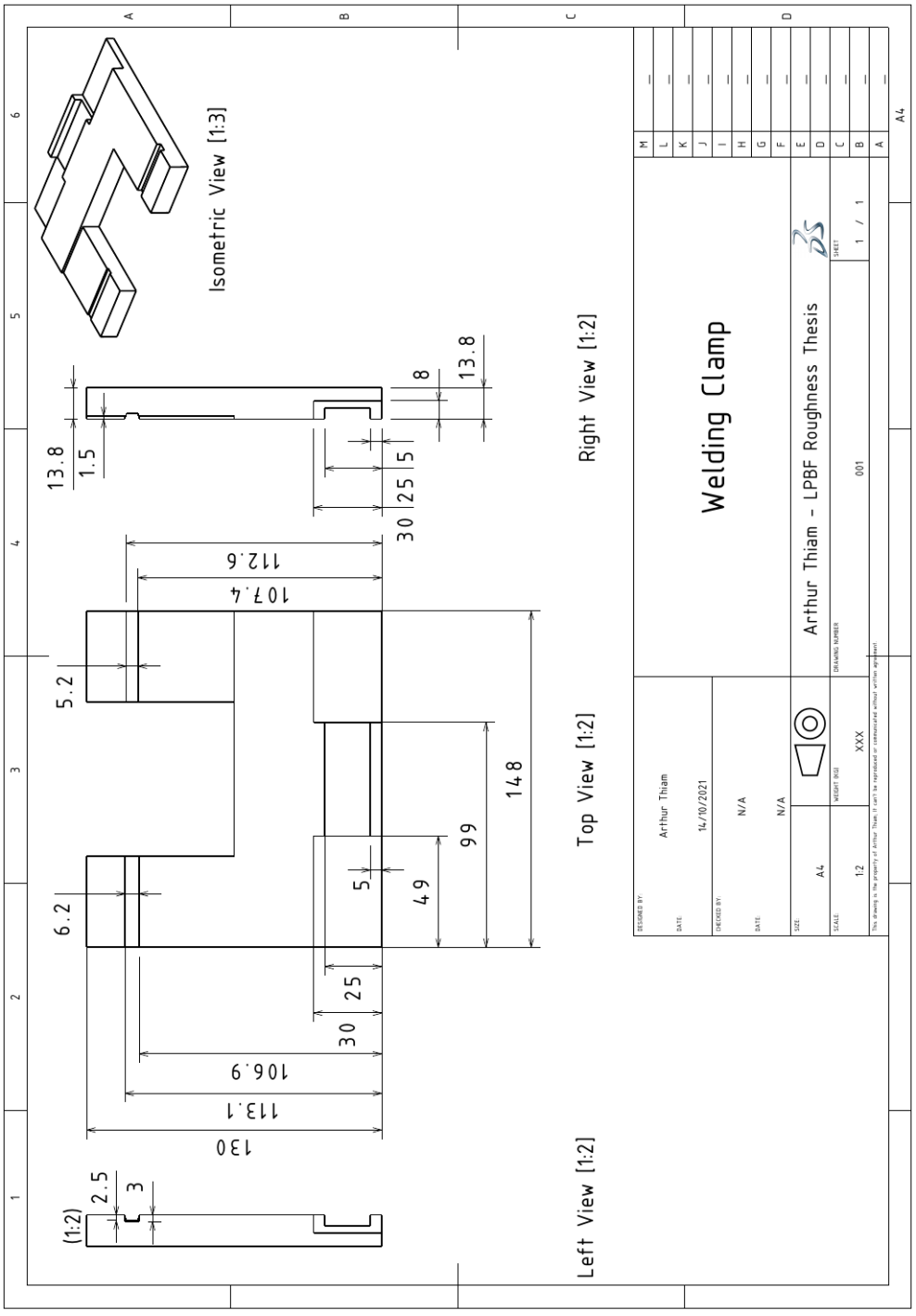

Figure C.1: Welding Clamp Technical Drawing

Appendix D

Sample Database

— Page Intentionally Blank —

D.1 Print Settings and Post Processing

Table D.1: Sample print and process settings

Sample	Machine	Recoater Blade	Heat treatment	Layer thickness	ED [J/mm3] (Up/Down)	Microshot peening
B1-45-A	DMP Flex 350	Carbon brush	1hr @ 980°C	30 μm	62/30	-
B1-45-B	DMP Flex 350	Carbon brush	1hr @ 980°C	30 μm	62/30	-
B1-45-C	DMP Flex 350	Carbon brush	1hr @ 980°C	30 μm	62/30	-
B1-60-A	DMP Flex 350	Carbon brush	1hr @ 980°C	30 μm	62/30	-
B1-60-B	DMP Flex 350	Carbon brush	1hr @ 980°C	30 μm	62/30	-
B1-60-C	DMP Flex 350	Carbon brush	1hr @ 980°C	30 μm	62/30	-
B1-90-A	DMP Flex 350	Carbon brush	1hr @ 980°C	30 μm	62/30	-
B1-90-B	DMP Flex 350	Carbon brush	1hr @ 980°C	30 μm	62/30	-
B1-90-C	DMP Flex 350	Carbon brush	1hr @ 980°C	30 μm	62/30	-
B2-45-A	DMP Flex 350	Soft blade	4hr @ 720°C	30 μm	62/30	x
B2-45-B	DMP Flex 350	Soft blade	4hr @ 720°C	30 μm	62/30	x
B2-45-C	DMP Flex 350	Soft blade	4hr @ 720°C	30 μm	62/30	x
B2-60-A	DMP Flex 350	Soft blade	4hr @ 720°C	30 μm	62/30	x
B2-60-B	DMP Flex 350	Soft blade	4hr @ 720°C	30 μm	62/30	x
B2-60-C	DMP Flex 350	Soft blade	4hr @ 720°C	30 μm	62/30	x
B2-90-A	DMP Flex 350	Soft blade	4hr @ 720°C	30 μm	62/30	x
B2-90-B	DMP Flex 350	Soft blade	4hr @ 720°C	30 μm	62/30	x
B2-90-C	DMP Flex 350	Soft blade	4hr @ 720°C	30 μm	62/30	x

D.2 Defects and Sample Purposing

Table D.2: Overview of sample print settings, defects, and testing

	Defects					Test purposing	
Sample	**Deformed entry***	**Kinked channel**	**Witness lines**	**Curved channel**	**Weld interference**	**Flow testing**	**Microscope testing**
B1-45-A	x	-	-	-	-	x	x
B1-45-B	x	-	-	-	-	x	x
B1-45-C	x	-	-	-	x	-	x
B1-60-A	x	x	-	-	-	-	x
B1-60-B	x	x	-	-	-	-	x
B1-60-C	x	x	-	-	-	-	x
B1-90-A	-	-	-	-	-	x	x
B1-90-B	-	-	-	-	-	x	x
B1-90-C	-	-	-	-	-	x	x
B2-45-A	-	-	x	x	-	-	x
B2-45-B	-	-	x	-	-	-	x
B2-45-C	-	-	x	x	-	-	x
B2-60-A	-	-	x	x	-	-	x
B2-60-B	-	-	x	-	-	-	x
B2-60-C	-	-	x	x	-	-	x
B2-90-A	-	-	-	x	-	-	x
B2-90-B	-	-	-	-	x	-	x
B2-90-C	-	-	-	x	-	-	x

*Deformed entries indicate small dimensional irregularities after base-plate removal. These are minor defects that were removed prior to the welding process to obtain a smooth transition from tube to channel.

Bibliography

[1] ISO 25178-2:2012(en), Geometrical product specifications (GPS) — Surface texture: Areal — Part 2: Terms, definitions and surface texture parameters.

[2] ISO 4287:1997(en), Geometrical Product Specifications (GPS) — Surface texture: Profile method — Terms, definitions and surface texture parameters.

[3] Making the unmakeable:How metal AM is bringing the aerospike rocket engine to life. *Metal AM*, Mar. 2022.

[4] ImageJ, June 2023.

[5] Laserform 316L(A) Datasheet, Oct. 2023.

[6] Laserform Ni718(A) Datasheet, Oct. 2023.

[7] Laserform Ti-gr23(A) Datasheet, Oct. 2023.

[8] Space Manufacturing Technology Report. Technical report, National Aeronautics and Space Administration, Dec. 2023.

[9] T. Adams, C. Grant, and H. Watson. A Simple Algorithm to Relate Measured Surface Roughness to Equivalent Sand-grain Roughness. *International Journal of Mechanical Engineering and Mechatronics*, 2012.

[10] U. Ali, H. Fayazfar, F. Ahmed, and E. Toyserkani. Internal surface roughness enhancement of parts made by laser powder-bed fusion additive manufacturing. *Vacuum*, 177:109314, July 2020.

[11] N. Andrew and R. Thomas. Advanced Manufacturing for Space Applications. Technical report, European Space Agency, July 2019. Reference: ESA-TECMS-TN-015895.

[12] L. C. Ardila. Effect of IN718 Recycled Powder Reuse on Properties of Parts Manufactured by Means of Selective Laser Melting. *Physics Procedia*, 2014.

[13] Y. Bai and Q. Bai. Hydraulics. In *Subsea Engineering Handbook*, pages 315–361. Elsevier, 2019.

[14] H. M. Beakawi Al-Hashemi and O. S. Baghabra Al-Amoudi. A review on the angle of repose of granular materials. *Powder Technology*, 330:397–417, May 2018.

[15] V. Bhavar, P. Kattire, V. Patil, S. Khot, K. Gujar, and R. Singh. A Review on Powder Bed Fusion Technology of Metal Additive Manufacturing. page 8.

[16] P. R. Bhave. ANALYSIS of FLOW in WATER. page 478.

[17] S. E. Brika, M. Letenneur, C. A. Dion, and V. Brailovski. Influence of particle morphology and size distribution on the powder flowability and laser powder bed fusion manufacturability of Ti-6Al-4V alloy. *Additive Manufacturing*, 31:100929, Jan. 2020.

[18] D. Buchbinder. High Power Selective Laser Melting (HP SLM) of Aluminum Parts. *Physics Procedia*, 2011.

[19] F. Calignano, L. Iuliano, M. Galati, P. Minetola, and G. Marchiandi. Accuracy of down-facing surfaces in complex internal channels produced by laser powder bed fusion (L-PBF). *Procedia CIRP*, 88:423–426, 2020.

[20] A. Charles, A. Elkaseer, L. Thijs, V. Hagenmeyer, and S. Scholz. Effect of Process Parameters on the Generated Surface Roughness of Down-Facing Surfaces in Selective Laser Melting. *Applied Sciences*, 9(6):1256, Mar. 2019.

[21] H. Chen and W. Yan. Spattering and denudation in laser powder bed fusion process: Multiphase flow modelling. *Acta Materialia*, 196:154–167, Sept. 2020.

[22] C. F. Colebrook. TURBULENT FLOW IN PIPES, WITH PARTICULAR REFERENCE TO THE TRANSITION REGION BETWEEN THE SMOOTH AND ROUGH PIPE LAWS. *Journal of the Institution of Civil Engineers*, 11(4):133–156, Feb. 1939.

[23] B. Dai, M. Li, and Y. Ma. Effect of surface roughness on liquid friction and transition characteristics in micro- and mini-channels. *Applied Thermal Engineering*, 67(1-2):283–293, June 2014.

[24] M. Daňa, I. Zetková, and P. Hanzl. The Influence of a Ceramic Recoater Blade on 3D Printing using Direct Metal Laser Sintering. *Manufacturing Technology*, 19(1):23–28, Feb. 2019.

[25] P. de Groot. Coherence Scanning Interferometry. In R. Leach, editor, *Optical Measurement of Surface Topography*, pages 187–208. Springer Berlin Heidelberg, Berlin, Heidelberg, 2011.

[26] C. English, S. Tewari, and D. Abbott. An Overview of Ni Base Additive Fabrication Technologies for Aerospace Applications. page 14.

[27] G. Favero, G. Berti, M. Bonesso, D. Morrone, S. Oriolo, P. Rebesan, R. Dima, P. Gregori, A. Pepato, A. Scanavini, and S. Mancin. Experimental and numerical analyses of fluid flow inside additively manufactured and smoothed cooling channels. *International Communications in Heat and Mass Transfer*, 135:106128, June 2022.

[28] L. A. Franco and A. Sinatora. 3D surface parameters (ISO 25178-2): Actual meaning of Spk and its relationship to Vmp. *Precision Engineering*, 40:106–111, Apr. 2015.

[29] B. Gao, H. Zhao, L. Peng, and Z. Sun. A Review of Research Progress in Selective LaserMelting (SLM). 2023.

[30] I. Gibson, D. W. Rosen, B. Stucker, and M. Khorasani. *Additive manufacturing technologies.* 2021. OCLC: 1225563364.

[31] P. Gradl, S. E. Greene, C. Protz, B. Bullard, J. Buzzell, C. Garcia, J. Wood, K. Cooper, J. Hulka, and R. Osborne. Additive Manufacturing of Liquid Rocket Engine Combustion Devices: A Summary of Process Developments and Hot-Fire Testing Results. 2018.

[32] P. R. Gradl, C. S. Protz, K. Cooper, D. Ellis, L. J. Evans, and C. Garcia. GRCop-42 Development and Hot-fire Testing Using Additive Manufacturing Powder Bed Fusion for Channel-cooled Combustion Chambers. In *AIAA Propulsion and Energy 2019 Forum*, Indianapolis, IN, Aug. 2019. American Institute of Aeronautics and Astronautics.

[33] P. R. Gradl and D. C. S. Protz. Channel Wall Nozzle Manufacturing Technology Advancements for Liquid Rocket Engines. *th International Astronautical Congress*, page 16.

[34] P. R. Gradl, D. C. S. Protz, D. D. L. Ellis, and S. E. Greene. Progress in Additively Manufactured Copper-Alloy GRCop-84, GRCop-42, and Bimetallic Combustion Chambers for Liquid Rocket Engines. *th International Astronautical Congress*, page 14.

[35] D. Gu and Y. Shen. Balling phenomena during direct laser sintering of multi-component Cu-based metal powder. *Journal of Alloys and Compounds*, 432(1-2):163–166, Apr. 2007.

[36] P. A. Hooper. Melt pool temperature and cooling rates in laser powder bed fusion. *Additive Manufacturing*, 22:548–559, Aug. 2018.

[37] K. Huang, J. Wan, C. Chen, Y. Li, D. Mao, and M. Zhang. Experimental investigation on friction factor in pipes with large roughness. *Experimental Thermal and Fluid Science*, 50:147–153, Oct. 2013.

[38] S. Kandlikar, D. Schmitt, and A. Carrano. Characterization of surface roughness effects on pressure drop in single-phase flow in minchannels.

[39] J. Kim, A. Wakai, and A. Moridi. Materials and manufacturing renaissance: Additive manufacturing of high-entropy alloys. 35(15), 2020.

[40] J. Kruth, L. Froyen, J. Van Vaerenbergh, P. Mercelis, M. Rombouts, and B. Lauwers. Selective laser melting of iron-based powder. *Journal of Materials Processing Technology*, 149(1-3):616–622, June 2004.

[41] J. Kruth, G. Levy, F. Klocke, and T. H. C. Childs. Consolidation phenomena in laser and powder-bed based layered manufacturing, Nov. 2007.

[42] J. Kruth, P. Mercelis, J. Van Vaerenbergh, L. Froyen, and M. Rombouts. Binding mechanisms in selective laser sintering and selective laser melting. *Rapid Prototyping Journal*, 11(1):26–36, Feb. 2005.

[43] U. P. Kumar, W. Haifeng, N. K. Mohan, and M. Kothiyal. White light interferometry for surface profiling with a colour CCD. *Optics and Lasers in Engineering*, 50(8):1084–1088, Aug. 2012.

[44] T.-P. Le, X. Wang, K. P. Davidson, J. E. Fronda, and M. Seita. Experimental analysis of powder layer quality as a function of feedstock and recoating strategies. *Additive Manufacturing*, 39:101890, Mar. 2021.

[45] R. Leach, editor. *Characterisation of Areal Surface Texture*. Springer Berlin Heidelberg, Berlin, Heidelberg, 2013.

[46] M. Leary. Powder bed fusion. In *Design for Additive Manufacturing*, pages 295–319. Elsevier, 2020.

[47] M. Lewis F. Friction Factors for Pipe Flow. pages 671–684, 1944.

[48] Y. Liu, Y. Yang, S. Mai, D. Wang, and C. Song. Investigation into spatter behavior during selective laser melting of AISI 316L stainless steel powder. *Materials & Design*, 87:797–806, Dec. 2015.

[49] M. J. Matthews, G. Guss, S. A. Khairallah, A. M. Rubenchik, P. J. Depond, and W. E. King. Denudation of metal powder layers in laser powder bed fusion processes. *Acta Materialia*, 114:33–42, Aug. 2016.

[50] A. Mostafaei, C. Zhao, Y. He, S. Reza Ghiaasiaan, B. Shi, S. Shao, N. Shamsaei, Z. Wu, N. Kouraytem, T. Sun, J. Pauza, J. V. Gordon, B. Webler, N. D. Parab, M. Asherloo, Q. Guo, L. Chen, and A. D. Rollett. Defects and anomalies in powder bed fusion metal additive manufacturing. *Current Opinion in Solid State and Materials Science*, 26(2):100974, Apr. 2022.

[51] L. Newton, N. Senin, E. Chatzivagiannis, B. Smith, and R. Leach. Feature-based characterisation of Ti6Al4V electron beam powder bed fusion surfaces fabricated at different surface orientations. *Additive Manufacturing*, 35:101273, Oct. 2020.

[52] L. Newton, N. Senin, C. Gomez, R. Danzl, F. Helmli, L. Blunt, and R. Leach. Areal topography measurement of metal additive surfaces using focus variation microscopy. *Additive Manufacturing*, 25:365–389, Jan. 2019.

[53] J. Nikuradse. *Laws of Flow in Rough Pipes*. National Advisory Committee For Aeronautics, 1933.

[54] E. O. Olakanmi. A review on selective laser sintering/melting (SLS/SLM) of aluminium alloy powders: Processing, microstructure, and properties. *Progress in Materials Science*, 2015.

[55] P. Oyar. Laser Sintering Technology and Balling Phenomenon. *Photomedicine and Laser Surgery*, 36(2):72–77, Feb. 2018.

[56] B. R. Munson, D. F. Young, T. H. Okiishi, and W. W. Huebsch. *Fundamentals of Fluid Mechanics, 6th Edition*. Don Fowley.

[57] D. B. Roidl, T. Fauner, and G. Additive. Continuous Improvement in Gas Flow Design. page 12.

[58] M. Sedlaček, B. Podgornik, and J. Vižintin. Correlation between standard roughness parameters skewness and kurtosis and tribological behaviour of contact surfaces. *Tribology International*, 48:102–112, Apr. 2012.

[59] I. Sideris and G.-C. Vosniakos. A simulation study of local powder bed gas shielding in Selective Laser Sintering/Melting machines, June 2020.

[60] Z. Snow, R. Martukanitz, and S. Joshi. On the development of powder spreadability metrics and feedstock requirements for powder bed fusion additive manufacturing. *Additive Manufacturing*, 28:78–86, Aug. 2019.

[61] J. C. Snyder and K. A. Thole. Understanding Laser Powder Bed Fusion Surface Roughness. *Journal of Manufacturing Science and Engineering*, 142(7):071003, July 2020.

[62] C. Stimpson. Roughness Effects on Flow and Heat Transfer for Additively Manufactured Channels. *Journal of Turbomachinery*, page 11, 2015.

[63] G. Strano, L. Hao, R. M. Everson, and K. E. Evans. Surface roughness analysis, modelling and prediction in selective laser melting. *Journal of Materials Processing Technology*, 213(4):589–597, Apr. 2013.

[64] G. Strano, L. Hao, R. M. Everson, and K. E. Evans. Surface roughness analysis, modelling and prediction in selective laser melting. *Journal of Materials Processing Technology*, 213(4):589–597, Apr. 2013.

[65] S. Sun, M. Brandt, and M. Easton. Powder bed fusion processes. In *Laser Additive Manufacturing*, pages 55–77. Elsevier, 2017.

[66] G. Takacs. A Review of Production Engineering Fundamentals. In *Sucker-Rod Pumping Handbook*, pages 13–56. Elsevier, 2015.

[67] W. Tato, L. Blunt, I. Llavori, A. Aginagalde, A. Townsend, and A. Zabala. Surface integrity of additive manufacturing parts: a comparison between optical topography measuring techniques. *Procedia CIRP*, 87:403–408, 2020.

[68] A. Thiam, A. Cervone, and P. Gradl. Surface Roughness of As-Built Laser-Powder Bed Fusion Parts. page 83.

[69] D. S. Thomas and S. W. Gilbert. Costs and Cost Effectiveness of Additive Manufacturing. Technical Report NIST SP 1176, National Institute of Standards and Technology, Dec. 2014.

[70] Y. Tian, D. Tomus, P. Rometsch, and X. Wu. Influences of processing parameters on surface roughness of Hastelloy X produced by selective laser melting. *Additive Manufacturing*, 13:103–112, Jan. 2017.

[71] L. Todhunter, R. Leach, S. Lawes, and F. Blateyron. Industrial survey of ISO surface texture parameters. *CIRP Journal of Manufacturing Science and Technology*, 19:84–92, Nov. 2017.

[72] A. Townsend, N. Senin, L. Blunt, R. Leach, and J. Taylor. Surface texture metrology for metal additive manufacturing: a review. *Precision Engineering*, 46:34–47, Oct. 2016.

[73] A. Tsigarida. On the use of confocal microscopy for calculating the surface microroughness and the respective hydrophobic properties of marble specimens. *Journal of Building Engineering*, page 9, 2021.

[74] B. Vayre, F. Vignat, and F. Villeneuve. Metallic additive manufacturing: state-of-the-art review and prospects. *Mechanics & Industry*, 13(2):89–96, 2012.

[75] D. Whitehouse. Identification and separation of surface features. In *Surfaces and Their Measurement*, pages 16–47. Elsevier, 2002.

[76] D. Whitehouse. Profile and areal (3D) parameter characterization. In *Surfaces and Their Measurement*, pages 48–95. Elsevier, 2002.

[77] E. Xometry. Selecting right surface roughness for CNC machining.

[78] I. Yadroitsev and I. Smurov. Surface Morphology in Selective Laser Melting of Metal Powders. *Physics Procedia*, 12:264–270, 2011.

[79] L. Yasmina and L. Rachid. Evaluation of Energy Losses in Pipes. *American Journal of Mechanical Engineering*, page 6.

[80] Y. Zhou and F. Ning. Build Orientation Effect on Geometric Performance of Curved-Surface 316L Stainless Steel Parts Fabricated by Selective Laser Melting. *Journal of Manufacturing Science and Engineering*, 142(12):121002, Dec. 2020.

[81] C. [U+FFFD] Çalışkan, G. Özer, M. Coşkun, and E. Koç. Investigation of direct metal laser sintering downskin parameters' sagging effect on microchannels. *The International Journal of Advanced Manufacturing Technology*, Apr. 2021.